

POLITECNICO DI TORINO
Scuola di Dottorato

Dottorato in Meccanica – XXIV ciclo

TESI DI DOTTORATO

**Investigation of under-platform damper
kinematics and dynamics**



Liu Tong

Tutore :
Prof. Muzio M. Gola

Coordinatore del corso di dottorato :
Prof. Luigi Garibaldi

Febbraio, 2013

Introduction

Under-platform damper is a device used in turbo engines to attenuate forced vibration amplitude and prevent high cycle fatigue of turbine blades, which are caused by hot gas flow and the vibration of engine rotor.

The device itself is a piece of metal and during service it is loaded by centrifugal force against the platform underside of two adjacent blades. The relative movement of the blade platforms produces possible slip on the damper surfaces that dissipates the vibration energy through heat induced by friction.

Although the damper is a simple device, it is difficult to predict and optimize its performance in the blades system by combining blade FE model, contact model and kinematic model due to marked nonlinearity of friction force, geometry coupling of two contact surfaces and uncertainties of contact surface conditions. As concluding from literature, the important parameters controlling damper effectiveness include damper mass, friction coefficient, contact stiffness and damper geometry.

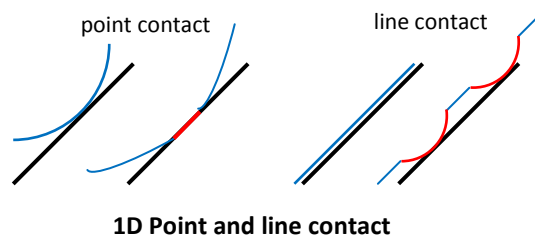
All numerical models require knowledge or information of contact and friction parameters, which are established either through direct single interface frictional measurements, done with the help of correct test arrangements or by fine tuning the parameters in numerical model and comparing the calculated response against the experimental response of damped blade(dummy or real) in vibration. What happen in detail on the damper kinematics and contact forces on the interface are not experimentally observed.

In this thesis, an alternative experimental way of investigating and evaluating under-platform damper behavior is proposed. By measuring relative movement between two simulated platforms, the movement of damper and forces transmitted through the damper, a record of the contact events(stick, slip, separation) which take place during the cycle is expected to provide information of friction coefficient, contact stiffness to better understand the damper behavior. It is paid attention to guarantee that the response determined by damper itself and contact interfaces should not be disturbed by test rig structure. The test rig is a trial to experimentally observe the damper kinematics and contact details , and furthermore reduce the ambiguity and complexity in optimizing damper geometry and performance .

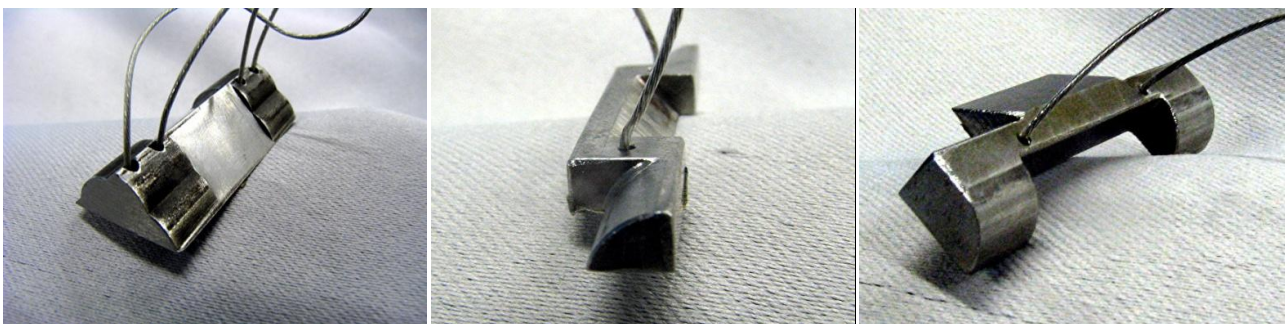
Two important motion types of under-platform damper are in phase (IP) and out of phase (OOP) motion. IP and OOP motion arise from the bending mode shapes of two adjacent vibrating blade with the same phase or opposite phase and normally their amplitude dominate among all the mode shapes. Equivalently during IP vibration one blade platform moves axially relative to the other platform and during OOP vibration one blade platform moves circumferentially relative to the other platform. In the experiments, relative motion along two perpendicular directions are

performed to simulate IP and OOP condition. In this thesis only 2D in plane motion of the damper is considered, translation and rotation in the other DOFs are not taken into account.

Damper geometry is a difficult factor for investigation. From experimental point of view, the traditional way of measuring response from the main structure damped by the under-platform damper is not convenient to change platform shapes and respective dampers once the structure is manufactured. From modeling point of view, the geometry influences both contact condition and interface coupling through the damper dynamics. According to current contact models, the contact interfaces can be simplified as a point or a line with discretized points.



In this thesis, three types of laboratory damper are used to reduce the uncertainty of this dual-interface friction test. One is so called three-point damper, which is based on a wedge-shaped damper but has one curved surface on one contact interface and two curved surfaces on the other contact interface. The advantage of three-point damper is that the contact region on its surfaces are determined, or more rigorously, determined in a macro way. The so called crossed curve-flat has two crossed surfaces, one of which is curved and the other is flat. The intersection point of curved line and straight line is intended to locate in the line where centrifugal force passes. The non-crossed curve-flat damper has surfaces like the crossed curve-flat damper but not crossed. The separation distance is intended to be made large to check the rotation effect.



A numerical simulation of the test is necessary for understanding the experimental results better and explore new geometries previous to new tests. On the other hand, the experimental results can be a validation tool of damper modeling once the results are reliable. In the simulation of this thesis, only macro contact model is implemented to compare the general response features of the damper from the tests when micro contact phenomenon is not significant. The stiffness of the damper itself is not considered, which means the damper is considered as a rigid body.

The thesis is divided into 5 chapters.

The first chapter is 'State of the Art' for friction damping mechanism and under-platform damper development. Historical and current contact model, kinematic model and simulation methods are referred to and commented.

The second chapter describes test rig set up and calibration procedures. The test rig is designed in a way conducting good performance, but material and structural limitations cannot be avoided completely. Calibration results give information on the stiffness distribution in the test rig and limitations of working range.

The third chapter analyzes kinematics measurement error and deduces the motion reconstruction of the damper from measured quantities. Force measurement error due to the structural indeterminacy is also presented and corrected.

The fourth chapter is contributed to demonstrating the experimental results for the mentioned two types of damper. At the beginning an analysis is made to link the contact stiffness parameter used in the contact model with the experimental hysteresis. Hysteresis, force distribution and motion features are described. Even if the test results have marked variability, the basic features of certain motion type is observed by linking the kinematics and damper equilibrium. Limitations of the test rig and corresponding results are outlined. Further improvements to the test rig are suggested.

The fifth chapter studies a numerical procedure to simulate the system response. Before applying the model and numerical solution to the test rig system, the numerical result is compared with an analytical solution for 1DOF system. The case when more than one stop happens during half a cycle is also obtained from the numerical calculation. Formulations are established taking the three-point damper as example, but relevant extensions can be done without much difficulty to other types of under-platform damper. Numerical solutions are compared with the experimental results, good consistency is obtained. Further investigations with the aid of the numerical tool are performed to check the characteristics of damper response.

Each chapter contains its conclusions.

Index

Chapter 1 State of the art	7
1.1 Dynamics with friction.....	7
1.2 Under-platform damper application	8
1.3 Contact mechanics with friction and hysteresis measurement	12
Chapter 2 Test rig set up and calibration	14
2.1 Components and function of the test rig	14
2.2 Introduction of piezoelectric actuator and piezomechanics.....	15
2.2.1 Necessity of preload structure for the actuator.....	15
2.2.2 Influence of preload structure to the displacement conducted by piezo actuator	15
2.3 Set up of piezoelectric actuators.....	16
2.4 Set up of the parallel mechanism.....	20
2.5 Set up of the force measurement structure.....	25
2.6 Test rig calibrations	28
2.6.1 Piezoelectric actuator and force sensor operation range	28
2.6.2 Stiffness distribution in the test rig	31
2.7 Check of the synchronicity of measured signals	35
2.8 Conclusions.....	36
Chapter 3 Measurement error analysis	37
3.1 Measurement of relative movement between the two platforms.....	37
3.2 Measurement of damper kinematics	38
3.2.1 Parallax error	38
3.2.2 Reconstruction of damper motion and error factors.....	40
3.3 Force measurement error from static indeterminacy.....	42
3.4 Conclusions.....	46
Chapter 4 Experimental results	48
4.1 Stiffness from measured hysteresis	48
4.2 Out-of-phase results of three-point damper.....	51
4.2.1 Hysteresis characteristics	51
4.2.2 Influence of excitation frequency.....	55
4.2.3 Contact force distribution	57
4.2.4 Rotation features	60
4.3 In-phase results of three-point damper	63
4.3.1 Hysteresis characteristics	63

4.3.2 Damper motion reconstruction.....	64
4.3.3 Contact force distribution	69
4.4 In-phase results of crossed curve-flat damper	70
4.4.1 Typical hysteresis.....	71
4.4.2 Contact force distribution	73
4.5 Out-of-phase results of crossed curve-flat damper	74
4.6 In-phase results of non-crossed curve-flat damper	75
4.7 Conclusions.....	76
Chapter 5 Numerical simulation of damper motion with direct time integration.....	77
5.1 Overview of Den Hartog's solution	77
5.2 Direct time integration for motion equations with dry friction	79
5.3 Contact model description	83
5.4 Formulation of damper motion in the test rig	86
5.5 Simulation results of out-of-phase motion for three-point damper.....	91
5.5.1 Steady state response and comparison with experimental results	91
5.5.2 Solution from different initial conditions	94
5.5.3 Influence of excitation frequency and test rig stiffness	95
5.5.4 Response sensitivity to friction coefficient	96
5.6 Simulation results of in-phase motion for three-point damper.....	97
5.6.1 Steady state response and comparison with experimental results	97
5.6.2 Influence of damper angle.....	99
5.7 Exception case of unique steady state solution	100
5.8 Conclusions.....	101
Closure.....	103
Cited literature	105

Chapter 1 State of the art

1.1 Dynamics with friction

The problems in structural dynamics with friction became tractable since the 30s of last century. After good approximated results were obtained, in 1931 one of the first important exact solution was given by J.P. Den Hartog when studying a single degree of freedom (SDOF) system damped by Coulomb friction or mixture of Coulomb and viscous damping [1]. He showed both theoretically and experimentally that, depending on system parameters, the mass may continuously move or it may come to a stop during parts of each cycle. Levitan [2] studied the forced oscillations of a mass-spring-damper system in which the support rather than the mass is excited. He used a Fourier series approximation for the Coulomb friction force that acts between the mass and the support. Hundal obtained closed-form analytical expressions for a single DOF system with the Coulomb friction force acting between the mass and the ground. His work was limited to a maximum of two stops per cycle [3]. Pratt and Williams [4] analyzed the relative motion of two masses with Coulomb friction contact. They used a combined analytical-numerical approach to obtain the response of the system for arbitrary values of the friction force, excitation frequency and natural frequency of the bodies. They showed that under certain conditions multiple lock-ups per cycle are possible and that for frequency ratios (excitation frequency versus natural frequency) below 0.5 no continuous sliding motion is possible. Their results were limited to two blocks with the same mass and spring stiffness and support motion of the same amplitude and frequency.

The complexity of friction damping is not only from the difficulty getting an analytical solution for even simple systems, but also is related to sensitivity to system parameters and initial conditions. Dariusz Grech et al. [5] analyze a mechanical system in two-dimensional relative motion with friction. Although the system is simple, the peculiar interplay between two kinetic friction forces and gravity leads to the wide range of admissible solutions exceeding most intuitive expectations. When Wernitz and Hoffmann [6] process irregular friction brake vibration data, the recurrence analysis indicates that irregular vibration states of friction brakes are strongly dominated by intermittency phenomena. Phase space reconstruction suggests that this intermittency is dominated by low-dimensional irregular deterministic dynamics rather than by high-dimensional stochastic processes. Duffor and Woodhouse [7] study the linear stability of systems which contain

a sliding frictional contact at a single point. A condition for instability is found, in terms of the transfer functions of the two systems at the point of contact. This condition is explored for generic systems, to establish the circumstances under which instabilities might be expected. A major conclusion is that if the coefficient of friction is assumed to be constant, then at least one mode of one or other of the contacting systems must have a displacement at the contact with a particular pattern of signs. If such a mode exists then instability is possible, depending on the value of the coefficient of friction and on the frequencies and mode shapes of the other modes of the system.

Apart from studying the dynamics with friction itself, people also paid attention to the damping effect of friction. Beards and Williams [8] analyzed the damping due to rotational slip in structural joints. They studied a two DOF system and concluded, analytically and experimentally that, as the friction force increases the response amplitude goes through a minimum. Beards and Woowat [9] carried out an experimental study of a steel frame where the joint clamping forces could be varied. They found that an optimum clamping force exists that minimizes the frame response. More recently, in his review of friction-induced vibration Ibrahim [10] compares the energy dissipated by friction to the energy dissipated by a viscous damper. the energy dissipated through friction is analyzed for a type of friction dampers used to reduce squeal noise from railway wheels. I.López et al. analytically study one degree-of-freedom system, giving existence and stability of the steady state solution and then the energy dissipated per cycle is determined as a function of the system parameters [11]. In this way the influence of the mass, natural frequency and internal damping of the friction damper on the energy dissipation is established. It is shown that increasing the mass and reducing the natural frequency and internal damping of the friction damper maximizes the dissipated energy.

1.2 Under-platform damper application

The under-platform damper was used in the turbo machinery since the 70's of last century and in the beginning investigations of this kind of damper is limited to practice and simple models. One of the most important characteristic of the blade damper design aims to search for the best value of mass that produces the optimal normal load when the turbine is rotating.

During the 80's J.H. Griffin [12] and C.H. Menq et al. study the blade-to-ground damper(Fig.1.1). If the normal load is small with respect to the exciting force, the FRF of the blade tends to the linear free response, i.e. without damper. If the load is large with respect to the excitation force the structure stiffens because the blade-to-ground damper sticks introducing the damper stiffness in the dynamics of the blade. In this case its response results in a linear FRF with resonance frequencies shifted toward greater values. With the introduction of a new stiffness the structure changes its response, changing its modal deflections. The damper stiffness together with the normal load are the two variables of their initial studies. The mass of the damper is considered negligible. The response of a single DOF is studied through modal analysis. The proposed solution is an approximation of the equilibrium equation by interpolating linear results of the linear free

and stick response. By iterative procedure the resonance amplitude that verifies the nonlinear equilibrium equation for a given combination of excitation force and normal preload is calculated. Varying the normal load (and keeping the damper stiffness constant) the resonance response is minimum for a particular value of normal preload and excitation force. The minimum modal response corresponds to an average between the linear free mode and the linear stuck mode. The iterative procedure reveals the corresponding optimal displacement of the response (the minimum resonance amplitude with varying normal load) is twice the value of the displacement at which slip is initiated. In this case the contact is half in slip condition and half in stick condition within one oscillation. Experimental test varying the normal load for the two types of damper verifies the numerical solution. Some differences are detected when the structure reaches the stuck condition. This happens for high normal load. Here the numerical amplitudes result higher. The difference is explained with the not properly correct hypothesis of negligible mass of the damper and the presence of micro-slip is the most important cause of this difference. In 1984 the influence of static and dynamic friction coefficient is investigated through analytical and time integration method [13]. The static friction coefficient tends to maintain the contact in stick condition.

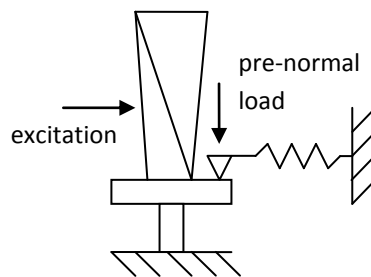


Fig.1.1 Demonstration of blade to ground damper

The introduction of the Harmonic Balance Method (HBM) was an important step in the analytical study of the nonlinear structure dynamics with friction. The HBM approximation proves to be a useful tool able to interact with complex structure modeled with FEM. The contact model can be integrated with HBM to predict the structure response. Normally the predicted response matches well with the time domain calculation except when some higher order mode shapes of the structure are excited [14].

When the normal load is large with respect to the excitation force, micro-slip effect may occur, where parts of the contact area slip while others stick. The model of a traditional Coulomb hysteresis loop (immediate state transition for one contact pair as a whole) does not reproduce nonlinear micro-slip influence on the dynamic response. In 1997 Sanlyturk et al. represented micro-slip hysteresis cycle by analytical formulation gradual transition from stick to slip through exponential curve [15].

Discretized approach has been adopted to reproduce micro-slip effect since the model proposed by Iwan in 1967 [16, 17, 18]. The discretized contact models are based on Coulomb friction theory. a set of parallel element, each one with its elastic contact and its coefficient. Fig.1.2 shows the configuration of this kind of model.

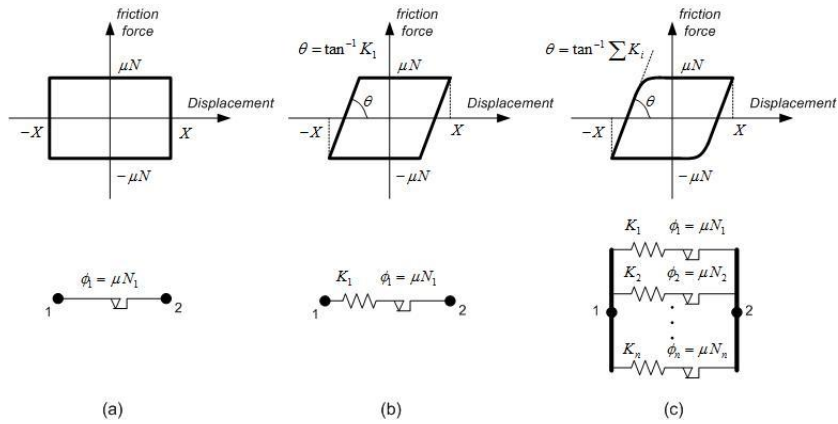


Fig.1.2 1D macro contact element and element arrays simulating micro contact

When strain hardening is taken into consideration, the model in Fig.1.2.c can be modified to the form in Fig.1.3.

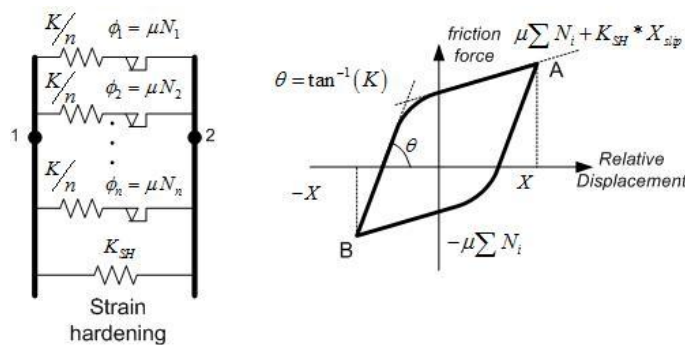


Fig.1.3 Modified 1D micro contact model with strain hardening

In 1986 Meng et al. introduced a different continuous micro-slip model, where a continuous area is loaded by a uniform pressure [19] and later used by Csaba [20]. This model can be referred as to the Bar-model. The contact body is represented by a rod having longitudinal elastic properties (Young modulus E , cross section A). The rod constraint is represented by the contact surface. When a tangential force is applied at one end of the Bar element, the distribution of shear at the contact interface produces slip in the point where the force is applied because it overpasses the local pressure multiplied for the friction coefficient. The disadvantage of Bar model is that there is no direct coupling between the geometry of most actual dampers and the relevant parameters of Bar model.

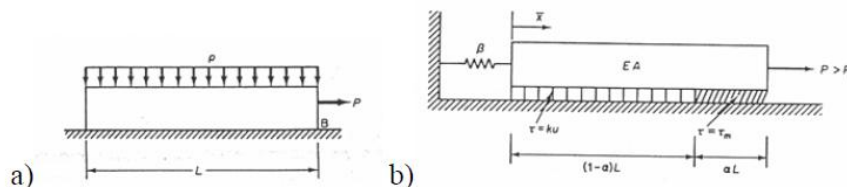


Fig.1.3 1D Bar model (from [19])

In 1997 and 1998 Yang et al. introduced a new variable for a 1D tangential displacement contact model: a variable normal load through the presence of a normal contact stiffness [21, 22]. This is a

great improvement to the contact model since it introduces more physical information represented by the real contact surfaces(possible lift-off and stick state disappearance when tangential relative motion reverses). The variable normal load was introduced also in the 2D contact model [23].

In 1998, Yang and Menq introduce the problem of blade damping for the wedge shaped under-platform damper [24, 25]. In this method, on each contact interface the contact is represented by a point contact. The damper inertia and stiffness of itself is neglected. The kinematics for wedge shaped damper is important by coupling the two contact interfaces. Transition criteria for the coupled contact interfaces are given according to a Coulomb contact model with tangential stiffness also considering the variable normal load even if without normal contact stiffness. The kinematic and contact model are shown in Fig.1.4. Maps are diagrammed to show how the inclinations of the wedge damper sides influence the amount of stick-slip state for the two sides of the damper. These are two important articles about under-platform damper which start more comprehensive investigations on the damper behavior.

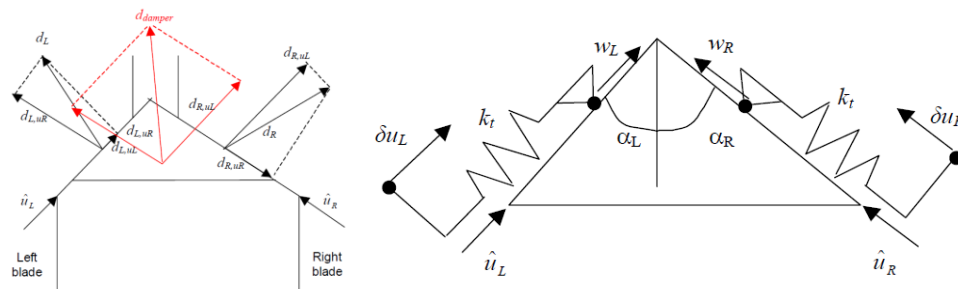


Fig.1.4 Kinematic and contact model used in [24,25]

Damper geometry influences not only the contact condition but also the coupling of interfaces. Except for triangle wedge damper, damper with curved contact surfaces are studied like cylindrical dampers [26] or with two rounded contact surfaces with a different position of the center [27], unsymmetrical dampers [28], and dampers with parabolic surfaces [29].

In [30], the authors provide a modeling which makes use of experimentally measured contact characteristics(hysteresis loops) for description of the basic contact behavior of given material combination with respective surface finish. It is shown that the commonly used under-platform dampers are prone to rolling motion(from experiment), an effect which reduces the damping in certain modes of vibration usually described as the lower nodal diameter bladed-disk modes, which is also proposed by [24]. The analysis methodology is based on a combination of the harmonic balance method and a structural modification approach, which is also described in [14].

Models in [28] include the damper inertia and consider a rotational contribution to the damper kinematics leading to a possible lift off from the blade platforms, which is currently the most complicated damper model. [31] explains the experiment data scattering of blade response damped by the damper as a consequence of the non-uniqueness of the static normal preloads. In [32], the author measures the kinematics of two types of under-platform dampers(wedge and cylindrical) in the test of traditional damper-blade test rig. The strong influence of the rotation of

the under-platform damper on the dynamic response is analyzed in particular for the in-phase vibration of two dummy blades.

1.3 Contact mechanics with friction and hysteresis measurement

Although in the work of this thesis no continuous contact mechanics theory is applied to investigate the damper behavior, the frictional contact problem is an important field in contact mechanics, which provides physical meaning of discrete contact modeling parameters and guides the new methodology to be applied in dynamic problems with friction.

In 1938 Cattaneo and then 1949 Mindlin published their seminal works on the effect of forces tangential to the interface of elastic bodies in contact and these studies take slip into account. They extended Hertz theory for normally loaded elastic spheres by adding an increasing tangential loading to these spheres and considering slip exclusively at their contact interface [33]. The concept of tangential stiffness and uniform friction coefficient is proposed. Fig.1.5 is the demonstration of this problem. Although Cattaneo and Mindlin's concept has some assumptions made for simplification, it has been widely used. [34] points out that the contact area diameter d_0 , resulting from the normal load P , may change considerably when a tangential loading Q is added, which is ignored in Cattaneo and Mindlin's model. The phenomenon of increasing contact area during tangential loading was first observed experimentally in 1950 by McFarlane and Tabor and independently by Parker and Hatch.

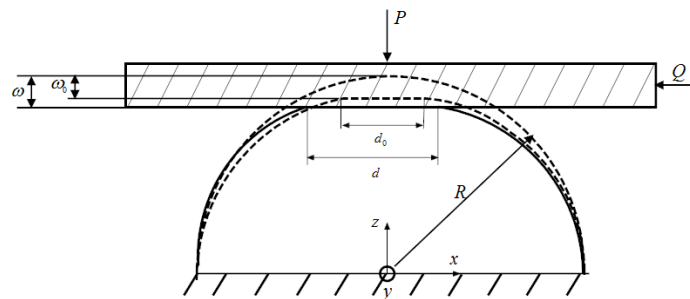


Fig.1.5 Spherical contact under combined normal and tangential loading

Apart from the detailed simplification, Cattaneo and Mindlin's theory has been widely used in normal condition and scale and partly verified by the experiments carefully designed for contact measurement.

Efforts to measure contact hysteresis date back to 1952, Mindlin et al. [35] measured the hysteresis loops for lenses with convex surfaces. The annular shape of the observed surface wear showed agreement with the theories, however the hysteresis loops measured does not agree well with theory when displacement amplitude is small. Johnson [36] measured static and dynamic hysteresis loops for hard steel spheres in contact with hard steel rollers. The slopes of the hysteresis cycles which represents the tangential stiffness showed good agreement with the theory. Goodman and Brown [37] measured hysteresis loops and energy dissipated at the contacts

of a sphere oscillating between two parallel flat plates. For a cyclic tangential force that produced only micro-slip, their experimental results agreed well with the theory.

One of the difficulties in measuring contact parameters relates to the disturbance of the test rig structure. The authors in [38] developed an experiment to measure structural response on a turbine vane segment. They obtained contact stiffness and dissipated energy by measuring hysteresis loops. A test rig which provides hysteresis measurement is described in [39] and the test gives data for contact behavior of under-platform damper by using real damper and same material for the other block to be rubbed on. [40] presents a new test rig design to measure tangential contact hysteresis during micro-slip, in which potential measurement errors are estimated and corrected if possible.

1.4 Time integration scheme

It is not easy or even intractable to get analytical solution of a dynamical system with friction. For large structures with friction damping, the combination of modal reduction and HBM provides an effective tool to predict the main structure's response. But when investigating the damper kinematics and dynamics itself, the simplification of HBM is not appropriate due to the nonlinearity of this unconstrained body. The test rig discussed in this thesis is designed to investigate the damper kinematics and dynamics not disturbed by the test structure, but in practice this is not achieved. In the range where outer dynamics can be neglected, the simulation of damper behavior adopts a time integration method.

The numerical procedure adopted in this thesis is based on Newmark- β method which has the advantage of second order accuracy. Lu et al. employ a state-space formulation and a linear integration scheme to get the discrete-time solution of dynamic response of a structure system equipped with multiple friction devices, which can be in either a stick or slip state[41]. In [42] the authors present a new dissipative and contact-stabilized time discretization scheme for dynamic frictional contact problem. Their approach allows an implicit treatment of the contact forces in the framework of the Newmark scheme. This may be helpful to find improvements to the direct integration used in this thesis.

Chapter 2 Test rig set up and calibration

2.1 Components and function of the test rig

The test rig is designed aiming at:

- measuring the forces transferred between the two simulated platforms of neighbouring blades through the under-platform damper.
- measuring left platform movement and damper movement relative to the right platform to simulate In-phase and Out-of-phase motion.

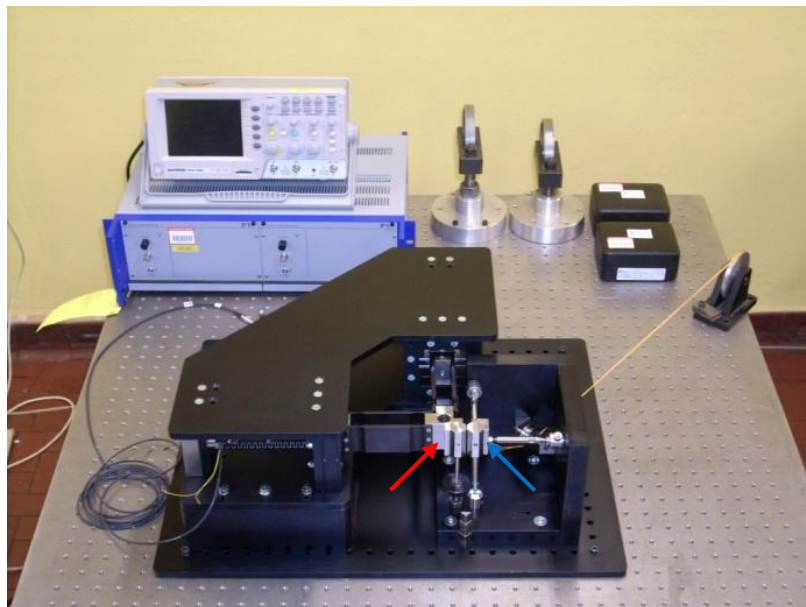


Fig.2.1 General view of the test rig

The test rig is composed by two main parts. One part comprising from two perpendicular piezoelectric actuators with auxiliary preloading and guiding structures produces any planar displacement to the left platform (shown as the red arrows in Fig.2.1). The other part contains two

perpendicularly located piezoelectric force sensors and measures the transferred force passing through the right platform (shown as the blue arrows in Fig.2.1) and guiding rod.

2.2 Introduction of piezoelectric actuator and piezomechanics

2.2.1 Necessity of preload structure for the actuator

Piezoelectric ceramics is a kind of material that can produce deformation according to applied charge or produce charge according to applied deformation. The current mostly used and reliable piezoelectric ceramics material is called PZT.

A piezoelectric stack is composed by a series of thin layers of piezoelectric ceramics in order to achieve large displacements by means of a summation of small displacement from each layer. Generally, a typical stack contains several thin layers of 0.2 up to 1 mm thick of piezoelectric ceramic glued together with alternate electrical poling directions.

PZT ceramic material can withstand pressures up to 250 MPa without breaking. This value must never be approached in practical applications, however, because depolarization occurs at pressures on the order of 20 % to 30 % of the mechanical limit. The PZT ceramic is especially sensitive to shear forces, which must be intercepted by external mechanisms.

For stacked actuator (which is a combination of several materials), additional compression limitations apply. Parameters such as aspect ratio, buckling, interaction at the interfaces, etc. must be considered.

Furthermore, the constructive configuration of piezoelectric stack makes it very sensible to pulling forces that can detach the layers. Therefore, ordinary piezoelectric stacks should work with an initial preload capable to avoid pulling forces. Torsion and bending moment should also be avoided due to the weakness of the glue [45].

2.2.2 Influence of preload structure to the displacement conducted by piezo actuator

Actuator stiffness is an important parameter for calculating force generation, resonant frequency, full-system behavior, etc. As in normal cases, the stiffness of a piezo actuator is expressed in terms of a spring constant k_s . If the external force on the actuator is constant, no displacement reduction happens and only the origin of displacement is shifted. But if the external force is variable during the operation, which happens when the preload spring is applied, the displacement conducted by the piezo actuator is reduced as shown in Fig 1.2. In the figure, L_0 is the initial length of the stack, ΔL_0 is the nominal displacement produced by the stack without external force, ΔL is the real displacement produced by the stack coupled with the preload spring with stiffness k_m , ΔL_R is the respective displacement loss.

From the equilibrium equation $k_s \Delta L = k_m (\Delta L_0 - \Delta L)$, we have:

$$\Delta L = \Delta L_0 \left(\frac{k_m + k_S}{k_S} \right), \Delta L_R = \Delta L_0 \left(\frac{k_m}{k_S} \right) \quad (1)$$

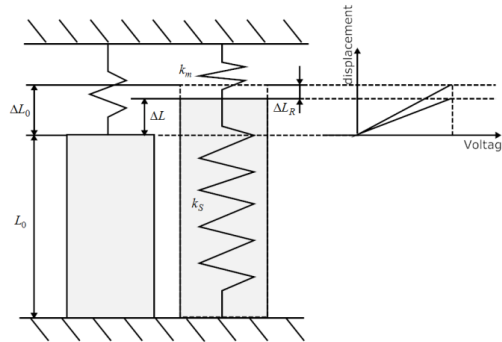


Fig2.2 Piezoelectric actuator displacement reduction due to preload spring

The result shows that the real displacement produced by the piezo actuator will be reduced with the proportion between preload stiffness and actuator stiffness, which means the preload stiffness cannot be too stiff.

The piezoelectric stack used in this test rig is PICA™-Power Actuator Model P-010.80. This model of actuator has the technical specifications as following:

Table 2.1 Piezoelectric stack parameters

MODEL	Displacement [μm] 10/+20%	Diameter D [mm]	Length L [mm] ±0.5	Blocking force (N)	Stiffness [N/μm]	Capacitance [nF] ±20%	Resonant frequency [kHz]
P-010.80	120	10	107	2400	19	510	10

2.3 Set up of piezoelectric actuators

As mentioned in the actuator specification table, the blocking force is a force to block any displacement of the stack even in the presence of an excitation voltage applied to its terminal. This force determines the upper limit of the feasible project area, white central area in Fig.2.3. The right limit is defined by the maximum displacement of the piezoelectric stacks, i.e. the displacement when the maximum voltage is applied to its terminals.

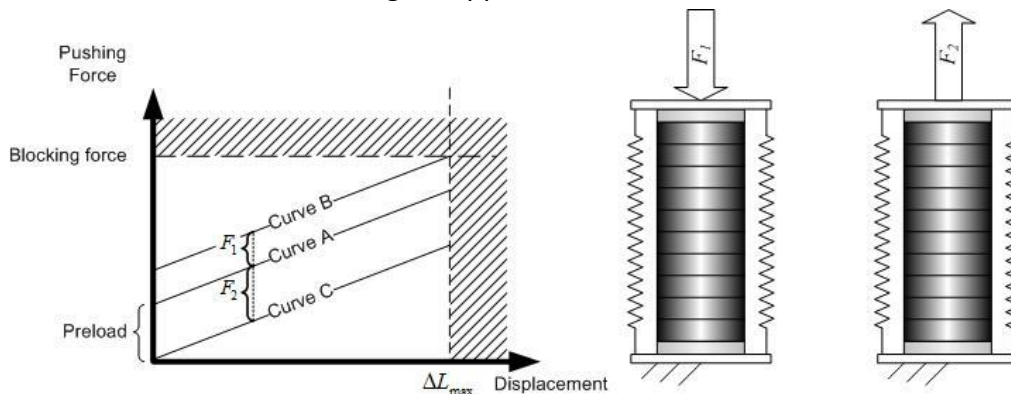


Fig.2.3 Feasible working area of the piezoelectric stack

The curve A in Fig.2.3 corresponds to a piezoelectric stack where the free end travels with the resistance imposed by the spring; this resistant force can be decomposed in the preload force and the force proportional to the spring stiffness. The inclination of curve A is related only to the stiffness. Thus adding a third component force applied to the piezoelectric stack free end causes only a shift up or down in the curve. The curve B and C are curves due to a pushing force and a pulling force respectively. Considering the limitations of the piezoelectric stacks the force F_1 in curve B is a maximum pushing force, which permits full displacement achieved by the stack. Similarly, the force F_2 in curve C is the maximum pulling force possible applied to the free end of the piezoelectric stack without exposing it to traction forces, and this force is equal to the preload force.

The scheme of working force F_W in this project is symmetric around $\Delta L_{max}/2$ as following:

$$\begin{aligned} F_W &= -F, & \Delta L &= 0 \\ F_W &= 0, & \Delta L &= \Delta L_{max}/2 \\ F_W &= F, & \Delta L &= \Delta L_{max} \end{aligned}$$

, where positive sign means pushing and negative sign means pulling.

There is the relation between F_S (force on the stack), F_m (force on the spring) and F_W (working force):

$$F_S = F_m + F_W \quad (2)$$

Denote the stiffness of the preload spring as k_m , the unloaded length of the spring as L , the length of the spring to produce the preload as L_P . Then the spring force is calculated as:

$$\Delta L_0 = L_P - L \quad (3-1)$$

$$F_m = k_m(L_P + \Delta L - L) = k_m(\Delta L_0 + \Delta L) \quad (3-2)$$

There are also the boundary conditions for stack force:

$$F_S = 0, \quad \Delta L = 0 \quad (4-1)$$

$$F_S = F_B, \quad \Delta L = \Delta L_{max} \quad (4-2)$$

, in which F_B is the blocking force.

Combining (1), (2), (3-1,2) and (4-1,2), we have:

$$k_m = \frac{F}{\Delta L_0} \quad (5-1)$$

$$\Delta L_0 = \frac{\Delta L_{max}}{F_B/F - 2} \quad (5-2)$$

ΔL_0 is required to be positive, therefore from (5) we know that the working force amplitude F has its maximum value lower than an half of the blocking force F_B . These relations are used to calculate the spring stiffness and the preload deformation in terms of the characteristics of the piezoelectric stack and the working force amplitude. It is presented in Fig.2.4 the stiffness variation due to different F_B/F . When $F = F_B/2$, the stiffness of the spring should be zero, as indicated by the curve "A" parallel to the abscissa, and the deformation to obtain the correct preload tends to infinite. On the other hand when F tends to zero, the stiffness goes asymptotically to F_B/L_{max} , as indicated in the figure. Therefore, a suitable option should equilibrate the preload spring stiffness and preload value.

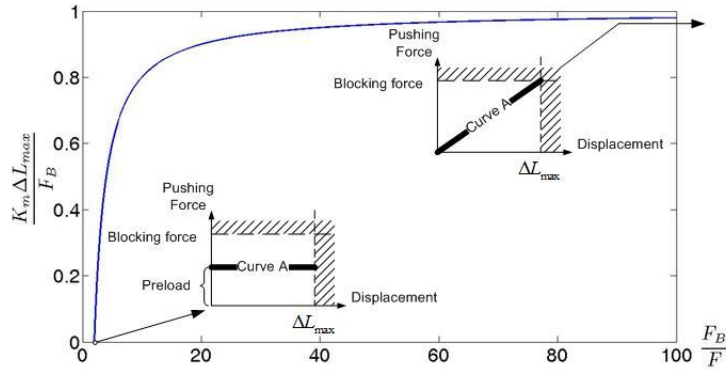


Fig.2.4 Stiffness variation along with the ratio of F_B/F

Additionally from Fig.2.5, $L = L_{pie} - \frac{F_e}{k_m} - \frac{F_e}{k_{pie}}$. (6)

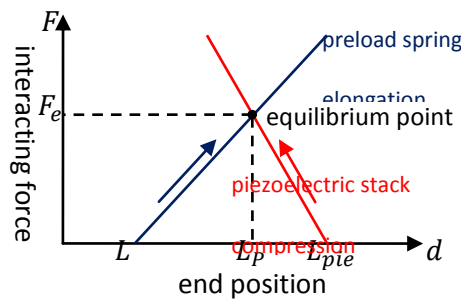


Fig.2.5 Preload scheme(force and displacement curve)

Here $F_B = 2400N$, $L_{pie} = 111.35mm$, $k_{pie} = 19N/\mu m$, $\Delta L_{max} = 120\mu m$. Notice that L_{pie} is the length of the stack plus two heights(H_8 and H_{10} shown in Fig.2.6) due to the bearing balls located between the stack and preload spring cover. From these parameters, If the preload force is set as $F = F_e = 900N$, the following initial values are calculated:

$$\Delta L_0 = 180\mu m, k_m = 5N/\mu m, L = 116.02\mu m$$

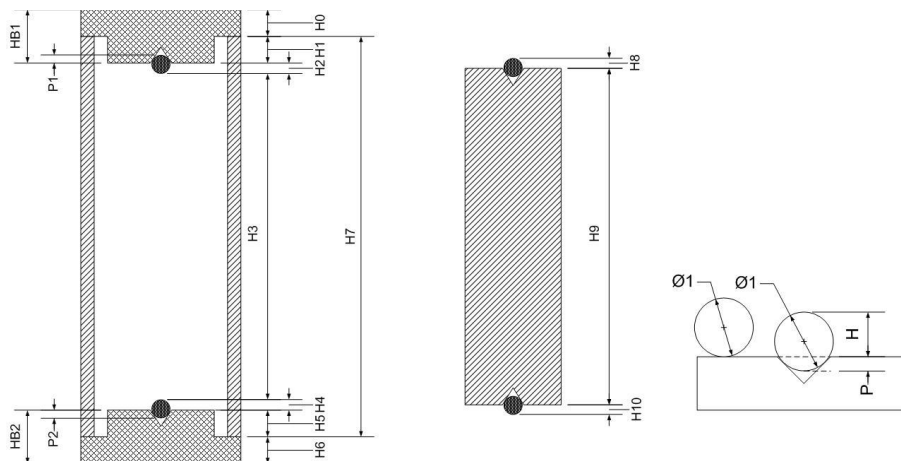


Fig.2.6 Configuration of assembling the piezoelectric stack

In order to satisfy the above mechanical properties, a basic geometric configuration of the spring is chosen a prior. The piezoelectric manufacturer PI suggests many configurations that protect the

stacks against some levels of bending and torsional loads. In this test rig, a configuration called ‘ Ω spring’ with bearing ball is adopted:

- Length L with no deformation
- Thickness t
- Pitch P
- Curvature diameter d
- Width W
- Minimum thickness a

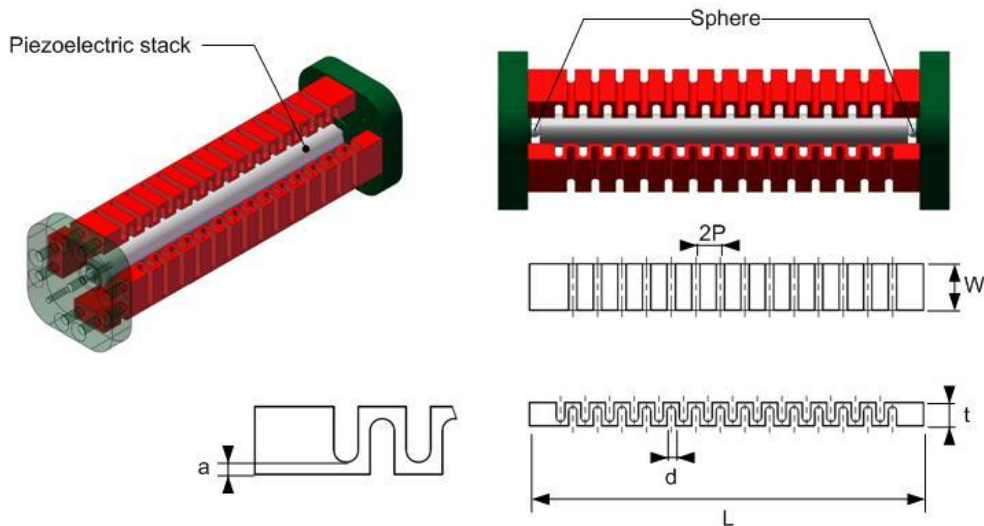


Fig.2.7 Preload spring configuration

According to the fabrication limitations the diameter " d " was settled to 2.5 mm and the length " L " was obtained from the initial calculation above. The variation of the natural frequency with the width " W " is null, and the variations of the stiffness and of the stress are linear, therefore, W was settled to 14 mm using only the fabrication requirements. In the cases where to change this value by a factor, the stress will be reduced and the stiffness will be increased by the same factor. Finally, the remaining variables are the thickness " t ", the minimum thickness " a " and the pitch " P ". Under the restriction that the first natural frequency of the preload spring component is about 500Hz, the manufacturing data determined are: $t = 7mm$, $P = 3.5m$, $a = 1.65mm$.

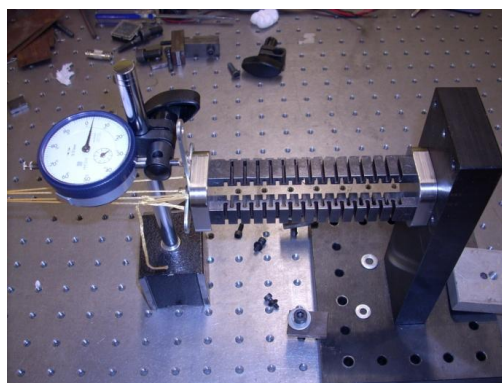


Fig.2.8 Calibration of assembled preload springs

The ‘ Ω ’ spring has a quasi infinite life when made from ASTM 52SiCrNi5 steel, of which the yield strength is 1400Mpa .

After construction the springs reach the stiffness of $4.28\text{N}/\mu\text{m}$ and $4.43\text{N}/\mu\text{m}$ for horizontal and vertical actuator and with a preload of 842N and 834N respectively, which are within the variability range of initial presumed value. Fig.2.8 shows the way to measure preload structure stiffness.

2.4 Set up of the parallel mechanism

A mechanism should be designed to impose desired displacement on the left platform. Normally, a parallel mechanism is a proper choice due to its adequate resolution, low level of parasitic forces, motion smoothness and zero backlash. There is a kind of parallel mechanisms that use flexural hinges as revolution joints recommended by some researchers. In this work, a simple parallel mechanism as represented in Fig.2.9 was chosen, in which the flexural hinges are intended to work as cylindrical joints for small displacement amplitude.

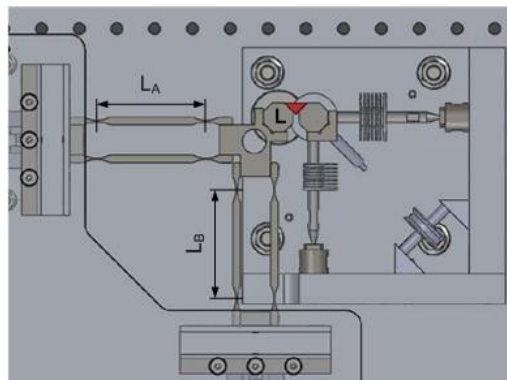


Fig.2.9 Parallel mechanism with flexural hinges

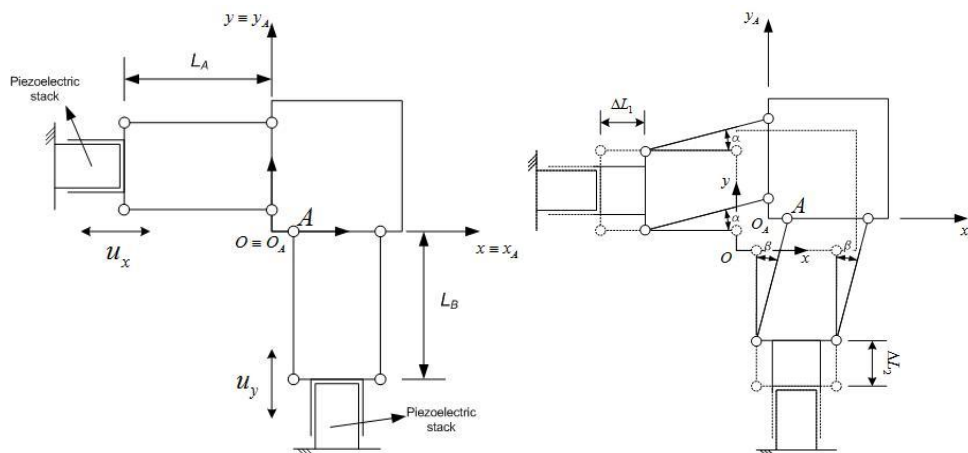


Fig.2.10 Parallel mechanism and dislocated positions

In this scheme, L_A and L_B are the lengths of the arms between the revolution joints. The revolution joints are considered in the kinematic formulation as ideal joints without clearance or

friction. The variables u_x and u_y are the imposed displacement by means of the piezoelectric stacks. Parallel configuration couples both directions even if a small displacement is applied. From Fig.2.10 a general dislocated position of the applied displacement is represented as follow:

$$\begin{aligned}x_A &= \Delta L_1 + L_A(\cos\alpha - 1) \\y_A &= \Delta L_2 + L_B(\cos\beta - 1)\end{aligned}$$

Applying the geometric relations $\sin\alpha = y_A/L_A$, $\sin\beta = x_A/L_B$, we obtain:

$$\Delta L_1 = x_A - L_A(\sqrt{1 - (y_A/L_A)^2} - 1) \quad (7-1)$$

$$\Delta L_2 = y_A - L_B(\sqrt{1 - (x_A/L_B)^2} - 1) \quad (7-2)$$

If we write in matrix form according to the first order approximation, equation (7-1,2) become:

$$\begin{Bmatrix} \Delta L_1 \\ \Delta L_2 \end{Bmatrix} = \begin{bmatrix} 1 & \frac{y_A}{L_A} \frac{1}{\sqrt{1 - (y_A/L_A)^2}} \\ \frac{x_A}{L_B} \frac{1}{\sqrt{1 - (x_A/L_B)^2}} & 1 \end{bmatrix} \begin{Bmatrix} x_A \\ y_A \end{Bmatrix} \quad (8)$$

Equation (7) or (8) shows the displacement coupling between the two directions, a possible solution to reduce this coupling effect is to increase the lengths L_A and L_B .

For example, if the lengths L_A and L_B are one hundred times larger than the displacements ΔL_1 and ΔL_2 given by the piezoelectric stack, the error of position x_A or y_A is about 1% deviated from the real value.

The detailed dimensions of the parallel component is determined by a gross Ansys 0-order optimization procedure.

A typical Ansys optimization procedure is completed by the following steps:

- (1) Create an modeling and analysis file.
 - ① Parametric modeling: Initializing the design variables(which are involved in the optimization procedure) and build up the model by corresponding parameters.
 - ② Apply load and solve.
 - ③ Go to the post-processing part, extract the result and assign the corresponding values to the constraint variables and objective function.
- (2) Form optimization control file.
- (3) Modify the design variables according to the finished optimization loops and the state of current optimization variables.

The convergence of a feasible solution is guaranteed by checking certain tolerance τ defined under different field. Assume F_j , X_j and F_{j-1} , X_{j-1} are the corresponding objective function and design variables at iteration j and $j - 1$. F_b and X_b are the optimized objective function and design variables. If $|F_j - F_{j-1}| \leq \tau$ or $|F_j - F_{j-1}| \leq \tau$, or alternatively, $|X_j - X_{j-1}| \leq \tau$ or $|X_j - X_b| \leq \tau$, the iteration searching for the optimization can be considered convergent and be stopped. τ is a tolerance defined in the relevant way.

The configuration of the parallel arm is shown in Fig.2.11. In this problem, from manufacturing point, the following dimensions are adopted: $H = 0.5mm$, $W = 40mm$, $L_2 = 54mm$, $L_3 = 9mm$.

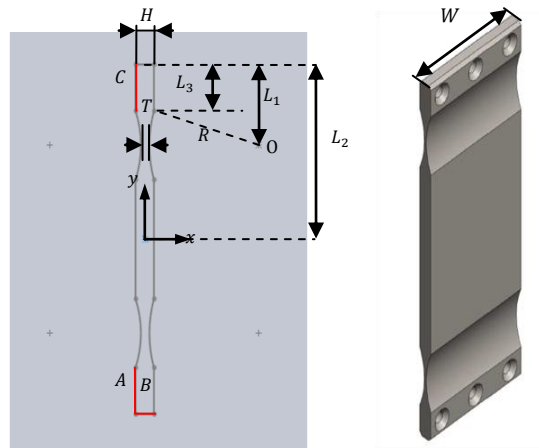


Fig.2.11 Configuration of the parallel arm

Apart from these known parameters, the parameters used in the optimization are:

Design variables: T, L_1

Objective function: F_X

State variables: f_1, σ_{1max}

F_X is the horizontal resultant force on the area A due to the horizontal displacement imposed on the area C , which represents the parasitic force of this type of mechanism; f_1 is the first natural frequency of the arm, which represents the stiffness of the structure; σ_{1max} is the maximal first principle stress of the arm.

When the static analysis is performed, according to the symmetry of structure and loading, the following simplified load conditions are adopted:

- (1) On area A , there is not displacement along x direction, that is $u_x = 0$.
- (2) On area B , there is not displacement along y direction, that is $u_y = 0$.
- (3) On area C , there is the imposed displacement along x direction with an amplitude of $80\mu m$ (considering the displacement reduction caused by the preload springs about 23% of $120\mu m$), that is $u_x = 80 * 10^{-6}$.

From the static analysis, σ_{1max} and F_X can be obtained.

When the modal analysis is performed, the following load conditions are adopted:

- (1) On area A , there is not displacement along x direction, that is $u_x = 0$.
- (2) On area B , there is not displacement along y direction, that is $u_y = 0$.
- (3) On area C , there is not displacement along x direction, that is $u_x = 0$.

From the modal analysis, f_1 can be obtained.

The initial dimensions are listed below: $T = 1.5mm$, $L_1 = 16mm$.

After the initial dimensions are input, the state variables σ_{1max} and F are calculated as: $\sigma_{1max} = 19.9\text{Mpa}$, $f_1 = 2039\text{Hz}$, and the objective function $F = 7.03\text{N}$. The stress distribution and first two mode shapes are shown in Fig.2.12 and Fig.2.13.

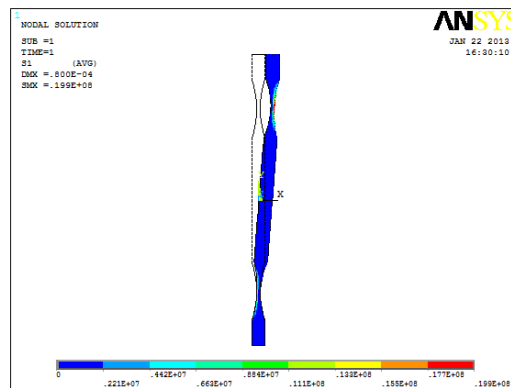


Fig.2.12 Stress distribution in the parallel arm with the initial dimension

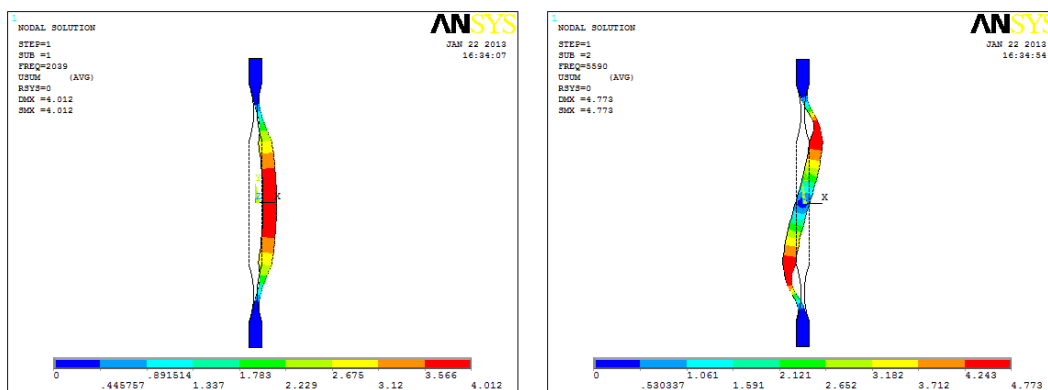


Fig.2.13 Mode shapes of the first 2 modes with the initial dimension

The practical range of design variables and state variables are given as:

$0.5\text{mm} \leq T \leq 2\text{mm}$, $16\text{mm} \leq L_1 \leq 26\text{mm}$, $f_1 \geq 1500\text{Hz}$, $\sigma_{1max} \leq 100\text{MPa}$. A gross optimization procedure is performed and after 10 iterations an optimized solution is obtained shown in Fig.2.14 and List 1.1, which has a much lower value of the objective function.

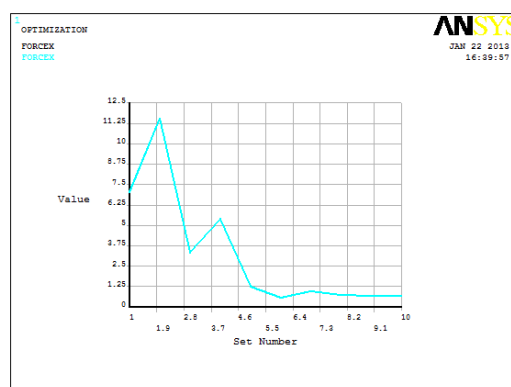


Fig.2.14 Objective function variation with the iteration

List 1.1 Optimization trace

LIST OPTIMIZATION SETS FROM SET 1 TO SET 10 AND SHOW

ONLY OPTIMIZATION PARAMETERS. (A "*" SYMBOL IS USED TO INDICATE THE BEST LISTED SET)

	SET 1	SET 2	SET 3	SET 4
	(FEASIBLE)	(FEASIBLE)	(FEASIBLE)	(FEASIBLE)
MAXSTRESS(SV)	0.19896E+08	0.19699E+08	0.14419E+08	0.16393E+08
FREQUENCY(SV)	2039.1	2162.5	1680.1	1876.9
T1 (DV)	0.15000E-02	0.17708E-02	0.10820E-02	0.13063E-02
L1 (DV)	0.20000E-01	0.21657E-01	0.23539E-01	0.22943E-01
FORCEX (OBJ)	7.0313	11.561	3.3476	5.3912

	SET 5	SET 6	SET 7	SET 8
	(FEASIBLE)	(INFEASIBLE)	(FEASIBLE)	(FEASIBLE)
MAXSTRESS(SV)	0.14531E+08	0.12337E+08	0.13122E+08	0.13523E+08
FREQUENCY(SV)	1601.0	> 1434.6	1500.2	1515.6
T1 (DV)	0.94919E-03	0.87103E-03	0.87030E-03	0.91499E-03
L1 (DV)	0.19266E-01	0.18306E-01	0.19647E-01	0.18354E-01
FORCEX (OBJ)	1.2645	0.55611	0.97291	0.75412

	SET 9	*SET 10*
	(FEASIBLE)	(FEASIBLE)
MAXSTRESS(SV)	0.13432E+08	0.13385E+08
FREQUENCY(SV)	1506.7	1503.2
T1 (DV)	0.92192E-03	0.92243E-03
L1 (DV)	0.18087E-01	0.18037E-01
FORCEX (OBJ)	0.68174	0.66407

From the optimization results, the final dimensions are adopted as:

$$T = 0.9mm, L_1 = 18mm.$$

In this way, after construction we have the length $L_A=L_B=72.3mm$, conducting to an error about 0.11%, at the maximum displacement $80\mu m$ of the piezoelectric stack.

Additionally, to prevent spurious movement in other directions a suspension to guide the piezoelectric displacement and increase the stiffness in other directions. The suspension is composed by double cross shown in Fig.2.15.

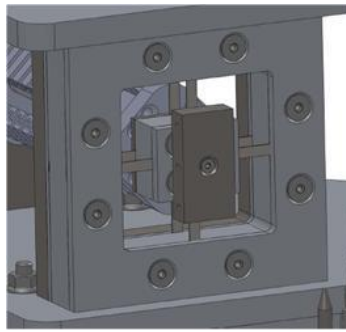


Fig.2.15 Double cross suspension

The parallel mechanism and double cross suspension will prevent the rotation of the left-platform to minimum.

2.5 Set up of the force measurement structure

The function of force measurement structure is to get the force transmitted by the damper through the interface between damper and right-platform. Piezoelectric force sensors are placed in the manner to form a Cartesian frame. The right platform, which has three threaded holes on the respective surfaces, is linked to three rods which have one threaded end with a nut. Then the rods are supported by two force sensors connected to two wall bases and one cylindrical extrusion connected to the ground.

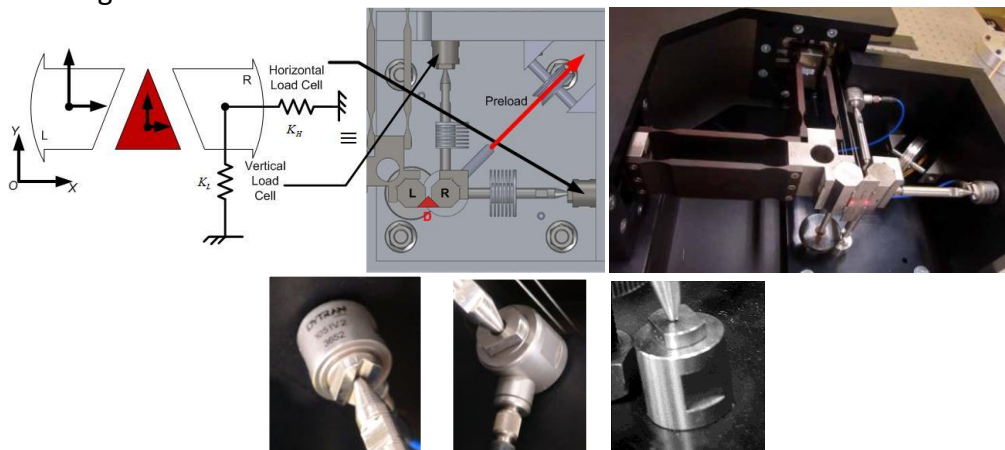


Fig.2.16 Force measurement structure

Fig.2.16 is a demonstration of the force measurement structure. From the top view, the horizontal and vertical load cells have a top cap for each, one has an in-plane straight slot which provides two kinematic constraint and the other one has a spherical concave on the surface which provides three kinematic constraint. The cap of the cylindrical extrusion has a flat surface which gives one kinematic constraint. Thus the free tripod frame(6 DOF) follows a complete kinematic constraint condition. Additionally, the lengths of the three rods are adjusted by fixing the respective nut. Once the height of the rod perpendicular to the movement plane is determined with an acceptable tolerance, the tripod constructs a regular Cartesian system.

A preload is then applied to make the respective rod and load cell in compression to guarantee the contact between them during operation. The preload is supplied by a deadweight-pulley mechanism. The tangent line of the preload wire passes through the center of the tripod to avoid

lateral force on the load cell. Losses due to friction in the pulley and uncertainties in the dead weight are negligible to the total preload.

The force sensors used in this test rig(Dytran 1051 V2) has technical specifications as follows:

Table 2.2 Force sensor specifications

MODEL	SENSITIVITY (N/V)	COMPRESSION RANGE(N)	MAX.COMP.(N)	TENSION RANGE(N)	MAX.TEN.(N)	DISCH. TC(sec)	RESOLUTION (N, RMS)
1051V2	44.48	2224	44480	2224	4448	100	0.0007

When the leakage of a charge (or voltage) occurs in a resistive capacitive circuit, the leakage follows an exponential decay. A piezoelectric force sensor system behaves similarly in that the leakage of the electrostatic charge through the lowest resistance also occurs at an exponential rate. The value of the electrical capacitance of the system (in farads), multiplied by the value of the lowest electrical resistance(in ohms) is called the Discharge Time Constant (in seconds).

DTC is defined as the time required for a sensor or measuring system to discharge its signal to 37% of the original value from a step change. This is true of any piezoelectric sensor, whether the operation be force, pressure or vibration monitoring. The DTC of a system directly relates to the low frequency monitoring capabilities of a system and, in the case of force monitoring, becomes very important as it is often desired to perform quasi-static measurements.

According to PCB force sensor calibration technique, miniature or high sensitivity models are calibrated by applying a known lightweight mass, letting the signal zero, and then quickly removing the mass. Output recorded is the sensitivity of the sensor. Based on this, a structure of relevant configuration is designed as in figure 2.17.

A calibrated weight is applied on the force sensor through a symmetric frame. The point contact between cover component and force sensor guarantees that momentum imposed on the sensor is negligible. The length of parallel wires and the width of cover component are long enough to make sure that the lateral force at the contact point is negligible. The special bearing pulley prevent the effect of friction to the minimum.

The sensitivity of the sensor S combined with the signal conditioner is then obtained though dividing the force drop ΔF by the voltage drop ΔV .

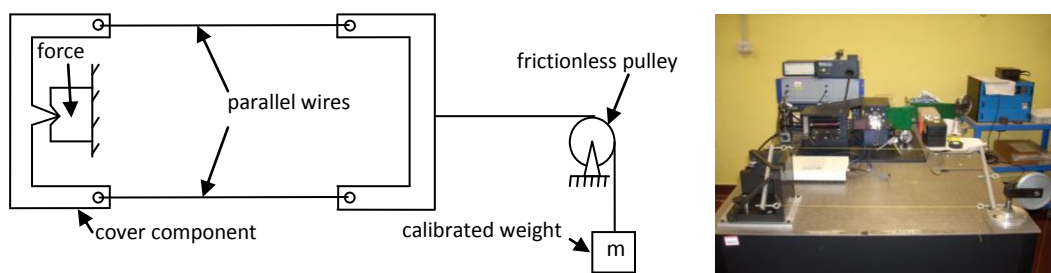


Fig.2.17 Scheme recalibrating the force sensor

From the theory of propagation of uncertainties, given the objective function

$$X = f(A, B, C, \dots)$$

and the uncertainty(standard deviation) of each variables $\sigma_A, \sigma_B, \sigma_C, \dots$, then the uncertainty of function X is calculated as:

$$\sigma_X^2 = \left(\frac{\partial f}{\partial A} \sigma_A\right)^2 + \left(\frac{\partial f}{\partial B} \sigma_B\right)^2 + \left(\frac{\partial f}{\partial C} \sigma_C\right)^2 + \dots \quad (9)$$

Here $S = \frac{\Delta F}{\Delta V}$, applying the above formulation, the following is obtained

$$\sigma_S = \sqrt{\left(\frac{1}{\Delta V} \sigma_F\right)^2 + \left(\frac{\Delta F}{\Delta V^2} \sigma_V\right)^2} \quad (10)$$

The tests are repeated for three times under the same condition. Here we assume that the uncertainty of force drop caused by the friction through the pulley and the response time is less than 1%. Based on these the average and uncertainty of the sensor sensitivity are obtained. Fig.2.18 shows an example of the test results.

Table 2.3 Force sensor calibration

	voltage drop		force drop		sensitivity (force jump/voltage jump)	
	Average(V)	SD(V)	Average(N)	SD(N)	Average(N/V)	SD(N/V)
horizontal sensor	0.94	0.024	39.4	0.4	41.9	1.15 (2.7%)
vertical sensor	1.24	0.024	56.1	0.6	45.2	1.00 (2.2%)

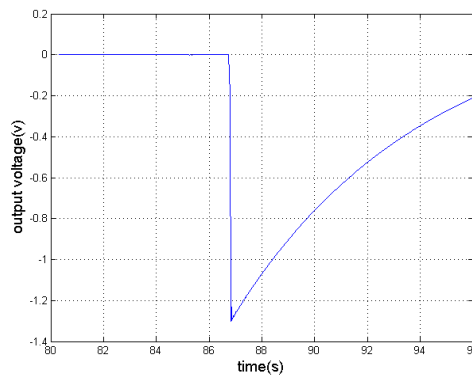


Fig.2.18 Representative load removal(weight of 5.72kg) result

Since the piezoelectric force sensors are designed for dynamical measurement, the load removal performance can be used to get the real force of a damper acting on the platform, which is useful to investigate the damper equilibrium.

Apart from the other factors, the uncertainty of measured dynamical force due to sensitivity is less than 3%.

2.6 Test rig calibrations

After the total test rig is assembled, it is important to check the test rig performance by investigating the mechanical property and operation range. Before demonstrating the calibration results, an introduction of laser vibrometer is given.

A laser Doppler vibrometer (LDV) is a scientific instrument that is used to make non-contact vibration measurements of a surface. The laser beam from the LDV is directed at the surface of interest, and the vibration amplitude and frequency are extracted from the Doppler shift of the laser beam frequency due to the motion of the surface. The output of an LDV is generally a continuous analog voltage that is directly proportional to the target velocity component along the direction of the laser beam[Wikipedia].

Single-point vibrometers measure the amount of vibration at a single point on an object's surface. More specifically, a laser vibrometer measures the projected component of an object's surface vibration vector along the direction of the incident laser beam. For example, if aligned perpendicularly to surface under test, the vibrometer measures the out-of-plane vibration to the surface (the instrument is sometimes referred to as an out-of-plane vibrometer. A differential vibrometer is used to measure the movement of a point relative to a reference point. The differential vibrometer can be used as single-point vibrometer when then reference laser head is covered by a specified cap.

In the work of this thesis, a differential laser vibrometer with controller Polytec OFV-3001 and sensor head OFV-512 is used. The displacement decoder inside the controller is OVD-20, of which the technical data are listed in Table 2.4.

Table 2.4 Specification of laser displacement decoder used in the test

Displacement decoder	Measurement range (scaling factor) $\mu\text{m/V}$	Full scale output (peak-peak)	Resolution μm	Maximum velocity m/s	Band width KHz	Maximum frequency for specified accuracy KHz	Amplitude linearity
OVD-20	20	320	0.08	2.5	0-250	100	± 1 increment

In the operation range of this test rig, this laser vibrometer is sensitive and precise enough to give correct displacement measurement. Maximally, when the measured body moves in harmonic way at 200Hz with amplitude(P-P) of $200\mu\text{m}$, the maximal velocity is $100 \times 10^{-6} (2\pi) \times 200 = 4\pi \times 10^{-2} \text{m/s}$, safely lower than the limit.

2.6.1 Piezoelectric actuator and force sensor operation range

To get the dynamic calibration factor (the ratio between output displacement and input excitation) of the piezoelectric actuator combined with the auxiliary structure (preload springs, suspension and parallel arms), tests are performed as follows: using a random noise excitation as input signal for the piezoelectric actuator, the transfer function is obtained through dividing the cross spectrum between the input and the output by the input auto spectrum. The output displacement is measured by a laser Doppler vibrometer. The test results are shown in Fig.2.19 and Fig.2.20.

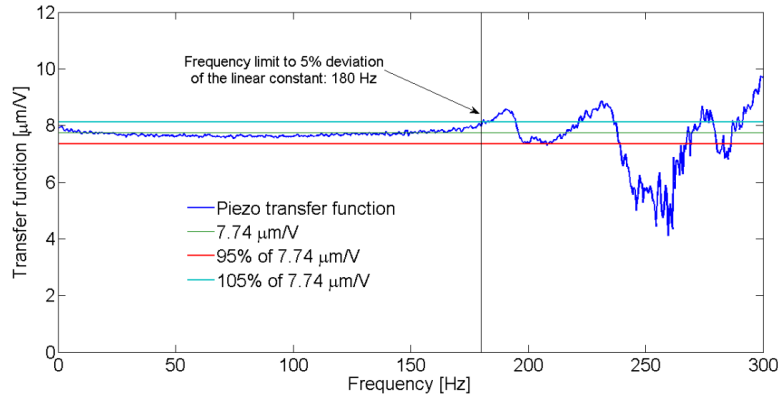


Fig.2.19 Dynamic calibration result of horizontal piezoelectric actuator with auxiliary structure

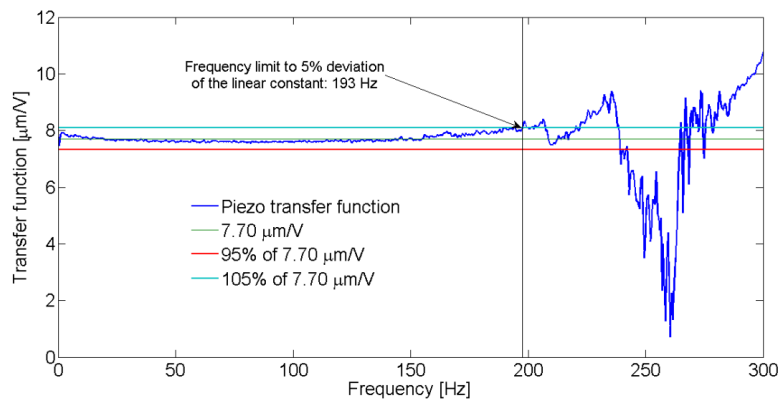


Fig.2.20 Dynamic calibration result of horizontal piezoelectric actuator with auxiliary structure

In the 5% linear range around the averaged value of the calibration factor $C_h = 7.74\mu\text{m}/V$ and $C_v = 7.70\mu\text{m}/V$, the horizontal actuator can work under 180Hz and the vertical actuator can work under 193Hz.

After knowing this dynamical factor, it is convenient to measure the real movement on the left-platform without external force. Considering the similarity between horizontal and vertical actuator chain, here only the horizontal direction is measured.

The measured signal compared with the excitation signal is shown in Fig.1.21. The results show that the dynamic calibration factor is reliable (all slopes are within 5% deviation range of $7.74\mu\text{m}/V$). When the actuator has no close loop control, the inner hysteresis due to material polarization causes deviations to harmonic input. The proportion of largest deviation from the center displacement Δd_{max} to the respective amplitude is about 30%, which can be overcome in the future by close loop control to the piezo-electric actuator.

Fig.2.21 shows the hysteresis behavior of displacement produced by the piezoelectric actuator without closed-loop control.

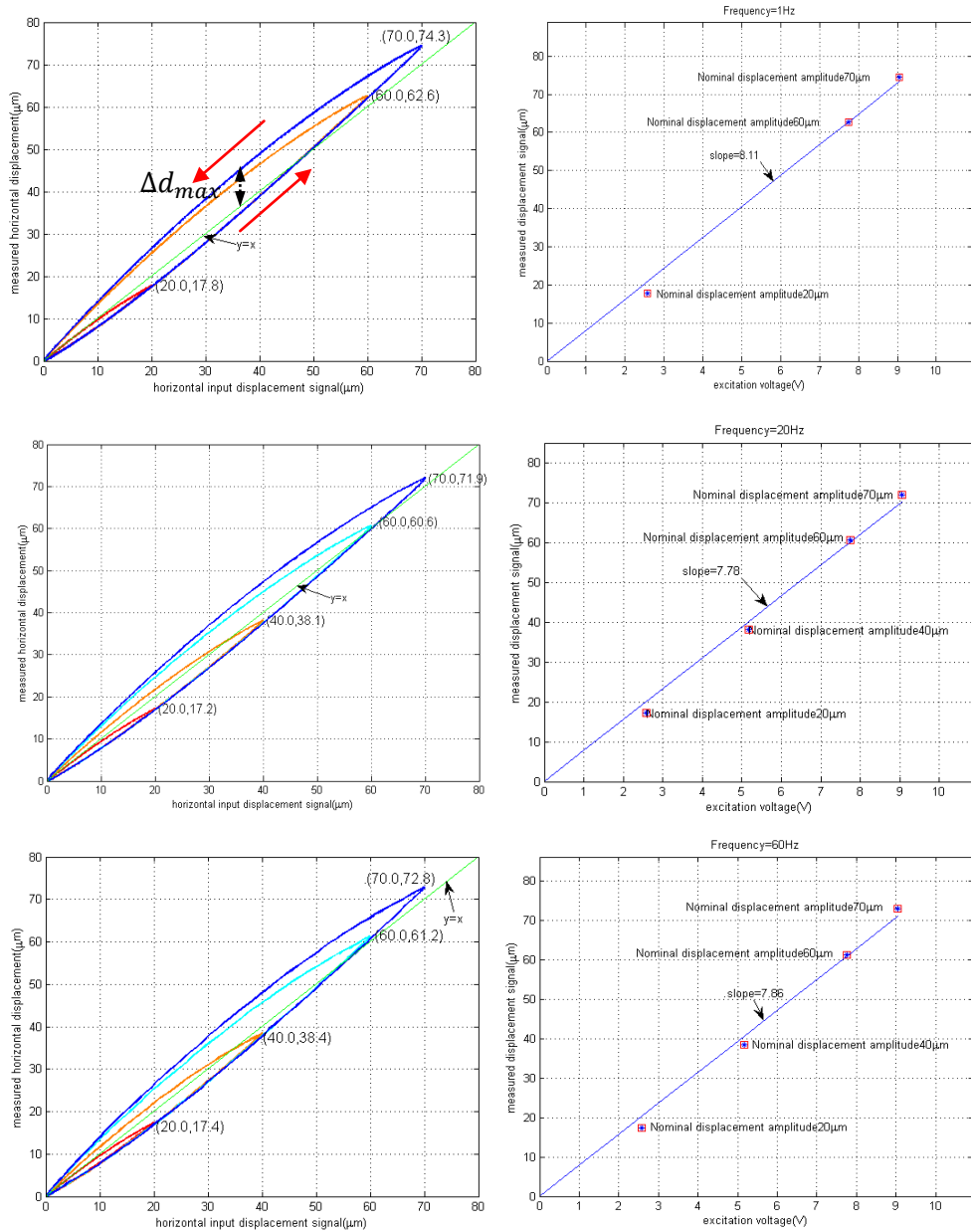


Fig.2.21 motion hysteresis of horizontal actuator under different frequency

A rough hammer test is used to check the frequency working range of the force sensor connected with the tripod and respective support. Since a force sensor is also mounted on the tip of the hammer, when an impact is applied by the hammer to the structure. The frequency response is given by dividing the output spectrum measured from the sensor in the structure by the auto spectrum of the impact input measured from the hammer sensor. The result for horizontal sensor is shown in Fig.2.22.

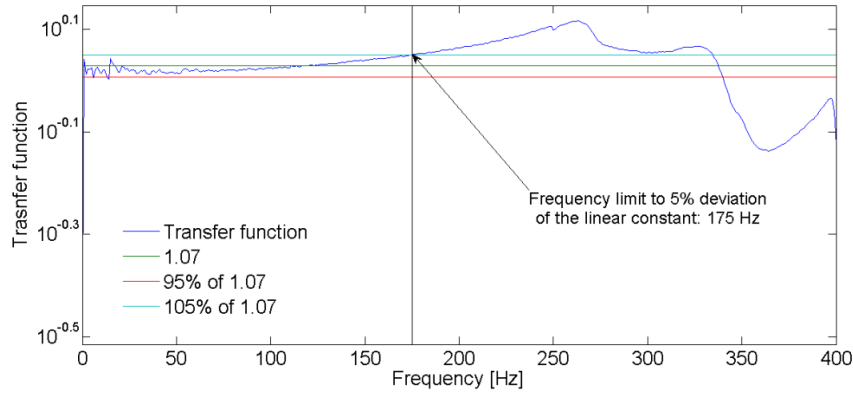


Fig.2.22 Transfer function by the hammer test for horizontal force sensor

An ideal hammer test can have a configuration that the hammer is suspended as a pendulum and the impact is realized by the gravity of the hammer. But here we roughly apply the impact on both directions manually since we need only the information of the sensitivity linearity range. After the tests, both sensors can work in a 5% linearity variation range below 175Hz.

2.6.2 Stiffness distribution in the test rig

In Fig.2.23, m_1 is the mass of damper, m_2 is the mass of right platform, the mass of guiding rod is neglected and regarded as a spring that has a stiffness of k_3 , m_3 is the mass of force sensor plus the effective mass of supporting wall. And k_4 is the equivalent stiffness of the force sensor and supporting wall. The damping in the structure is not shown.

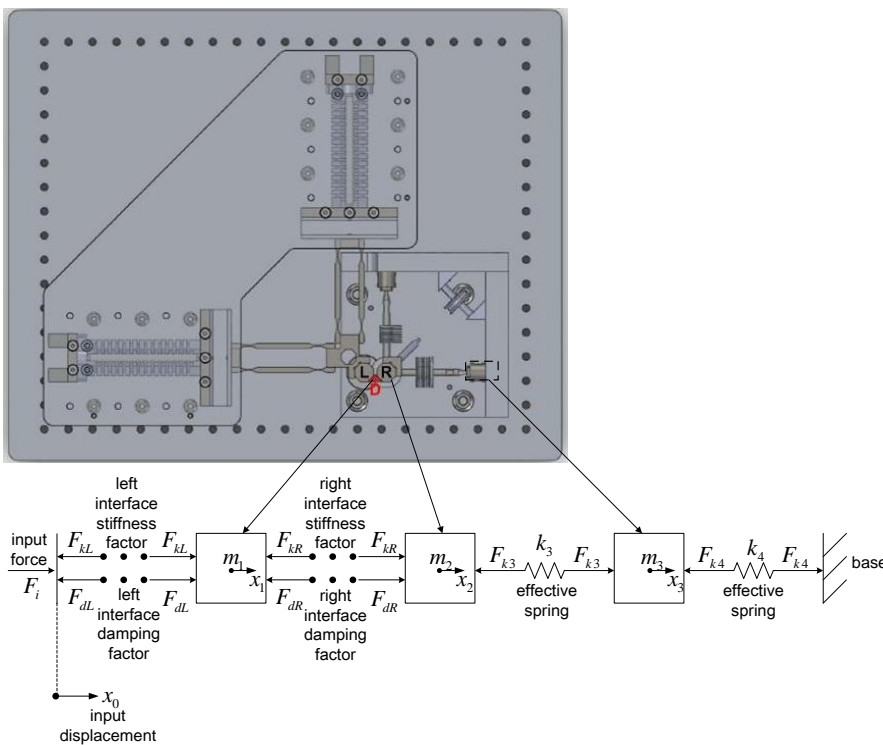


Fig.2.23 Demonstration of discrete model parameters of the test rig

Assuming initially each mass is at its equilibrium point with necessary preload, the motion equations of the system is as follows:

$$\begin{cases} m_1\ddot{x}_1 + F_{kR} + F_{dR} = F_{kL} + F_{dL} \\ m_2\ddot{x}_2 + F_{k3} = F_{kR} + F_{dR} \\ m_3\ddot{x}_3 + F_{k4} = F_{k3} \end{cases}$$

And there is the force relation $F_i = F_{kL} + F_{dL}$, consequently,

$$F_{k3} = F_{kR} + F_{dR} - m_2\ddot{x}_2$$

F_{k3} is the force measured by force sensor. The difference between it and the real force at right interface is the inertial force of m_2 .

The energy consumed by the damper and two interfaces in one period is:

$$E_c = \int_T F_i \cdot dx_0 - (F_{kR} + F_{dR}) \cdot dx_2$$

Substitute F_i , F_{kR} and F_{dR} by F_{k3} , the energy is expressed as

$$E_c = \int_T (F_{k3} + m_1\ddot{x}_1 + m_2\ddot{x}_2) \cdot dx_0 - (F_{k3} + m_2\ddot{x}_2) \cdot dx_2$$

If the kinetic energy of mass m_2 and m_3 are negligible, the formulation becomes

$$E_c = \int_T F_{k3} \cdot d(x_0 - x_2) \quad (11)$$

It is shown by equation (11) that linking the relative displacement between left platform and right platform and transmitted force to the force sensor to illustrate the interface characteristics is reasonable.

Under low frequency operation range, the mass and damping parameters are not important, while the stiffness of test rig components can influence the measurement features through changing the relative displacement between two platforms, which is a consequence of contact force increase.

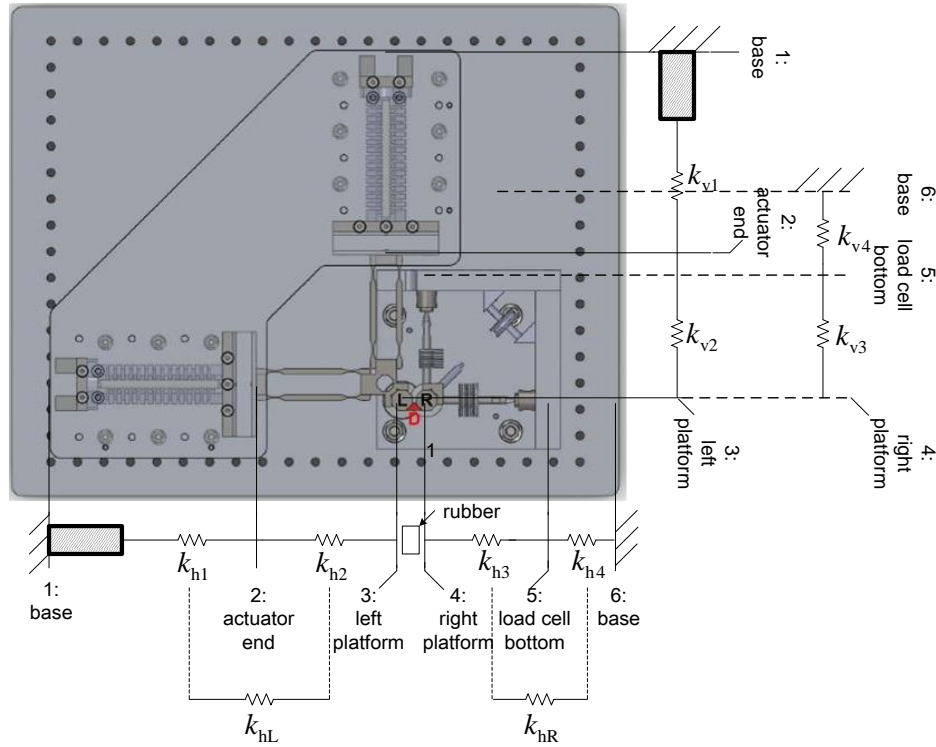


Fig.2.24 Demonstration of stiffness distribution in the operation chain

According to the results in design stage, the preload springs for the horizontal actuator have a total stiffness of $4.28\text{N}/\mu\text{m}$ and the preload springs for the vertical horizontal actuator have a total stiffness of $4.43\text{N}/\mu\text{m}$. The stiffness of the piezoelectric stack used is $19\text{N}/\mu\text{m}$. The parallel combination of piezoelectric stack and preload springs has a stiffness of about $23\text{N}/\mu\text{m}$ which is very stiff, but the connection interfaces along the operation chain may reduce the total stiffness. The stiffness distribution is demonstrated in Fig.2.24. The two rectangles with shadow slash inside represent the ideal piezoelectric stacks which produce deformations only depending on the imposed voltage. k_{h1}, k_{v1} is the respective resultant stiffness of each stack with preload system. k_{h2}, k_{v2} is the respective stiffness of each parallel pushing arm. Respectively, k_{h1} and k_{h2} can be integrated as k_{hL} ; k_{h3} and k_{h4} can be integrated as k_{hR} ; k_{v1} and k_{v2} can be integrated as k_{vL} ; k_{v3} and k_{v4} can be integrated as k_{vR} .

To implement the calibration, two pieces of rubber are put between the platforms with pre-compression. The inertial effect of mass is ignored along the operation chain. So the force measured from force sensor can be used to estimate the chain stiffness in different sections.

Neglecting the damping between 4 and 6, the measured displacement at points 4 and 5 has the same phase with measured force. Denote F_{P-P} as the peak to peak amplitude of measured force and d_{P-P} as the peak to peak amplitude of measured displacement. The stiffness between the specified two points is:

$$k = \frac{F_{P-P}}{d_{P-P}} \quad (12)$$

This can be used to estimate k_{h3} , k_{h4} and k_{hR} .

For k_{hL} , consider imposing the same nominal amplitude from the actuator and denote the measured displacement amplitude of point 3 without external force as d_{P-P}^0 and the respective amplitude under external force produced by the rubber as d_{P-P}^1 .

It is noticed that the viscous damping effect of the rubber is not negligible. So the phase shift between measured displacement at point 3 and measured force has to be taken into account. Fig.2.25 demonstrates the situation.

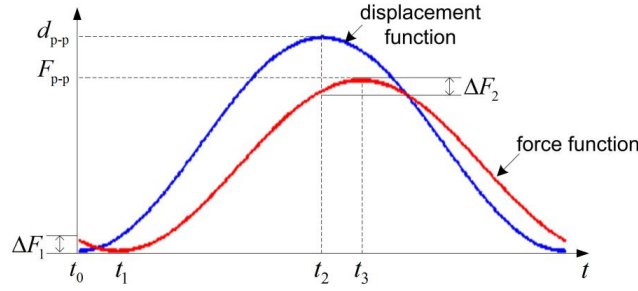


Fig.2.25 Demonstration of phase shift between force and displacement signal

The formulations of d_{P-P}^0 and d_{P-P}^1 are following:

$$d_{P-P}^0 = C_h \Delta V$$

$$d_{P-P}^1 = d_{P-P}^0 - \frac{F_{P-P} - \Delta F_1 - \Delta F_2}{k_{hL}}$$

In which C_h is the calibration factor of the horizontal piezoelectric stack obtained in previous section. ΔV is the maximum voltage with respect to a certain nominal amplitude of displacement.

Then the stiffness is formulated as:

$$k_{hL} = \frac{F_{P-P} - \Delta F_1 - \Delta F_2}{d_{P-P}^0 - d_{P-P}^1} \quad (13)$$

Regarding to the horizontal direction, practical measurement position for point 2 is on the interface between actuator and pushing arm, for point 3 is on the cube attached to the left platform top, for point 4 is on the cube attached to the right platform top, for point 5 is on the bottom of force sensor.

The test results give $k_{hL} = 4.7 \pm 0.2 \text{ N}/\mu\text{m}$, $k_{hR} = 8.7 \pm 0.2 \text{ N}/\mu\text{m}$.

Fig.2.26 shows the real horizontal displacement given by the actuator when the rubber is located between the platforms. The reduction of displacement can be compensated by closed-loop control to the actuator, which is not implemented in this thesis.

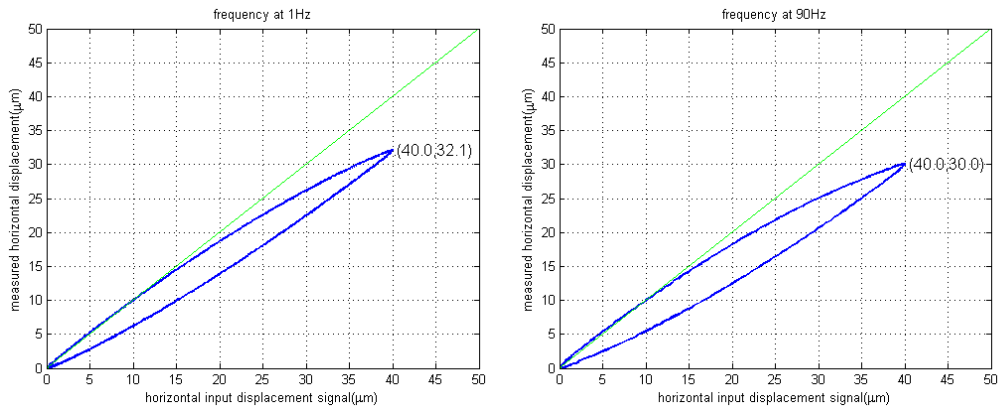


Fig.2.26 Demonstration of actuator displacement under external force

2.7 Check of the synchronicity of measured signals

Originally, the test rig is expected to give the relative displacement between the two platforms as the output displacement by the piezoelectric actuator, but due to the flexibility of the manufactured structures, it is necessary to measure the relative movement between the two platforms. So there are two kinds of signals to be measured, one is the displacement from laser and the other is the force from force sensor.

The data acquisition is realized by NI USB-6289 board and corresponding Labview program. Although the innate hardware lag in the chain between NI board and physical devices such as voltage amplifiers is negligible, it is checked before performing damper tests to avoid spurious hysteresis between displacement and force signal.

Again by using the laser, a square wave is applied to the actuator, when the input square signal changes its direction at the corner, there will be abrupt change at the same time for both displacement and force signal. Fig.2.28 shows a representative measurement under the following condition:

Excitation frequency: 0.5Hz

Excitation nominal amplitude(peak to peak): $40\mu\text{m}$

Sample frequency of generation: 1000Hz

Sample frequency of measurement: 1000Hz

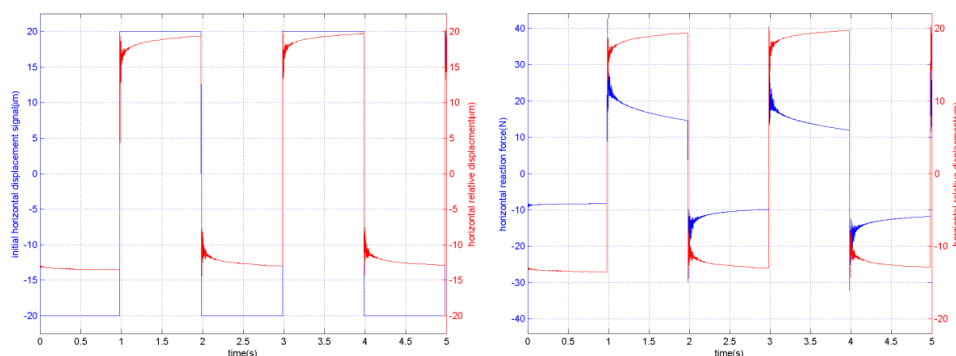


Fig.2.27 Example of signal synchronicity check

The tests show that the generation and acquisition time delay for different channels can be neglected within at least the range of 1ms.

2.8 Conclusions

The test rig is designed with the purpose of giving certain forms of displacement to the simulated platform and measuring forces transmitted to the simulated right platform through the damper.

To reduce the influence of the test rig structure to the damper and corresponding interfaces, the left platform and right platform are two octagon shaped hard steel with small mass.

The piezoelectric actuators, together with preload springs, double cross suspension and parallel mechanism guarantee accurate horizontal or vertical movement to the left platform. Potentially the combination of the two direction's movement produces any trajectory in plane. The compliance calibration shows the weak point of this part, which has integrated stiffness times lower than the design value. The dynamic calibration shows both actuators can work in a linear range until about 190Hz.

The piezoelectric sensors, together with force conducting tripod and preload device, is capable to measure the dynamic forces though the right platform in a linear range below 175Hz. Possible errors of the force measurement will be discussed in next chapter.

The synchronicity of force and displacement signals is guaranteed.

Chapter 3 Measurement error analysis

3.1 Measurement of relative movement between the two platforms

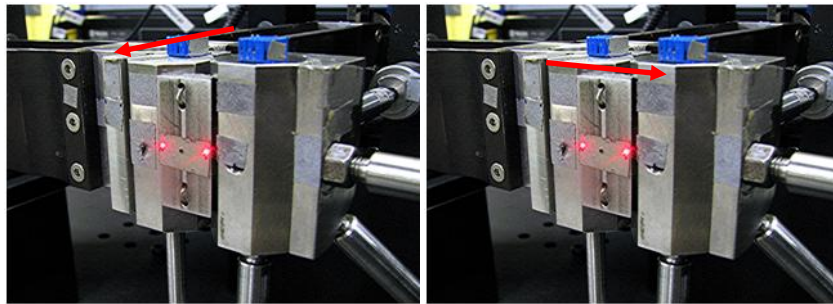


Fig.3.1 Demonstration of in-phase(left) and out-of-phase(right) motion

As mentioned in chapter 2, the measured force from the force sensor and corresponding movement between the two platforms form a dual-interface hysteresis representing the contact properties between damper and two platforms. When the relative movement of the two platforms is measured by the differential laser, there can be an inclination between operation direction and correct projection direction of the laser beams.

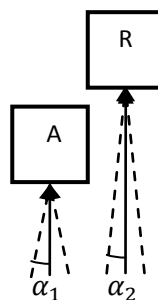


Fig.3.2 Projection error

Fig.3.2 shows the situation when the direction of laser beams is deviated from the correct direction. Denote the motion amplitude of body A and the reference body R as A_1 and A_2 , the measurement value will be $A_1(1 - \cos\alpha_1)$ and $A_2(1 - \cos\alpha_2)$ respectively. α_1 and α_2 are limited to 2° , for single point measurement, the relative error is less than $1 - \cos(2^\circ) \approx 0.06\%$, which is

practically negligible. This also holds for differential measurement. In the following sections, this projection error is not considered.

3.2 Measurement of damper kinematics

3.2.1 Parallax error

Here a wedge shaped under-platform damper, which is mostly used in gas turbine industry, is investigated to demonstrate the parallax error by laser measurement, shown In Fig.3.2.

During oscillations, the damper may move both horizontally and vertically and allow some rotation. Due to the combination of the movement, the actual projected point of laser beam is changing, which could be a source of measurement error. The laser is used to measure the vertical movement component of the projected point.

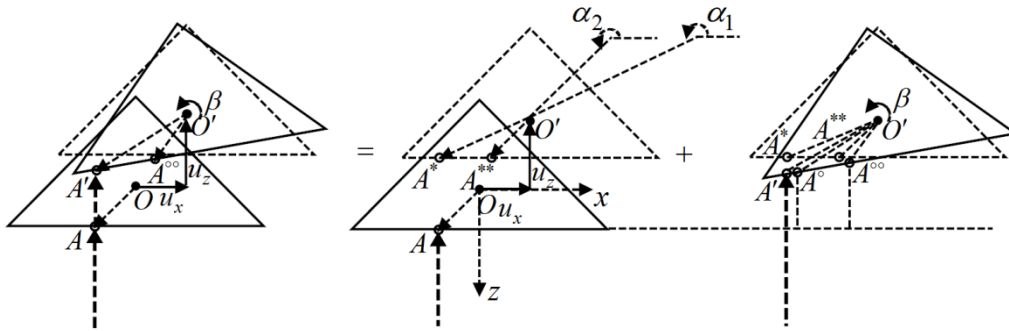


Fig.3.2 Measurement of vertical movement at a point on the damper

First consider the vertical movement at a point on the damper bottom. Denote point A as the initial position where the laser beam is projected to the damper. $O(0,0)$ is the initial position of the damper mass center and origin of the fixed coordinate system, base on which the coordinates of each point in Fig.3.2 are established.

The coordinates of A are (x_A, z_A) . If O moves u_x and u_z respectively in the horizontal and vertical direction, we have:

$$O'(u_x, u_z), A^{**}(x_A + u_x, z_A + u_z), A^*(x_A, z_A + u_z)$$

Then when the damper has a rotation angle of β , the following geometric relations stand:

$$\overrightarrow{O'A^{oo}} = \overrightarrow{O'A^{**}} e^{i\beta}, \overrightarrow{O'A^o} = \overrightarrow{O'A^*} e^{i\beta}$$

The vector $\overrightarrow{O'A^{**}}$ has components $\begin{Bmatrix} x_A \\ z_A \end{Bmatrix}$, and the vector $\overrightarrow{O'A^*}$ has components $\begin{Bmatrix} x_A - u_x \\ z_A \end{Bmatrix}$. They can be expressed in complex number as:

$$\overrightarrow{O'A^{**}} = r_2 e^{i\alpha_2}, \overrightarrow{O'A^*} = r_1 e^{i\alpha_1}$$

, in which $r_2 = \sqrt{x_A^2 + z_A^2}$, $\cos\alpha_2 = \frac{x_A}{r_2}$, $\sin\alpha_2 = \frac{z_A}{r_2}$ and $r_1 = \sqrt{(x_A - u_x)^2 + z_A^2}$, $\cos\alpha_1 = \frac{x_A - u_x}{r_1}$, $\sin\alpha_1 = \frac{z_A}{r_1}$.

Thus the vectors $\overrightarrow{O'A^{oo}}$ and $\overrightarrow{O'A^o}$ are expressed as: $\overrightarrow{O'A^{oo}} = r_2 e^{i(\alpha_2 + \beta)}$, $\overrightarrow{O'A^o} = r_1 e^{i(\alpha_1 + \beta)}$.

The coordinates of point A^{oo} and A^o are respectively:

$$A^{oo}(r_2 \cos(\alpha_2 + \beta) + u_x, r_2 \sin(\alpha_2 + \beta) + u_z)$$

$$\tan\beta = \frac{\delta z_{A_L A_R}}{d} \quad (3)$$

The measurements of vertical movement at a point on the damper bottom and damper rotation can be used to reconstruct the total motion of the damper as a rigid body, which contains two translations and one rotation in plane.

3.2.2 Reconstruction of damper motion and error factors

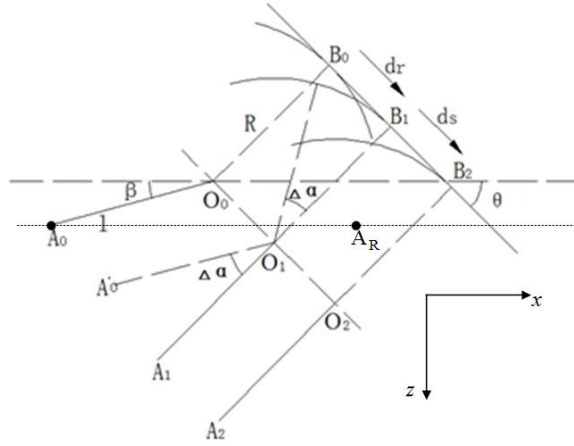


Fig.3.4 Damper motion decomposition

The dampers used in the experiments have a curved surface on the right side, which provides a known contact region on this surface.

We assume that the damper is always in contact with the right-platform, which can be verified by the experiment if there is no pure decay interval in the measured force signal. In this sense, the relative movement between contact point on the damper right surface and contact point on the right-platform comprises from two parts: pure rolling and pure translation.

In Fig.3.3, before movement point A_0 is the point where laser beam is projected on the damper to get z direction movement component; point A_R is the point as the reference on the damper to measure rotation; point O_0 is the center of the curved surface line; B_0 is the contact point. l is the distance between A_0 and O_0 . β is the angle between line $\overline{O_0 A_0}$ and the horizontal line. θ is the inclination angle of the platform edge. Notice that in this section the definition of angle β and α will be different from last section.

To demonstrate the relations between measured quantity and induced quantity, introduce the following coordinates: (x_{A_0}, z_{A_0}) , $(x_{A_0'}, z_{A_0'})$, (x_{A_1}, z_{A_1}) , (x_{A_2}, z_{A_2}) .

For rolling, from Fig.3.3, the contact point changes from B_0 to B_1 with a rotation angle of $\Delta\alpha$, the curve center O_0 moves to O_1 , the auxiliary line $\overline{O_1 A_0'}$ is translated from the line $\overline{O_1 A_0}$ and line $\overline{O_1 A_1}$ is rotated counterclockwise by $\Delta\alpha$ from $\overline{O_1 A_0'}$. From the geometric relations we have :

$$dr = |O_0 O_1| = |B_0 B_1| = R\Delta\alpha$$

and further

$$\begin{cases} x_{A_1} - x_{A_0} = R \cdot \Delta\alpha \cdot \cos(\theta) + l \cdot \cos(\beta) - l \cdot \cos(\beta + \Delta\alpha) \\ z_{A_1} - z_{A_0} = R \cdot \Delta\alpha \cdot \sin(\theta) + l \cdot \sin(\beta + \Delta\alpha) - l \cdot \sin(\beta) \end{cases} \quad (4)$$

When the displacements are small, the relation is simplified as:

$$\begin{cases} x_{A1} - x_{A0} = R \cdot \Delta\alpha \cdot \cos(\theta) + l \cdot \sin(\beta) \cdot \Delta\alpha \\ z_{A1} - z_{A0} = R \cdot \Delta\alpha \cdot \sin(\theta) + l \cdot \cos(\beta) \cdot \Delta\alpha \end{cases} \quad (5)$$

For the translation, the contact point moves from B_1 to B_2 covering a distance of ds , the curve center O_1 moves to O_2 and the line $\overline{O_1A_2}$ is translated from line $\overline{O_1A_1}$. From the geometric relations we have:

$$\begin{cases} x_{A2} - x_{A1} = ds \cdot \cos(\theta) \\ z_{A2} - z_{A1} = ds \cdot \sin(\theta) \end{cases} \quad (6)$$

The total movement is composed by the two parts, giving:

$$\begin{cases} x_{A2} - x_{A0} = (x_{A1} - x_{A0}) + (x_{A2} - x_{A1}) = R \cdot \Delta\alpha \cdot \cos(\theta) + l \cdot \sin(\beta) \cdot \Delta\alpha + ds \cdot \cos(\theta) \\ z_{A2} - z_{A0} = (z_{A1} - z_{A0}) + (z_{A2} - z_{A1}) = R \cdot \Delta\alpha \cdot \sin(\theta) + l \cdot \cos(\beta) \cdot \Delta\alpha + ds \cdot \sin(\theta) \end{cases} \quad (7)$$

Let $h = l \cdot \cos(\beta)$. Denote the x direction displacement point A_0 as u_{A0} , the z direction displacement of point A_0 as w_{A0} , the differential vertical movement between point A_0 and reference point A_R as $\delta w_{A_0A_R}$. The horizontal distance between point A_0 and A_R is d . The horizontal distance between point A_0 and O_0 is h . w_{A0} and $\delta w_{A_0A_R}$ are measured movement quantities. d and h are measured geometric quantities.

The correspondence between the quantities formulated in (5)-(7) and the measured quantities are:

$$z_{A2} - z_{A0} = w_{A0} \quad (8)$$

$$\Delta\alpha = \frac{\delta w_{A_0A_R}}{d} \quad (9)$$

$$ds = \frac{w_{A0} - (R \sin\theta + h) \cdot \Delta\alpha}{\sin\theta} \quad (10)$$

From (10) and the first equation in (7) the x direction movement of point A_0 is also deduced.

When the damper motion is reconstructed from the measured quantities, the parallax error discussed in the last section is negligible, but there is another error factor: measurement uncertainty of laser projection position.

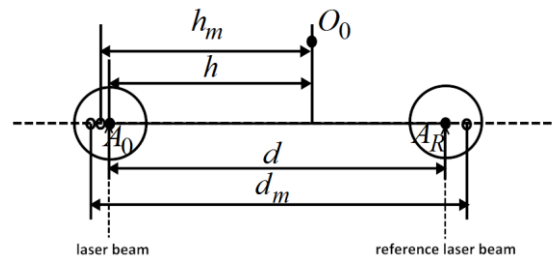


Fig 3.5 Laser beam projection position measurement uncertainty

As shown in Fig.3.5, the real distance between point A_0 and A_R is d , the corresponding measured distance is d_m and express their relation as $d = d_m \pm \sigma_d$; the real distance between point A_0 and O_0 is h , the corresponding measured distance is h_m and express their relation as $h = h_m \pm \sigma_h$. Denote the measurement of $\delta w_{A_0A_R}$ as δw for short. Maximally the circle area of laser spot on the damper bottom has a radius of $0.5mm$, from which reasonably σ_d is set to $\pm 1mm$ and σ_h is set to $\pm 0.5mm$.

From equation (9), (10) and the uncertainty propagation formulation used in the previous chapter, the measurement uncertainties of the rotation angle $\sigma_{\Delta\alpha}$ and the surface translation distance ds are deduced as following:

$$\sigma_{\Delta\alpha} = \sqrt{\left(\frac{\partial\Delta\alpha}{\partial d}\sigma_d\right)^2} = \frac{\delta w_m}{d_m^2}\sigma_d \quad (11-1)$$

$$\Delta\alpha = \Delta\alpha_m + \sigma_{\Delta\alpha} = \Delta\alpha_m \left(1 + \frac{\sigma_d}{d_m}\right) \quad (11-2)$$

$$\begin{aligned} \sigma_{ds} &= \sqrt{\left(\frac{\partial ds}{\partial h}\sigma_h\right)^2 + \left(\frac{\partial ds}{\partial\Delta\alpha}\sigma_{\Delta\alpha}\right)^2} = \sqrt{(\Delta\alpha_m\sigma_h)^2 + (h_m\sigma_{\Delta\alpha})^2} \\ &= \frac{1}{\sin\theta} \sqrt{(\Delta\alpha_m\sigma_h)^2 + \left(\frac{(R\sin\theta+h_m)\sigma_d}{d_m}\delta w_m\right)^2} \end{aligned} \quad (12)$$

Notice that $\sigma_{\Delta\alpha}$ is not dependent on the measured movement quantities, while σ_{ds} depends on measured quantities $\Delta\alpha_m$ and δw_m .

For example if $d_m = 10mm$, $h_m = 6mm$, the relative uncertainty of $\Delta\alpha$ is $\pm 10\%$; Besides if $\delta w_m = 30\mu m$ and $\Delta\alpha_m = 3 \times 10^{-3}$, the absolute uncertainty of ds is $4.6\mu m$.

3.3 Force measurement error from static indeterminacy

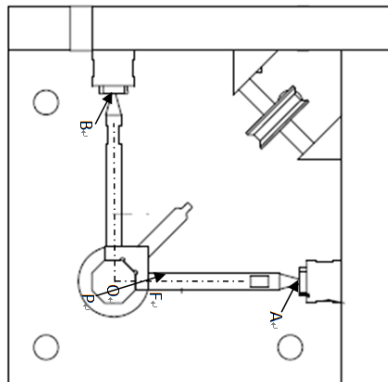


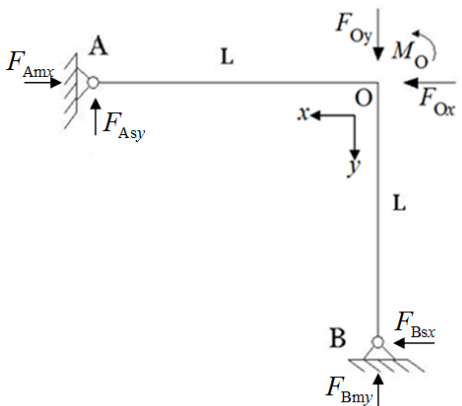
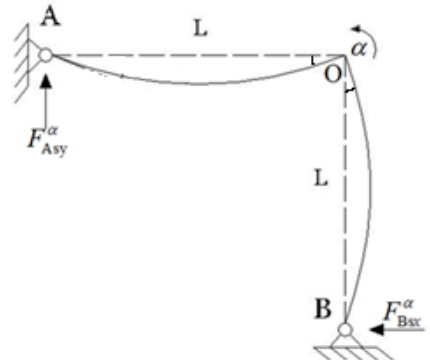
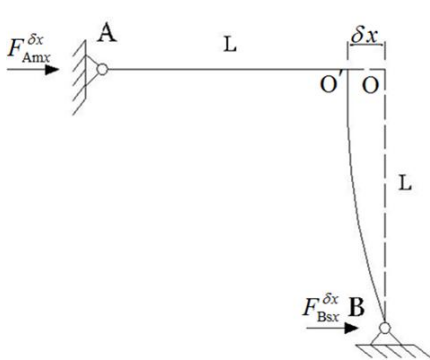
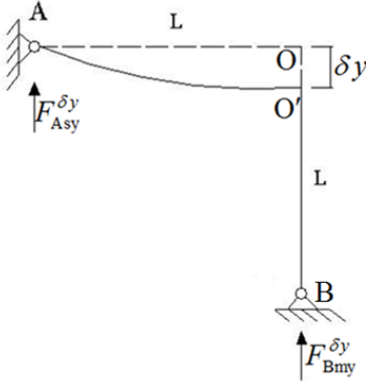
Fig.3.6 Sketch of the reaction force measurement structure

From Fig.3.6, the resultant force on the interface between damper and regular octagon shaped platform may not pass through the center of the platform. In this case, the force produces a momentum to the measurement mechanism.

In the structure, contact region A is the interface between horizontal rod end and support slot; contact region B is the interface between vertical rod end and support cave. In the real operation, a certain amount of preload is applied to the mechanism to prevent the slip at the contact region, so A and B can be regarded as two hinges. As we know, there are 3 equilibrium equations of the mechanism considering only x-y plane and there are 4 constraints from the two hinges. So the mechanism is not statically determined.

Due to the indeterminacy of the mechanism, it is necessary to make an analysis of the measured forces at contact region A and B caused by the interface resultant force. To make a feasible estimation, the cantilever beam model is adopted to simulate the two rods. Point O is the clamped end but movable, points A and B are the ends where reaction forces which play the role of external forces.

Fig.3.7.1 is the sketch of force distribution of the statically indeterminate mechanism. To calculate the reaction forces, three degrees of freedom at the cross point O is considered separately. Fig.3.7.2 represents the system when there is only angular displacement α . Fig.3.7.3 represents the system when there is only displacement δx . Fig.3.7.4 represents the system when there is only displacement δy . The reaction forces caused by known deformation under these three cases are listed below each figure.

 <p style="text-align: center;">Fig.3.7.1</p>	 <p style="text-align: center;">Fig.3.7.2</p>
$F_{Amx} - F_{Bsx} = F_{Ox}, \quad F_{Bmy} + F_{Asy} = F_{Oy}$ $F_{Asy} \cdot L + F_{Bsx} \cdot L = M_O$	$F_{Asy}^{\alpha} = \frac{3EI}{L^3} \cdot \alpha L = \frac{3EI}{L^2} \cdot \alpha$ $F_{Bsx}^{\alpha} = \frac{3EI}{L^3} \cdot \alpha L = \frac{3EI}{L^2} \cdot \alpha$
 <p style="text-align: center;">Fig.3.7.3</p>	 <p style="text-align: center;">Fig.3.7.4</p>
$F_{Amx}^{\delta x} = \frac{EA}{L} \cdot \delta x, \quad F_{Bsx}^{\delta x} = \frac{3EI}{L^3} \cdot \delta x$	$F_{Bmy}^{\delta y} = \frac{EA}{L} \cdot \delta y, \quad F_{Asy}^{\delta y} = \frac{3EI}{L^3} \cdot \delta y$

Using the equilibrium equations listed below Fig.3.6.1 and reaction force components shown in Fig.3.6.2-4, the following set of equations is constructed.

$$\left\{ \begin{array}{l} F_{Amx}^{\delta x} + F_{Bsx}^{\delta x} - F_{Bsx}^{\alpha} = F_{Ox} \\ F_{Bmy}^{\delta y} + F_{Asy}^{\delta y} + F_{Asy}^{\alpha} = F_{Oy} \\ F_{Asy}^{\delta y} \cdot L - F_{Bsx}^{\delta x} \cdot L + F_{Asy}^{\alpha} \cdot L + F_{Bsx}^{\alpha} \cdot L = M_O \end{array} \right.$$

Substituting the value of each reaction force component into the equations above, we obtain the following set of equations.

$$\left\{ \begin{array}{l} \frac{EA}{L} \cdot \delta x + \frac{3EI}{L^3} \cdot \delta x - \frac{3EI}{L^2} \cdot \alpha = F_{Ox} \\ \frac{EA}{L} \cdot \delta y + \frac{3EI}{L^3} \cdot \delta y + \frac{3EI}{L^2} \cdot \alpha = F_{Oy} \\ \frac{3EI}{L^2} \cdot \delta y - \frac{3EI}{L^2} \cdot \delta x + \frac{3EI}{L} \cdot \alpha + \frac{3EI}{L} \cdot \alpha = M_O \end{array} \right. \quad (13)$$

Denote a and b are the arms to the octagon center of force component F_{Ox} and F_{Oy} . The sign of the moment is positive when the moment is counterclockwise.

So the momentum is $M_O = F_{Ox} \cdot a - F_{Oy} \cdot b$.

Solving equations (13), the dimensionless displacement of each freedom is obtained.

$$\frac{\delta x}{L} = \frac{1}{2} \left[\left(\frac{1}{1+\gamma} + 1 \right) \cdot (\beta F_{Ox}) + \left(\frac{1}{1+\gamma} - 1 \right) \cdot (\beta F_{Oy}) + \left(\frac{a}{L} \right) \cdot (\beta F_{Ox}) - \left(\frac{b}{L} \right) \cdot (\beta F_{Oy}) \right] \quad (14)$$

$$\frac{\delta y}{L} = \frac{1}{2} \left[\left(\frac{1}{1+\gamma} - 1 \right) \cdot (\beta F_{Ox}) + \left(\frac{1}{1+\gamma} + 1 \right) \cdot (\beta F_{Oy}) - \left(\frac{a}{L} \right) \cdot (\beta F_{Ox}) + \left(\frac{b}{L} \right) \cdot (\beta F_{Oy}) \right] \quad (15)$$

$$\alpha = \frac{\beta F_{Ox} - \beta F_{Oy}}{2} + \frac{1}{2} \left(1 + \frac{1}{\gamma} \right) \left(\frac{a}{L} \cdot \beta F_{Ox} - \frac{b}{L} \cdot \beta F_{Oy} \right) \quad (16)$$

The coefficient $\beta = \frac{1}{EA}$ and $\gamma = \frac{3I}{AL^2}$. β represents the strain produced by one Newton's compression. γ represents a dimensionless quantity related to the geometry property of the rod. If the finite element procedure is applied, the same results can be obtained and additionally other unknown displacements are calculated.

$$\alpha_B = \frac{1}{2} \left(\frac{3}{2(1+\gamma)} + 1 \right) \cdot \beta F_{Ox} + \frac{1}{2} \left(\frac{3}{2(1+\gamma)} - 1 \right) \cdot \beta F_{Oy} + \frac{1}{2} \left(1 - \frac{1}{2\gamma} \right) \cdot \left(\frac{\beta M_O}{L} \right)$$

$$\alpha_A = -\frac{1}{2} \left(\frac{3}{2(1+\gamma)} - 1 \right) \cdot \beta F_{Ox} - \frac{1}{2} \left(\frac{3}{2(1+\gamma)} + 1 \right) \cdot \beta F_{Oy} + \frac{1}{2} \left(1 - \frac{1}{2\gamma} \right) \cdot \left(\frac{\beta M_O}{L} \right)$$

Then the reaction forces at the two hinges are obtained:

$$F_{Amx} = \frac{\delta x}{\beta L} = \frac{1}{2} \left(\frac{1}{1+\gamma} + 1 \right) \cdot F_{Ox} + \frac{1}{2} \left(\frac{1}{1+\gamma} - 1 \right) \cdot F_{Oy} + \frac{1}{2} \cdot \frac{a}{L} \cdot F_{Ox} - \frac{1}{2} \cdot \frac{b}{L} \cdot F_{Oy}$$

$$F_{Asy} = \frac{1}{2} \left[\left(1 - \frac{1}{1+\gamma} \right) \cdot F_{Ox} + \left(1 - \frac{1}{1+\gamma} \right) \cdot F_{Oy} + \frac{M_O}{L} \right]$$

$$F_{Bmy} = \frac{\delta y}{\beta L} = \frac{1}{2} \left(\frac{1}{1+\gamma} + 1 \right) \cdot F_{Oy} + \frac{1}{2} \left(\frac{1}{1+\gamma} - 1 \right) \cdot F_{Ox} - \frac{1}{2} \cdot \frac{a}{L} \cdot F_{Ox} + \frac{1}{2} \cdot \frac{b}{L} \cdot F_{Oy}$$

$$F_{Bsx} = \frac{1}{2} \left[\left(1 - \frac{1}{1+\gamma} \right) \cdot F_{Ox} + \left(1 - \frac{1}{1+\gamma} \right) \cdot F_{Oy} - \frac{M_O}{L} \right]$$

Consider the real geometry of the right platform shown in Fig.3.8. a and b are the arm lengths to the octagon center of contact force component F_{Ox} and F_{Oy} .

The momentum applied to the center is: $M_O = F_{Ox} \cdot a - F_{Oy} \cdot b$

Note that the sign of the moment is positive when the moment is counterclockwise.

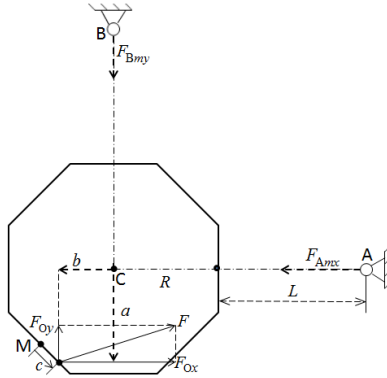


Fig.3.8 Demonstration of resultant force application position

The expression of measured and secondary forces at the joints now are expressed in matrix form:

$$\begin{Bmatrix} F_{Amx} \\ F_{Bmy} \end{Bmatrix} = \begin{bmatrix} \frac{1}{2} \left(\frac{1}{1+\gamma} + 1 + \frac{a}{L} \right) & \frac{1}{2} \left(\frac{1}{1+\gamma} - 1 - \frac{b}{L} \right) \\ \frac{1}{2} \left(\frac{1}{1+\gamma} - 1 - \frac{a}{L} \right) & \frac{1}{2} \left(\frac{1}{1+\gamma} + 1 + \frac{b}{L} \right) \end{bmatrix} \begin{Bmatrix} F_{Ox} \\ F_{Oy} \end{Bmatrix} \quad (17)$$

$$\begin{Bmatrix} F_{Bsx} \\ F_{Asy} \end{Bmatrix} = \begin{bmatrix} \frac{1}{2} \left(-\frac{1}{1+\gamma} + 1 - \lambda_1 \right) & \frac{1}{2} \left(-\frac{1}{1+\gamma} + 1 + \lambda_2 \right) \\ \frac{1}{2} \left(-\frac{1}{1+\gamma} + 1 + \lambda_1 \right) & \frac{1}{2} \left(-\frac{1}{1+\gamma} + 1 - \lambda_2 \right) \end{bmatrix} \begin{Bmatrix} F_{Ox} \\ F_{Oy} \end{Bmatrix} \quad (18)$$

Or inversely,

$$\begin{Bmatrix} F_{Ox} \\ F_{Oy} \end{Bmatrix} = \begin{bmatrix} \frac{(1+\gamma) \cdot (\alpha_2 + 1) + 1}{\alpha_1 + \alpha_2 + 2} & \frac{(1+\gamma) \cdot (\alpha_2 + 1) - 1}{\alpha_1 + \alpha_2 + 2} \\ \frac{(1+\gamma) \cdot (\alpha_1 + 1) - 1}{\alpha_1 + \alpha_2 + 2} & \frac{(1+\gamma) \cdot (\alpha_1 + 1) + 1}{\alpha_1 + \alpha_2 + 2} \end{bmatrix} \begin{Bmatrix} F_{Amx} \\ F_{Bmy} \end{Bmatrix} \quad (19)$$

In which, $\alpha_1 = \frac{a}{L}$ and $\alpha_2 = \frac{b}{L}$.

The approximated sizes of the beam model are following: $r=3.5\text{mm}$ (radius of the cross section), $L = 72.75\text{mm}$ (length of the rod). E is 210Gpa . For a circular cross section rod, $I=\pi r^4/4$.

According to these data, $\gamma = 1.7 \times 10^{-3}$ and $\beta = 1.24 \times 10^{-7}$.

The error caused by parasitic effect(represented by term $\frac{1}{1+\gamma}$) due to axial force is negligible compared to the influence(represented by $\frac{a}{L}$ or $\frac{b}{L}$) due to applied momentum.

After the damper is located between the platform, using real position of the contact point the corrections are made for each damper.

Three-point damper:

$$\begin{Bmatrix} F_{Ox} \\ F_{Oy} \end{Bmatrix} = \begin{bmatrix} 0.959 & 0.053 \\ 0.041 & 0.947 \end{bmatrix} \begin{Bmatrix} F_{Amx} \\ F_{Bmy} \end{Bmatrix}$$

Crossed curve-flat damper:

$$\begin{Bmatrix} F_{Ox} \\ F_{Oy} \end{Bmatrix} = \begin{bmatrix} 0.949 & 0.079 \\ 0.053 & 0.923 \end{bmatrix} \begin{Bmatrix} F_{Amx} \\ F_{Bmy} \end{Bmatrix}$$

Non-crossed curve flat damper:

$$\begin{Bmatrix} F_{Ox} \\ F_{Oy} \end{Bmatrix} = \begin{bmatrix} 0.961 & 0.056 \\ 0.041 & 0.946 \end{bmatrix} \begin{Bmatrix} F_{Amx} \\ F_{Bmy} \end{Bmatrix}$$

3.4 Conclusions

When the differential laser is used to measure a single point movement on one translational and relative movement for two translational bodies, the error due to a small inclination between the operation direction and ideal direction can be negligible.

When the differential laser is used to measure a single point movement on one motive body with rotation, the parallax error is negligible when the motion amplitude is small(less than $100 \mu\text{m}$ range). The measurement of rotation of a rigid body by the differential laser has an maximal 10% error due to measurement uncertainty of the distance between two projected distance.

The force error caused by the mechanism indeterminacy is corrected by a simplified beam model.

The total error of force measurement can be considered from the nonlinearity deviation of sensitivity which is 5% given in chapter 1.

Equation (16) can be used to estimate the rotation angle due to applied momentum, a better design of the platform can reduce this effect.

Chapter 4 Experimental results

After the test rig is set up and measurement error analysis, measurements are taken to investigate damper behavior. Elaborations are made to show the damping characteristics, motion and equilibrium due to contact forces of the damper.

4.1 Stiffness from measured hysteresis

As mentioned in the previous chapter, the hysteresis between the measured force and relative movement of the corresponding platforms reflect the damping which happen on the dual interface. This hysteresis, not like the single contact interface hysteresis, does not give direct information on contact tangential stiffness, but gives information combining both normal and tangential stiffness of the two interfaces. Fig.4.1 shows a typical spherical-flat surface hysteresis under tangential relative movement, in which $K_{\text{tangential}}$ represents the tangential contact stiffness of this contact pair.

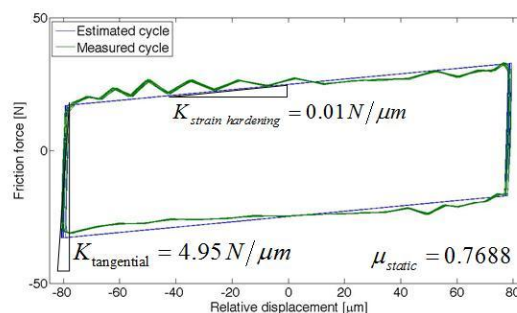


Fig.4.1 Typical spherical-flat hysteresis under tangential loading(from LAQ.AERMEC at Politecnico di Torino)

Consider the case of out-of-phase motion (shown in Fig.4.2), where the relative movement between the two platform is only horizontal (along x direction). Assume the right platform is static and the relative movement is given by the left platform displacement u_L . Under the motion of left platform, the damper experiences a horizontal and vertical displacement as u_D and w_D . Denote the contact point on the left platform as L_P , the coupled contact point on the damper as L_D . Denote the contact point on the right platform as R_P , the coupled contact point on the damper as R_D . After the motion, the contact points move to L'_P , L'_D , R'_P and R'_D respectively.

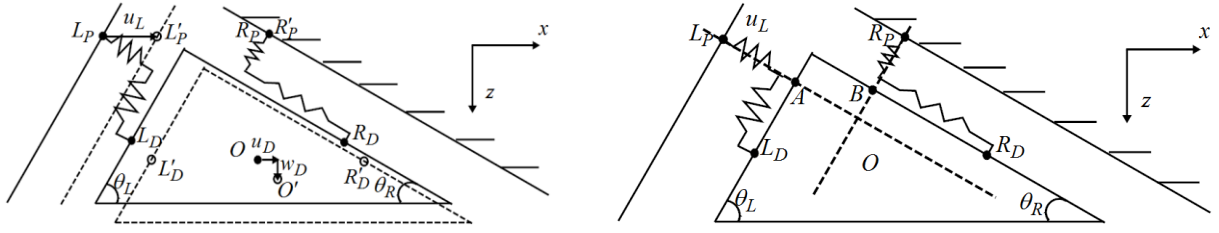


Fig.4.2 Contact spring loading under out-of-phase condition

A and B are the auxiliary points to determine the spring lengths. First find the coordinates of the auxiliary points. Take A for example. Line $\overline{AL_P}$ is perpendicular to line $\overline{AL_D}$, implying:

$$(x_A - x_{L_P})(x_A - x_{L_D}) + (z_A - z_{L_P})(z_A - z_{L_D}) = 0$$

Additionally, the slope of line $\overline{AL_D}$ is $\tan(\theta_L)$, implying:

$$z_A = -\tan(\theta_L)(x_A - x_{L_D}) + z_{L_D}$$

Combining the two relations, x_A and z_A are obtained:

$$x_A = \frac{x_{L_P} + \tan^2(\theta_L)x_{L_D} + \tan(\theta_L)(z_{L_D} - z_{L_P})}{1 + \tan^2(\theta_L)}$$

$$z_A = \frac{z_{L_D} + \tan^2(\theta_L)z_{L_P} + \tan(\theta_L)(x_{L_D} - x_{L_P})}{1 + \tan^2(\theta_L)}$$

Denote $\tan(\theta_L)$ as T_1 , $\sin(\theta_L)$ as S_1 and $\cos(\theta_L)$ as C_1 . The spring lengths on the left interface are obtained:

$$s_L^n = \frac{x_A - x_{L_P}}{\sin(\theta_L)} = \frac{T_1^2(x_{L_D} - x_{L_P}) + T_1(z_{L_D} - z_{L_P})}{(1 + T_1^2)S_1}$$

$$s_L^t = \frac{x_A - x_{L_D}}{\cos(\theta_L)} = \frac{x_{L_P} - x_{L_D} + T_1(z_{L_D} - z_{L_P})}{(1 + T_1^2)C_1}$$

Similarly for the right contact interface, the following relations are expressed:

$$x_B = \frac{x_{R_P} + \tan^2(\theta_R)x_{R_D} - \tan(\theta_R)(z_{R_D} - z_{R_P})}{1 + \tan^2(\theta_R)}$$

$$z_B = \frac{z_{R_D} + \tan^2(\theta_R)z_{R_P} - \tan(\theta_R)(x_{R_D} - x_{R_P})}{1 + \tan^2(\theta_R)}$$

Denote $\tan(\theta_R)$ as T_2 , $\sin(\theta_R)$ as S_2 and $\cos(\theta_R)$ as C_2 . The spring lengths on the right interface are obtained:

$$s_R^n = \frac{x_{R_P} - x_B}{\sin(\theta_R)} = \frac{T_2^2(x_{R_P} - x_{R_D}) + T_2(z_{R_D} - z_{R_P})}{(1 + T_2^2)S_2}$$

$$s_R^t = \frac{x_{R_D} - x_B}{\cos(\theta_R)} = \frac{x_{R_D} - x_{R_P} + T_2(z_{R_D} - z_{R_P})}{(1 + T_2^2)C_2}$$

After the motion of the left platform, new lengths of the contact springs are:

$$s_{L'}^n = \frac{T_1^2(x_{L'_D} - x_{L'_P}) + T_1(z_{L'_D} - z_{L'_P})}{(1 + T_1^2)S_1}, s_{L'}^t = \frac{x_{L'_P} - x_{L'_D} + T_1(z_{L'_D} - z_{L'_P})}{(1 + T_1^2)C_1}$$

$$s_{R'}^n = \frac{T_2^2(x_{R'_D} - x_{R'_P}) + T_2(z_{R'_D} - z_{R'_P})}{(1 + T_2^2)S_2}, s_{R'}^t = \frac{x_{R'_D} - x_{R'_P} + T_2(z_{R'_D} - z_{R'_P})}{(1 + T_2^2)C_2}$$

And the relations between new and initial positions of contact points are:

$$\begin{aligned} x_{L'_p} - x_{L_p} &= u_L; \quad z_{L'_p} - z_{L_p} = 0; \quad x_{R'_p} - x_{R_p} = 0; \quad z_{R'_p} - z_{R_p} = 0 \\ x_{L'_D} - x_{L_D} &= u_D; \quad z_{L'_D} - z_{L_D} = w_D; \quad x_{R'_D} - x_{R_D} = u_D; \quad z_{R'_D} - z_{R_D} = w_D \end{aligned}$$

Then the incremental loading caused by the left platform motion is:

$$\delta F_L^n = -k_L^n (s_{L'}^n - s_L^n) = -k_L^n \frac{T_1^2 (u_D - u_L) + T_1 w_D}{(1+T_1^2) S_1} \quad (1)$$

$$\delta F_L^t = k_L^t (s_{L'}^t - s_L^t) = k_L^t \frac{u_L - u_D + T_1 w_D}{(1+T_1^2) C_1} \quad (2)$$

$$\delta F_R^n = -k_R^n (s_{R'}^n - s_R^n) = -k_R^n \frac{-T_2^2 u_D + T_2 w_D}{(1+T_2^2) S_2} \quad (3)$$

$$\delta F_R^t = k_R^t (s_{R'}^t - s_R^t) = k_R^t \frac{u_D + T_2 w_D}{(1+T_2^2) C_2} \quad (4)$$

For the sign definition in equation (1)-(4), the normal force increment is positive when it is increased, and the tangential force increment is positive when it is increased along the direction to the upper triangle vertex.

When neglecting the inertial force of the damper, the total incremental load on the damper is zero. This equilibrium condition is expressed in x and z direction:

$$\begin{cases} \delta F_L^n \cdot S_1 + \delta F_L^t \cdot C_1 - (\delta F_R^n \cdot S_2 + \delta F_R^t \cdot C_2) = 0 \\ \delta F_L^n \cdot C_1 - \delta F_L^t \cdot S_1 + \delta F_R^n \cdot C_2 - \delta F_R^t \cdot S_2 = 0 \end{cases} \quad (5)$$

Substitute (1)-(4) into (5), two equations containing u_D and w_D are obtained:

$$\begin{cases} a_1 u_D + b_1 w_D = c_1 u_L \\ a_2 u_D + b_2 w_D = c_2 u_L \end{cases} \rightarrow \begin{cases} u_D = \frac{b_2 c_1 - b_1 c_2}{a_1 b_2 - a_2 b_1} u_L \\ w_D = \frac{a_1 c_2 - a_2 c_1}{a_1 b_2 - a_2 b_1} u_L \end{cases} \quad (6)$$

$$\begin{aligned} \text{, in which } a_1 &= \frac{-k_L^n T_1^2 - k_L^t}{1+T_1^2} + \frac{-k_R^n T_2^2 - k_R^t}{1+T_2^2}, \quad b_1 = \frac{(-k_L^n + k_L^t) T_1}{1+T_1^2} + \frac{(k_R^n - k_R^t) T_2}{1+T_2^2}, \quad c_1 = \frac{-k_L^n T_1^2 - k_L^t}{1+T_1^2} \\ a_2 &= \frac{T_1 (k_L^t - k_L^n)}{1+T_1^2} + \frac{T_2 (k_R^n - k_R^t)}{1+T_2^2}, \quad b_2 = \frac{-(k_L^n + k_L^t T_1^2)}{1+T_1^2} + \frac{-(k_R^n + k_R^t T_2^2)}{1+T_2^2}, \quad c_2 = \frac{T_1 ((k_L^t - k_L^n))}{1+T_1^2} \end{aligned}$$

From (5) the horizontal contact force component is:

$$\begin{aligned} \delta F_h &= (\delta F_R^n \cdot S_2 + \delta F_R^t \cdot C_2) \\ &= \left[-a_{12} \frac{b_2 c_1 - b_1 c_2}{a_1 b_2 - a_2 b_1} - a_{22} \frac{a_1 c_2 - a_2 c_1}{a_1 b_2 - a_2 b_1} \right] u_L \end{aligned} \quad (7)$$

$$\text{, in which } a_{12} = \frac{-k_R^n T_2^2 - k_R^t}{1+T_2^2}, \quad a_{22} = \frac{T_2 (k_R^n - k_R^t)}{1+T_2^2}.$$

So the visual stiffness obtained from the horizontal hysteresis curve has a value as:

$$k_h = \frac{\delta F_h}{u_L} = \left[-a_{12} \frac{b_2 c_1 - b_1 c_2}{a_1 b_2 - a_2 b_1} - a_{22} \frac{a_1 c_2 - a_2 c_1}{a_1 b_2 - a_2 b_1} \right] \quad (8)$$

Although k_h is complicatedly coupled by the normal and tangential stiffness of the two interfaces, it is a constant determined by the single contact stiffness and damper geometry. The actual contact stiffness on the two interfaces have the same magnitude level as k_c .

When $k_L^n = k_R^n = k^n$, $k_L^t = k_R^t = k^t$, $T_1 = T_2 = 1$, from equation (8) it is found:

$$\frac{1}{k_h} = \frac{1}{k^n} + \frac{1}{k^t} \quad (9)$$

When $k_L^n = 2k_R^n = 2k^n$, $k_L^t = 2k_R^t = 2k^t$, $T_1 = T_2 = 1$, it is found:

$$k_h = \frac{3k^n k^t (k^n + k^t)}{(k^n + 2k^t)(k^t + 2k^n)} \quad (10)$$

When $k^n = \frac{3}{2} k^t$, referred to [27], there is

$$k_h = \frac{45}{56} k^t \quad (11)$$

Fig.4.3.1-4.3.4 are typical hysteresis obtained from independent experiments under the same condition above.

Here the equivalent stiffness of k_v is not formulated, the analysis procedure is similar and normally $k_v \neq k_h$.

4.2 Out-of-phase results of three-point damper

4.2.1 Hysteresis characteristics

motion type	nominal amplitude	excitation frequency	dead weight
Out-of-phase	60 μ m	10Hz	4.65kg

Take the above condition as a start case.

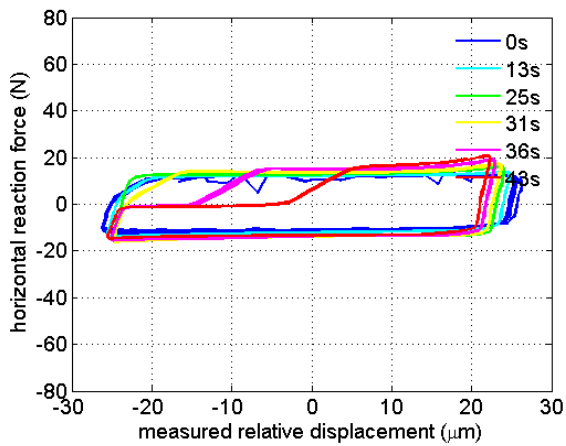


Fig.4.3.1

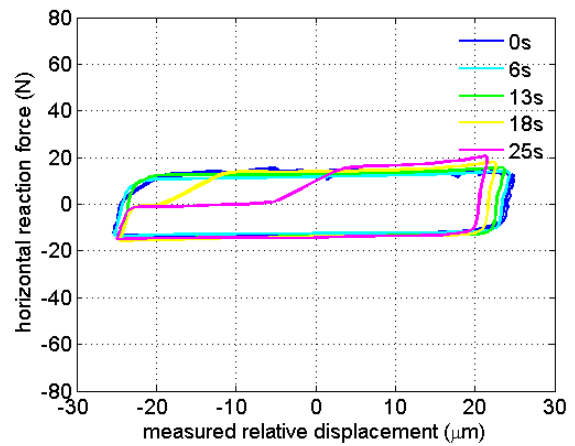


Fig.4.3.2

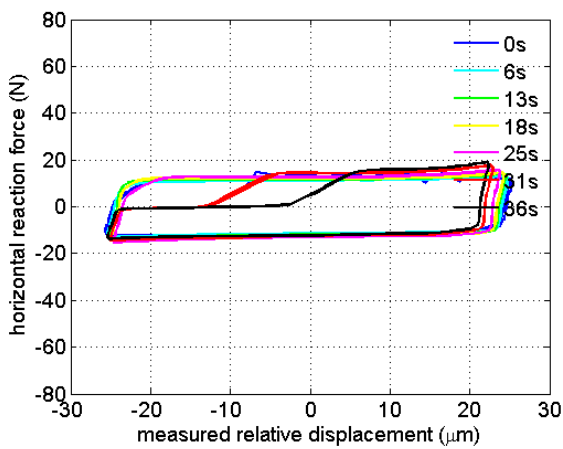


Fig.4.3.3

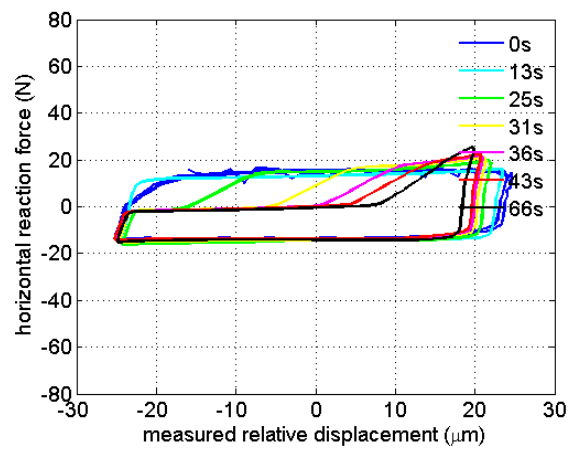


Fig.4.3.4

Fig.4.3.1-4.3.4 are typical hysteresis obtained from independent experiments under the same condition above. By independent it means at the beginning of each test the damper is released to avoid initial condition set from the end of previous test .

- (1) In the beginning the hysteresis has a shape similar to single contact interface hysteresis (stick-slip) which contains both macro-slip and micro-slip phenomenon. There is a constant slope k_h as discussed in the section before.
- (2) With the time going, the hysteresis changes in the way that relative displacement amplitude reduces and reaction force amplitude increases. The proportion of the two quantities is constant.
- (3) A 'shoe' shape occurs after some time and this phenomenon is repeatable.

Details from Fig.4.3.1 and Fig.4.3.4 are shown in Fig.4.4.1 and Fig.4.4.2.

Here the equivalent stiffness of k_v is not formulated, the analysis procedure is similar and normally $k_v \neq k_h$.

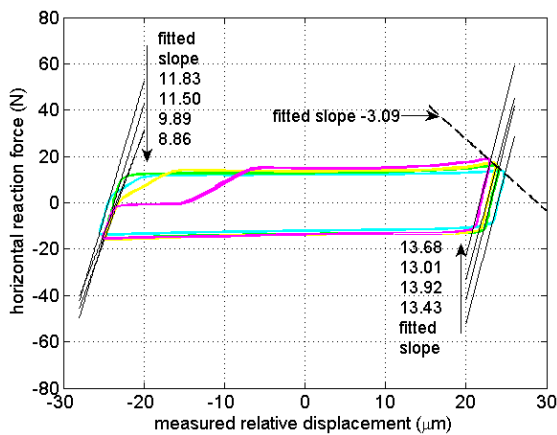


Fig.4.4.1

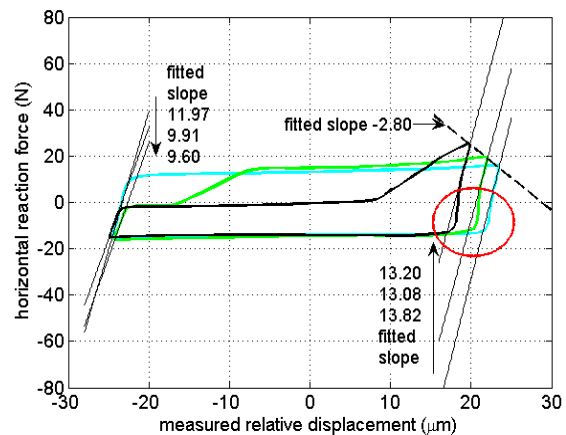


Fig.4.4.2

The explanation of fact (2) readily is obtained if we note that the series of the two springs in the test rig, $k_{hL} = 4.7 \pm 0.1N/\mu m$, $k_{hR} = 4.7 \pm 0.1N/\mu m$, implies a total horizontal spring value of the test rig itself at $3.05N/\mu m$.

From the test rig stiffness distribution, with the following symbols:

C_p : calibration factor of the piezoelectric stack actuator

$V(t)$: voltage applied to the actuator

$H(t)$: horizontal force through the damper

δ_{hL} : compliance of the left spring, including the stack own compliance, calculated at $1 / 4.7 = 0.213 \mu m/N$

δ_{hR} : compliance of the right spring, including the stack own compliance, calculated at $1 / 8.7 = 0.115 \mu m/N$

u_L : left platform horizontal displacement

u_R : right platform horizontal displacement

u_{LR} : horizontal relative platform displacement

, it is readily calculated that: $u_L = C_p V(t) - H(t)\delta_{hL}$, $u_R = H(t)\delta_{hR}$

$$u_{LR} = u_L - u_R = C_p V(t) - H(t)(\delta_{hL} + \delta_{hR})$$

When $V(t)$ reaches the maximum V_{max} , the relative displacement will reach the maximum u_{LR}^{max} accordingly, denote H^{max} as the force at this moment. For two different values of u_{LR}^{max} and H^{max} , the relation is expressed:

$$u_{LR}^{max1} - u_{LR}^{max2} = (H^{max2} - H^{max1})(\delta_{hL} + \delta_{hR}) \quad (12)$$

Fig.3.5 shows the plot of this formula. However, force sensors and laser and the acquisition system do not measure the total force H displacement u_{LR} , they give instead the values \tilde{H} and \tilde{u}_{LR} about the mean. When the diagram is symmetric, then the mean is in the symmetry center. Therefore in the case of a symmetric cycle the lower-left and the upper-right ends of the diagram will lie, in axes $(\tilde{H}, \tilde{u}_{LR})$. Although the measured hysteresis is not completely symmetric, the difference of different mean values is small. It is seen from the dashed line represented in Fig.4.4.1 and Fig.4.4.2, the slope which matches well with spring constant data obtained in the calibration stage.

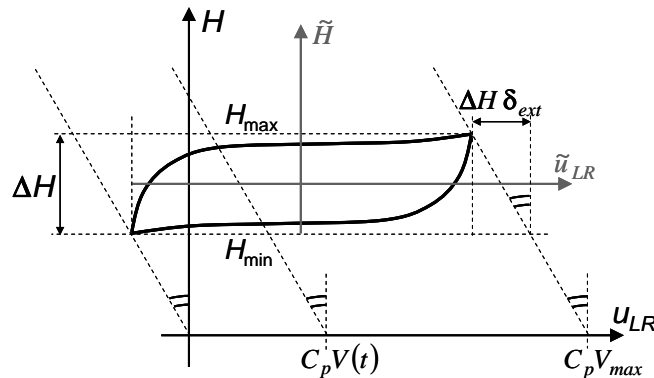


Fig.4.5 Plot of symmetric hysteresis diagram in "total" and in "about the mean" axes

The visual contact stiffness from Fig.4.4.1 and Fig.4.4.2 shows that there is some difference between the condition when the damper moves out and in. The shaped labeled by red ellipse in Fig.4.4.2 is not present in the single contact hysteresis with constant normal load.

Fig.4.6.1-Fig.4.6.6 show the different way of hysteresis evolution from three tests. Fig.4.6.1-4.6.2, Fig.4.6.3-4.6.4, and Fig.4.6.5-4.6.6 belong to one test respectively.

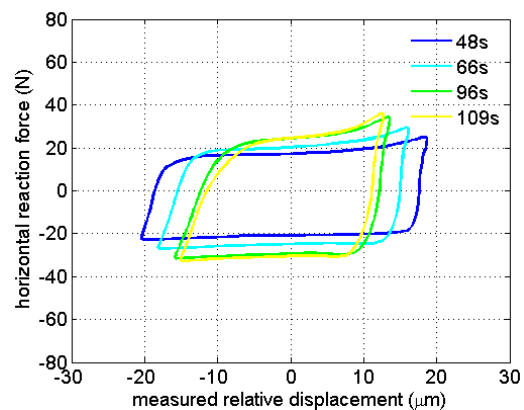
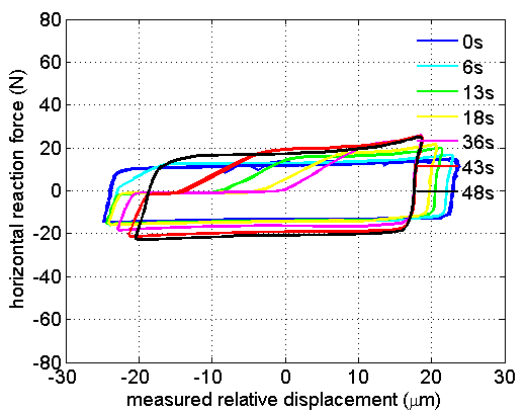


Fig.4.6.1

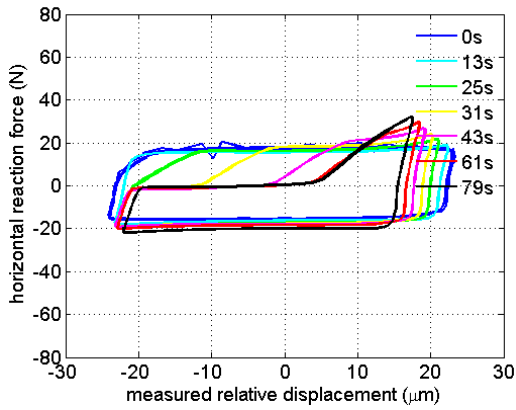


Fig.4.6.3

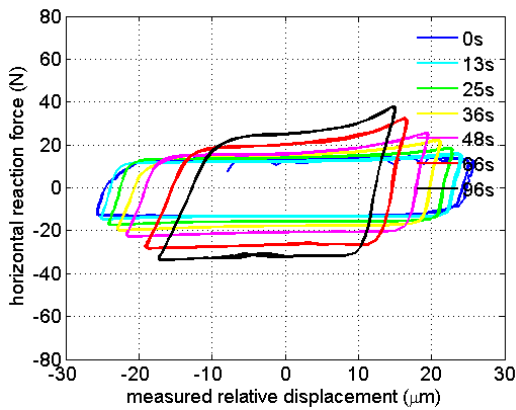


Fig.4.6.5

Fig.4.6.2

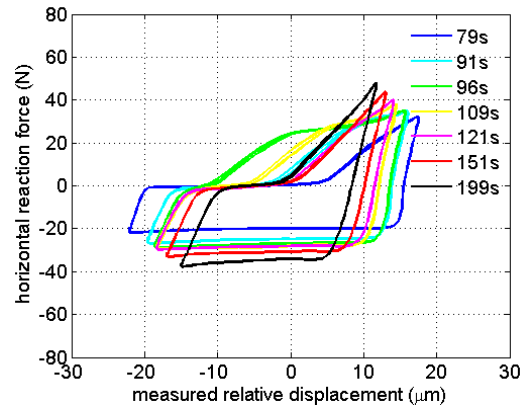


Fig.4.6.4

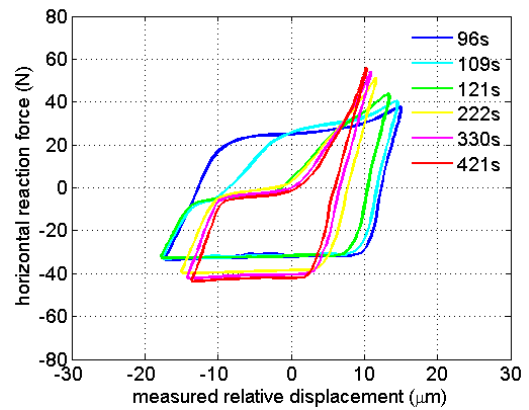


Fig.4.6.6

In the first group, the 'shoe' shape disappears after some time and keep a quasi Coulomb shape going on. In the second group, the 'shoe' shape maintains to the end. While in the third group, the 'shoe' shape happens after a relatively long period compared to the previous two. At this stage, it is difficult to explain the 'shoe' shape and the difference of evolution procedure. From phenomenological point of view, the evolution of transmitted force measurement are given as an observation reference. Fig.4.7.1-4.7.2, Fig.4.7.3-4.7.4, Fig.4.7.5-4.7.6 correspond to the case of Fig.4.6.1-4.6.2, Fig.4.6.3-4.6.4, and Fig.4.6.5-4.6.6 respectively and the colors follow the same arrangement. The solid line represent the horizontal force and the dashed line represent the vertical force.

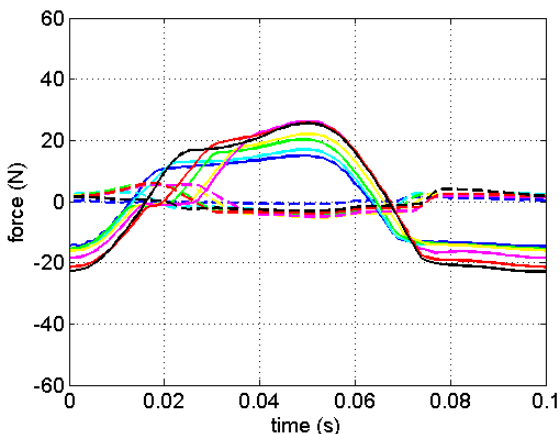


Fig.4.7.1

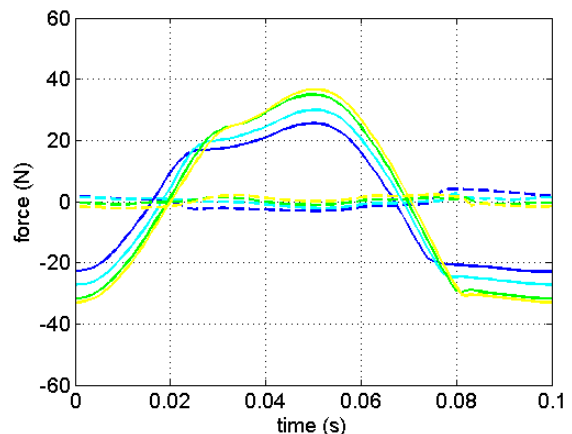


Fig.4.7.2

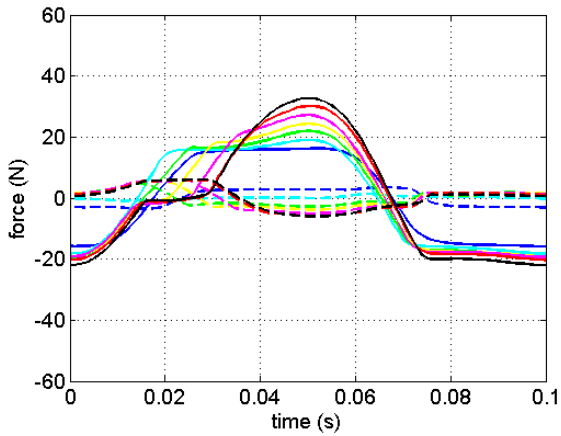


Fig.4.7.3

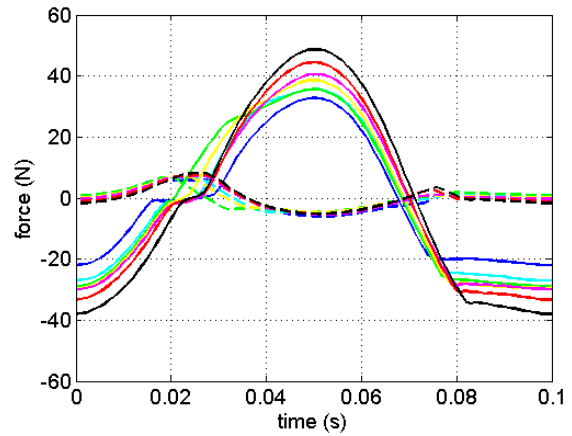


Fig.4.7.4

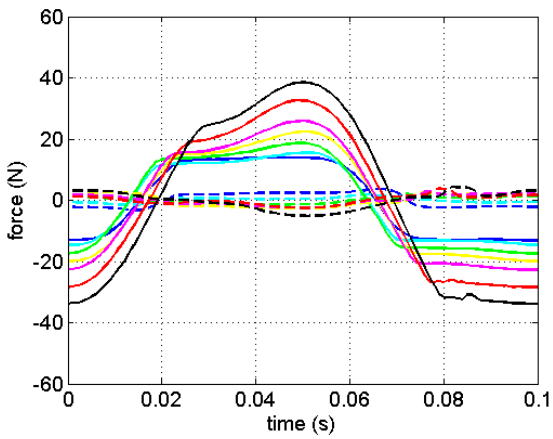


Fig.4.7.5

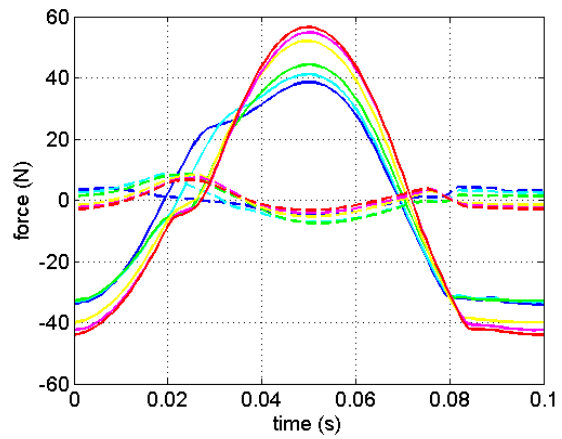


Fig.4.7.6

It is clear that both quasi-Coulomb shape and ‘shoe’ shape can happen under different contact force level. The increase of contact force can be due to the increase of traditionally defined parameter: friction coefficient by gradual moving in between the two platforms.

4.2.2 Influence of excitation frequency

Test conditions are listed below:

motion type	nominal amplitude	excitation frequency	dead weight
out-of-phase	60 μ m	5Hz (Fig.3.8.1-Fig.3.8.2) 40Hz(Fig.3.8.3-Fig.3.8.4) 80Hz(Fig.3.8.5-Fig.3.8.6)	2.65kg

Hysteresis are shown in Fig.4.8.1-Fig.4.8.6:

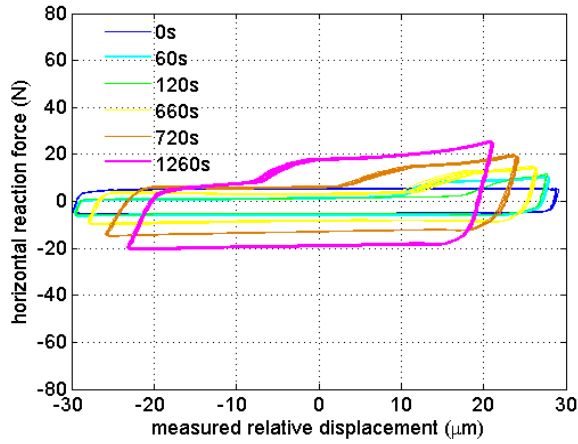


Fig.4.8.1

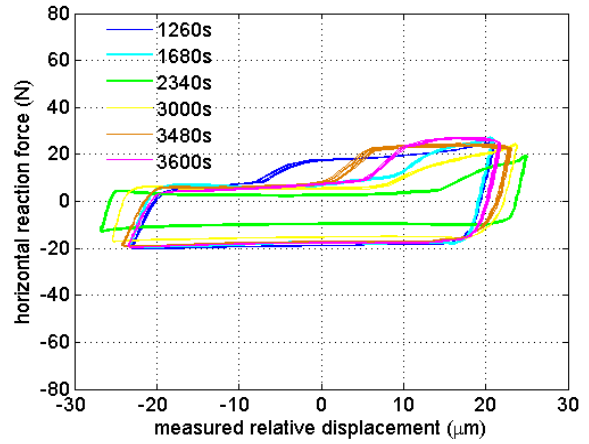


Fig.4.8.2

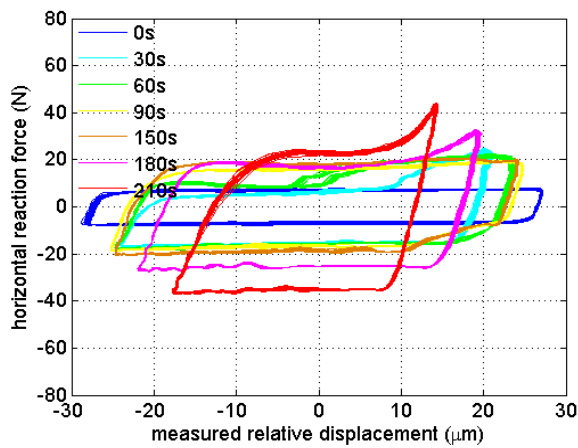


Fig.4.8.3

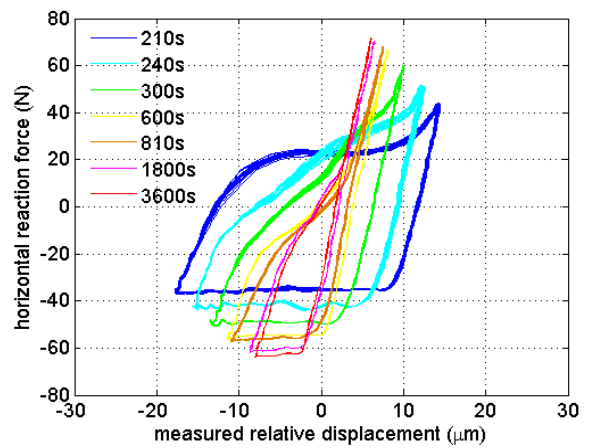


Fig.4.8.4

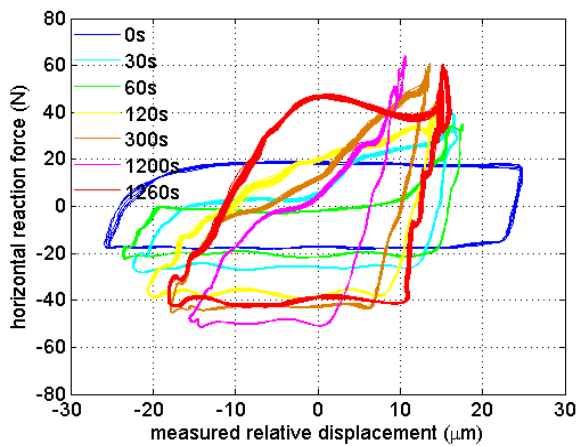


Fig.4.8.5

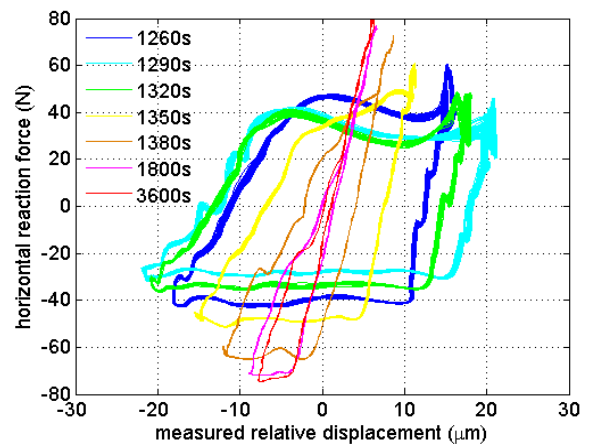


Fig.4.8.6

Comparing the hysteresis in last section and this section, it can be summarized that under low frequency(5Hz, 10Hz respectively) the hysteresis is more precise representing the interface property due to less influence of higher frequency component in the signal. At this moment we are not sure whether the high frequency component is linked to the damper or interface or the test rig structure.

The area of the hysteresis represents the total energy dissipated by the damper through the contact interfaces with the two platforms. Fig.4.9 shows this feature along with time.

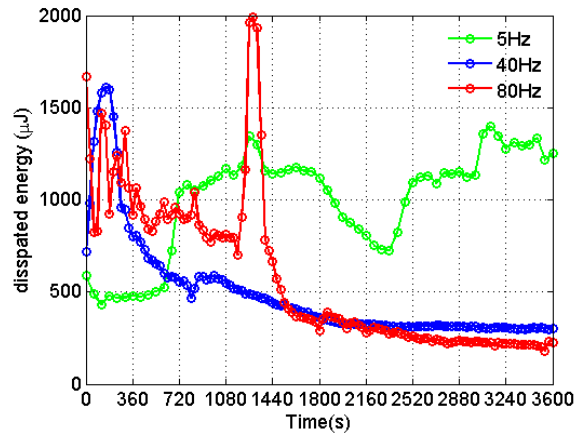


Fig.4.9 Energy dissipation from the hysteresis

Under high frequency, the transmitted force through the damper increases significantly within the test duration and the corresponding hysteresis gets into a micro-slip pattern, which consumes much less energy than the macro-slip scheme.

Lower preload (dead weight 2.65kg) tends to increase the uncertainty of damper response, which can be interpreted as a consequence of contact parameters sensitivity.

4.2.3 Contact force distribution

To understand better the behavior of damper in operation, it is useful to explore the force distribution on the damper surfaces. As mentioned in Chapter 2, by neglecting the damper inertial force, the contact forces and simulated centrifugal force by deadweight preload are in equilibrium. And the absolute contact forces are obtained from deadweight lifting with certain error acceptable. Fig.4.10 is typical load removal result in the test.

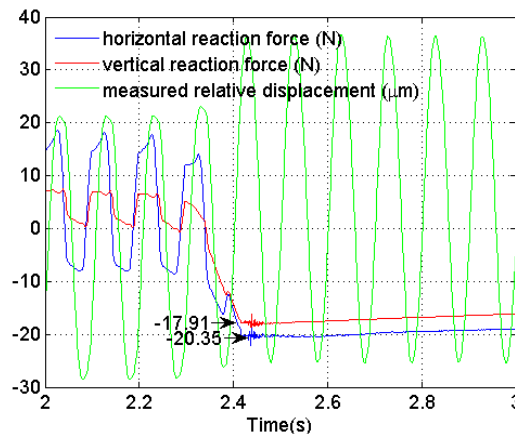


Fig.4.10

After knowing the real contact force (dynamic plus static part), damper equilibrium is constructed through the principle that contact force on the right surface, left surface and centrifugal force pass through one point.

Fig.4.11.1-Fig.4.11.3, Fig.4.12.1-Fig.4.12.3, Fig.4.13.1-Fig.4.13.3, and Fig.4.14.1-Fig.4.14.3 are the results grouped (a,b,c,d) corresponding to each hysteresis shape obtained from section 4.1.1. The first diagram is the hysteresis, the second shows the proportion between tangential force (TF) and normal force (NF) on each surface and the third shows contact force distribution.

In group a, the hysteresis is similar to Coulomb cycle. The features are summarized:

- (1). From green to pink to green point, both interfaces are in stick state.
- (2). From pink to cyan point, the left interface is in stick state and the right interface is in positive slip state.
- (3). From cyan to red point, both interfaces are in slip state with some strain hardening effect.
- (4). From red to yellow point, both interfaces are in stick state.
- (5). From yellow to black point, the left interface is in stick state and the right interface is in micro-slip state.
- (6). From black to green point, both interfaces are in slip state.
- (7). The resultant force on left side passes through the center of surface, which means that both curved surfaces on left side are in contact with left platform.

Here experimentally it is verified that in the wedge shaped under-platform damper, each interface can have different states between stick and slip at the same time.

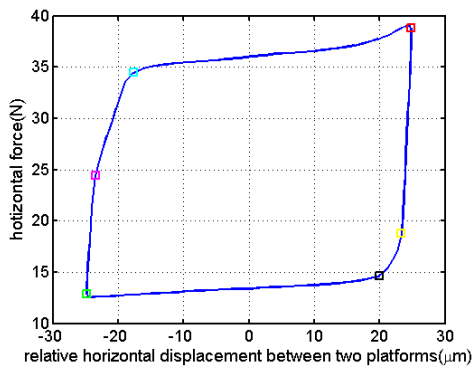


Fig.4.11.1(group a)

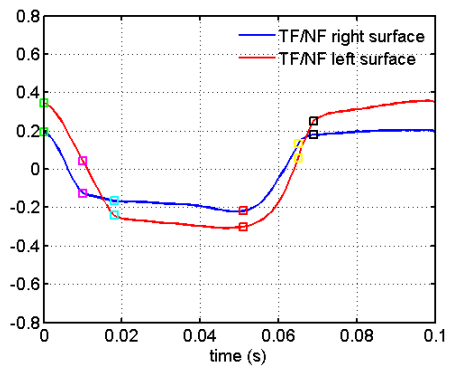


Fig.4.11.2(group a)

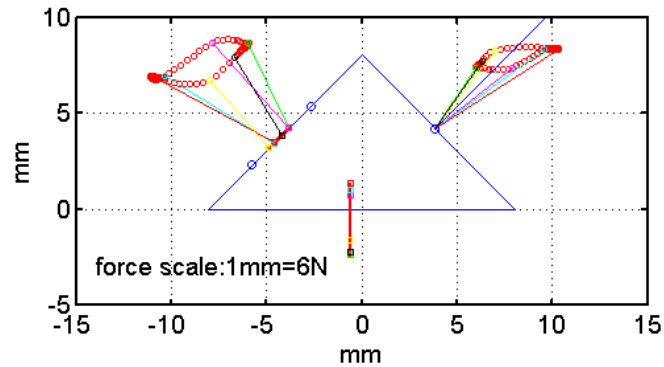


Fig.4.11.3(group a)

In group b, the largest difference from group a is in the part from pink to cyan point, where the left interface is in slip state reaching the friction limit while the right interface is in stick state but with a constant proportion between tangential and normal contact force, which happens normally when the interface reaches friction limit.

From the force distribution diagram Fig.4.12.3, the resultant force application position moves down to the lower contact point where the pink and blue point locate near to. If the errors of force measurement and the real position of contact are considered, this demonstration of distribution

features is satisfactory. At this moment, the assumption that between pink and blue stage, the upper contact point loses the contact.

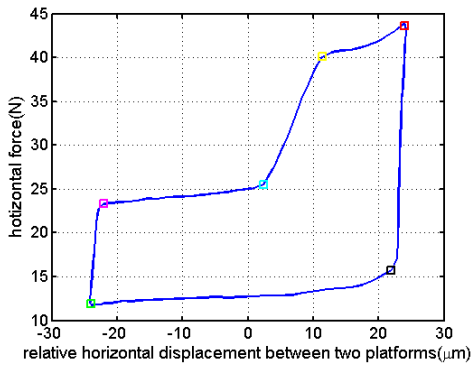


Fig.4.12.1(group b)

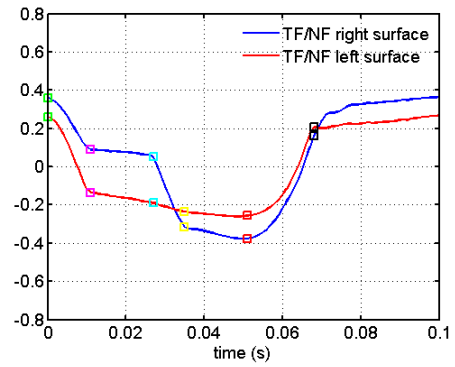


Fig.4.12.2(group b)

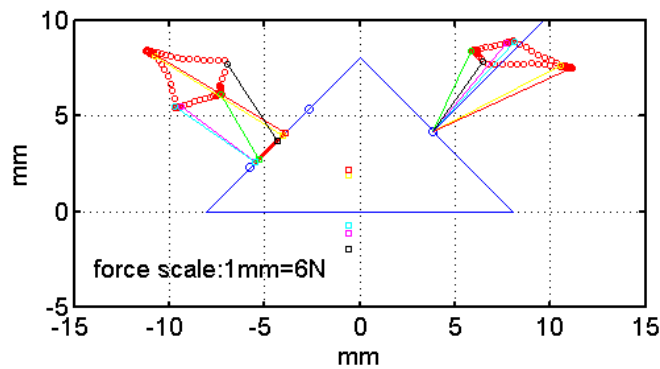


Fig.4.12.3(group b)

Group c is similar with group b except for the stage between cyan and yellow point. In this case, from Fig.4.13.2, the right surface does not slip when the two platforms move near.

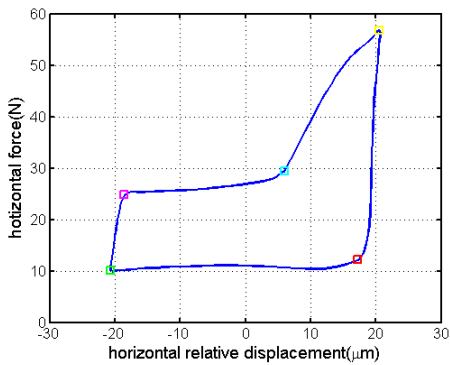


Fig.4.13.1(group c)

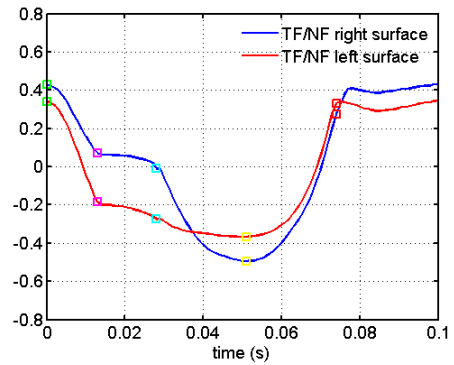


Fig.4.13.2(group c)

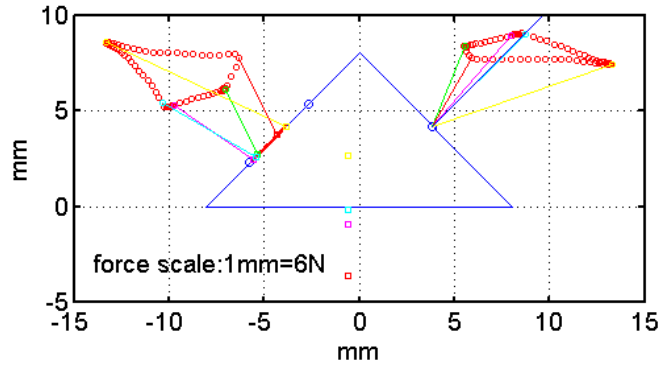


Fig.4.13.3(group c)

In group d, the resultant force on left surface passes near the center similar to group a and consequently no contact point loses contact. Fig.4.14.2 tells us that the nominal friction coefficient in this case reaches higher value. Here the results are not presented for all cases obtained from the experiment. By summarizing the results a conclusion can be made that force distribution influences and reflects the motion features of the damper and the friction coefficient is an important parameter which influences the equilibrium state of the amper.

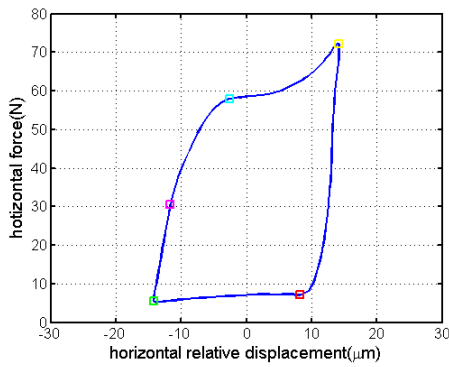


Fig.4.14.1(group d)

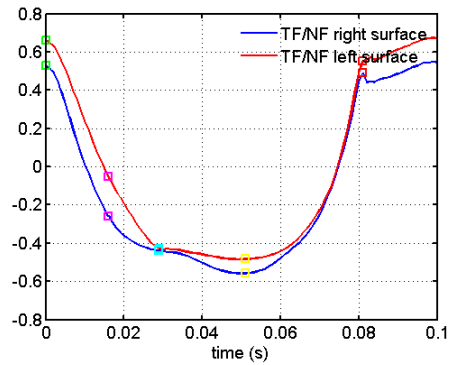


Fig.4.14.2(group d)

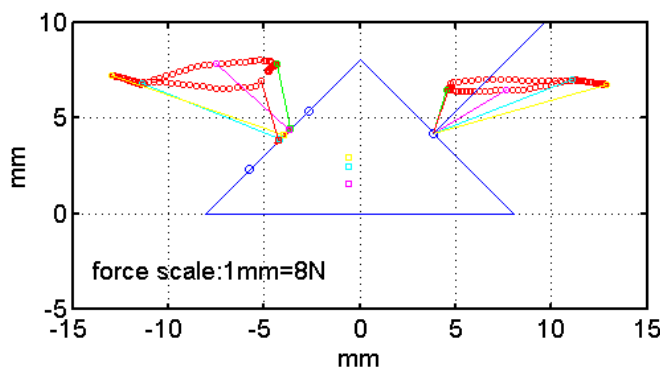


Fig.4.14.3(group d)

4.2.4 Rotation features

It is natural to investigate the complex hysteresis and force distribution patterns by observing the damper rotation which is neglected at the beginning when people considered this problem. There is a difficulty as mentioned before that we cannot measure damper rotation and relative

displacement between the two platforms at the same time from one differential laser, so the measured force is a reference signal to synthesize the results from different tests.

Fig.4.15-Fig.4.18 show the results according to the condition below.

motion type	nominal amplitude	excitation frequency	dead weight	laser beam distance
out-of-phase	$60\mu m$	5Hz (Fig.4.15-Fig.4.17) 40Hz(Fig.4.18)	4.65kg	$11.3\pm 0.1mm$

For Fig.4.15-Fig.4.17, sub diagram a and b are from one test while c and d are from the other independent test. Sub diagram b and d are the reference force signal, a shows the hysteresis, c shows damper rotation.

In Fig.4.15 the hysteresis corresponds to a quasi Coulomb shape and the damper rotation is negligible small(relative displacement between the measured two points is less than $1\mu m$). In Fig.4.16 the hysteresis begins changing to a 'shoe' shape and the damper rotation peak to peak amplitude is increased about 4 times. The hysteresis in Fig.4.17 is a 'shoe' shape with high contact force and the damper rotation amplitude increases about 20 times than in the case demonstrated by Fig.4.15.

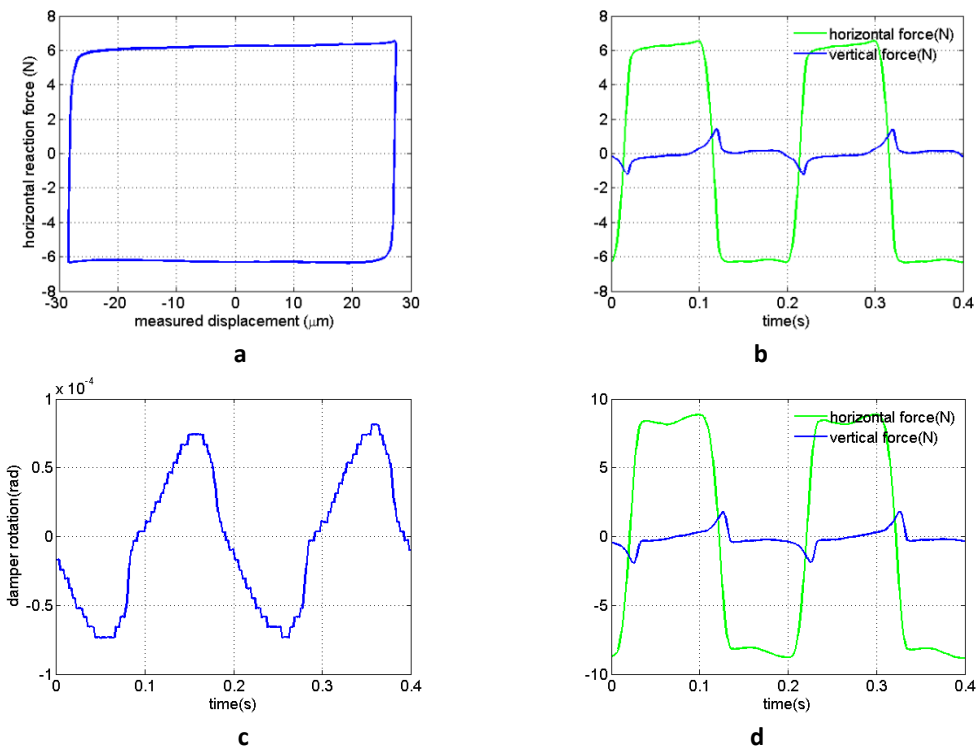


Fig.4.15

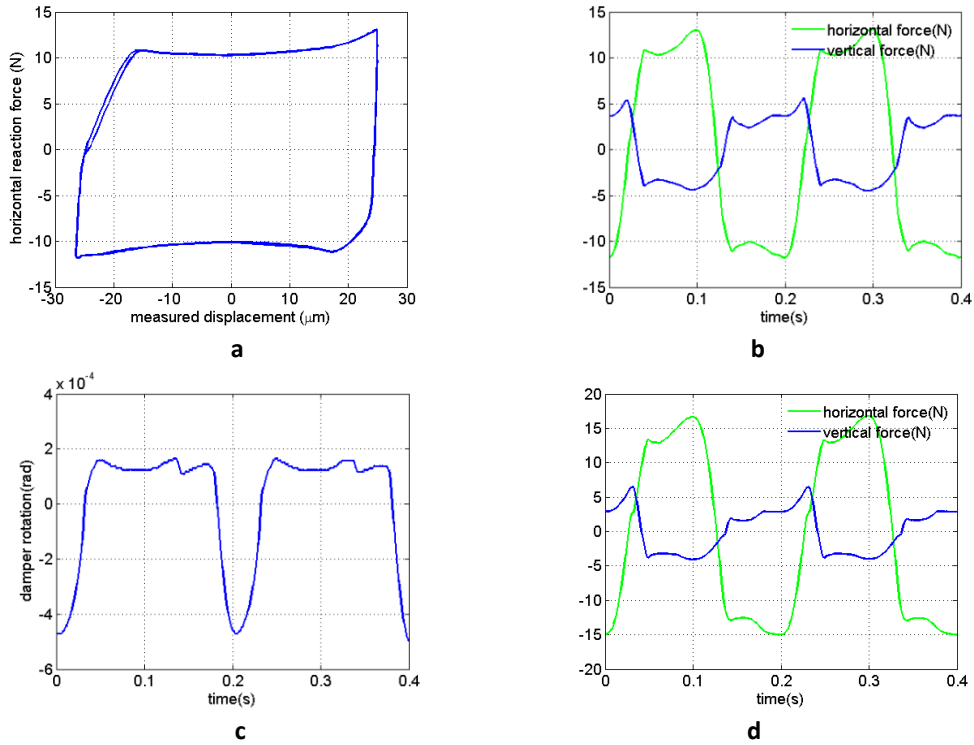


Fig.4.16

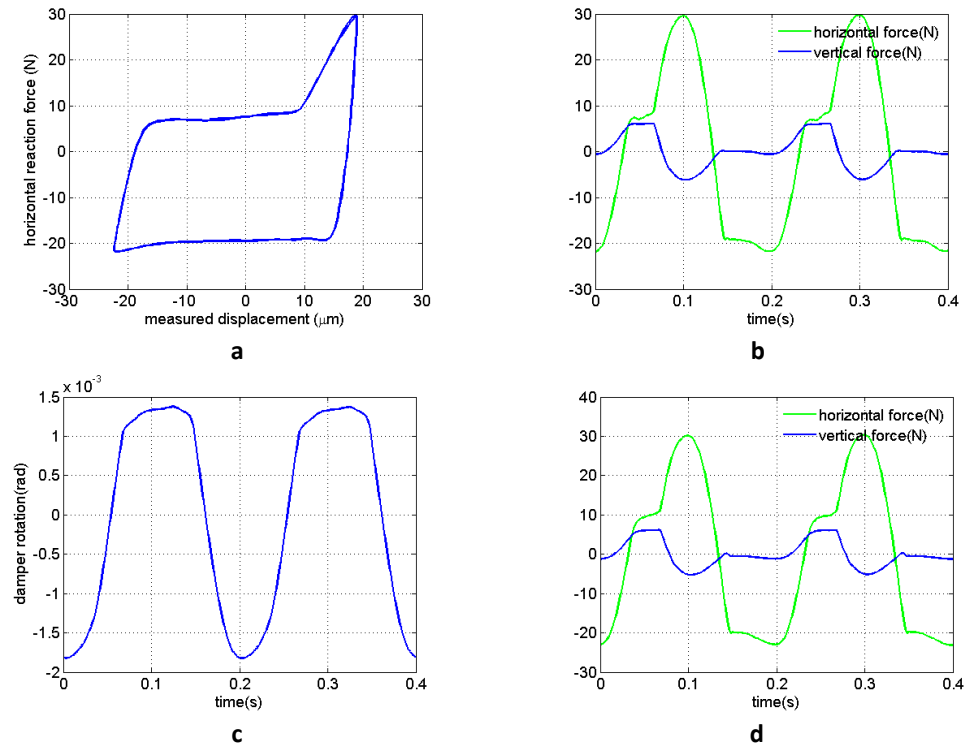


Fig.4.17

For Fig.4.18, only the rotation(sub diagram a, c, e), and correspondent measured force(sub diagram b, d, f) are shown. The case from c and d is similar with the case demonstrated in Fig.4.17 even if the frequency is higher. The case from a and b is a transient stage similar with case in Fig.4.16. The case from e and f represents a state when the contact force is very high to prevent macro-slip and the rotation is less than the case when a macro 'shoe shape' happens.

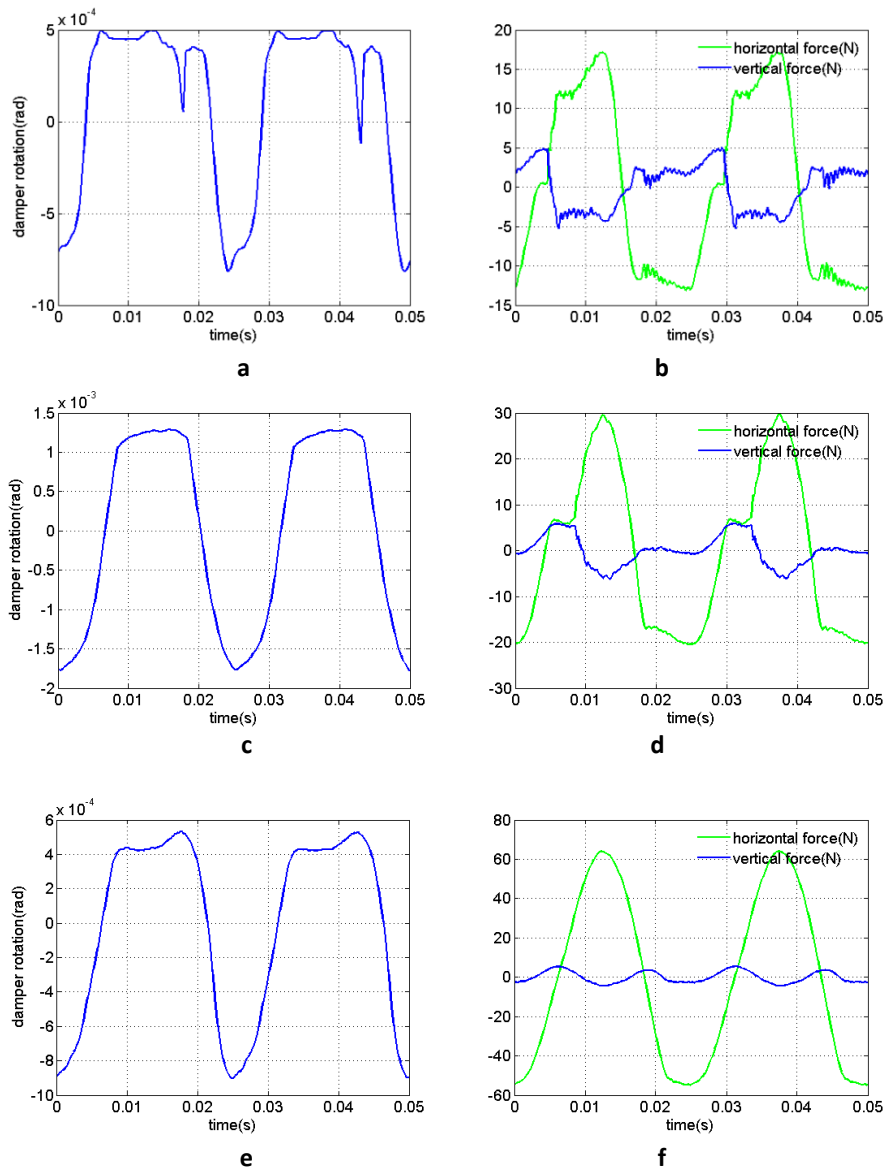


Fig.4.18

4.3 In-phase results of three-point damper

4.3.1 Hysteresis characteristics

As mentioned in the literatures, the in-phase motion for a wedge-shaped under-platform damper is more critical due to potential rotation during the relative movement between two adjacent platforms, which can reduce energy dissipation significantly. The hysteresis is a direct clue demonstrating the energy dissipation on the interfaces, thus also reflecting the rotation level.

Typical in-phase hysteresis of the three-point damper under following conditions are shown in Fig.4.19.

motion type	nominal amplitude	excitation frequency	dead weight
in-phase	20 μ m (Fig.3.19.a)	5Hz (Fig.3.19.a-b)	4.65kg
	60 μ m (Fig.3.19.b-c)	40Hz(Fig.3.19.c)	

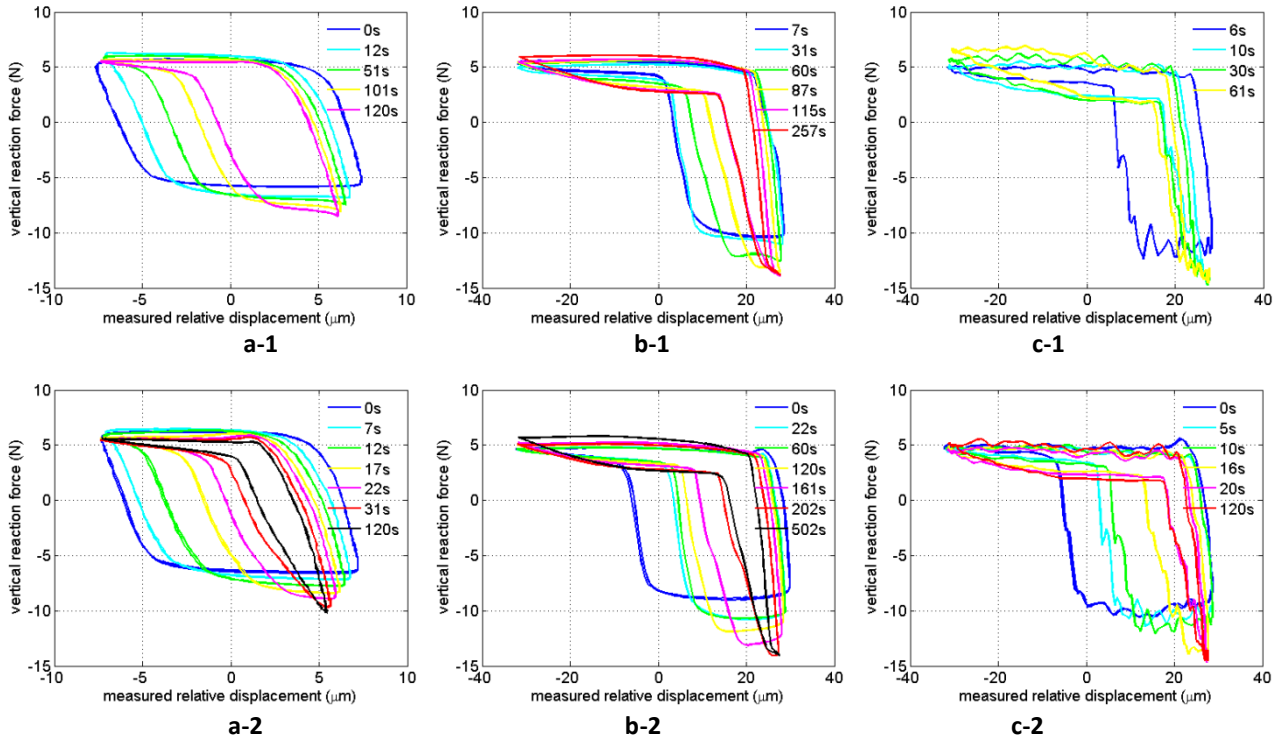


Fig.4.19

It can be observed from Fig.4.19 that under in-phase motion, the evolution of hysteresis does not follow the same principle as out-of-phase condition. The contact force excursion with time is not times increased from the initial value, which means the damper is not stuck at the final of tests. The possible macro-slip stage (labeled by the red ellipse in subplot a) shrinks during the test for both small and large motion amplitude.

The visual stiffness k_v for in-phase is less than k_h and this is possibly due to rotation happened with the stick state.

4.3.2 Damper motion reconstruction

To better demonstrate the damper motion for certain hysteresis shape, the measurement of damper rotation and one point vertical motion are linked to reconstruct damper kinematics. The difficulty of lacking lasers measuring all the needed motion quantities at the same time is overcome by synchronizing the force signals measured at different time. So for constructing one motion picture, at least 3 tests are needed, which are denoted as PD for platform relative displacement, RD for damper rotation and VD for one point vertical displacement.

Example 1:

motion type	nominal amplitude	excitation frequency	dead weight
in-phase	$60\mu m$	40Hz	4.65kg

Fig.4.20 is the force synchronized force signal from three tests, in which color blue is from test PD, color red is from test RD and color green is from test VD.

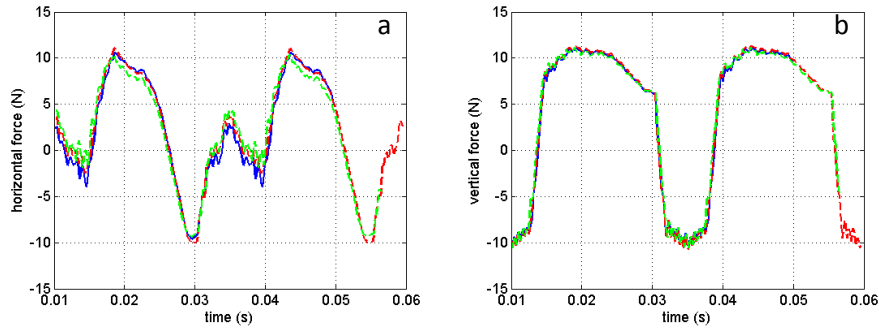


Fig.4.20 Force signal synchronization(the signals are averaged for the convenience of comparison)

Take the PD measurement as reconstruction base. Fig.4.21 shows the hysteresis shape, corresponding measured force shape and measured motion quantities. The color arrangement of subplot c follows Fig.4.20.

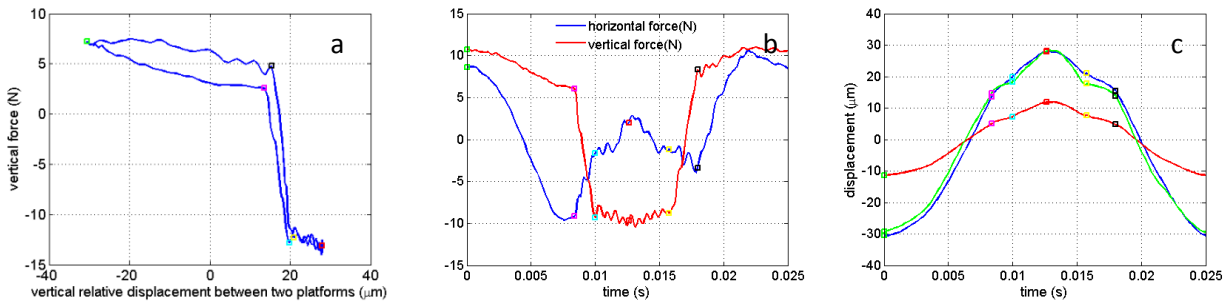


Fig.4.21 Hysteresis shape and motion measurement from example 1

The reconstructed motion is divided into 6 stages in this case according to the labeled points shown in the hysteresis. Here it is noted that for visual ability, in the motion plots of example 1-3, $1mm$ stands for $10\mu m$ and the rotation is increased for 100 times. In example 4, $1mm$ stands for $5\mu m$ and the rotation is increased for 200 times.

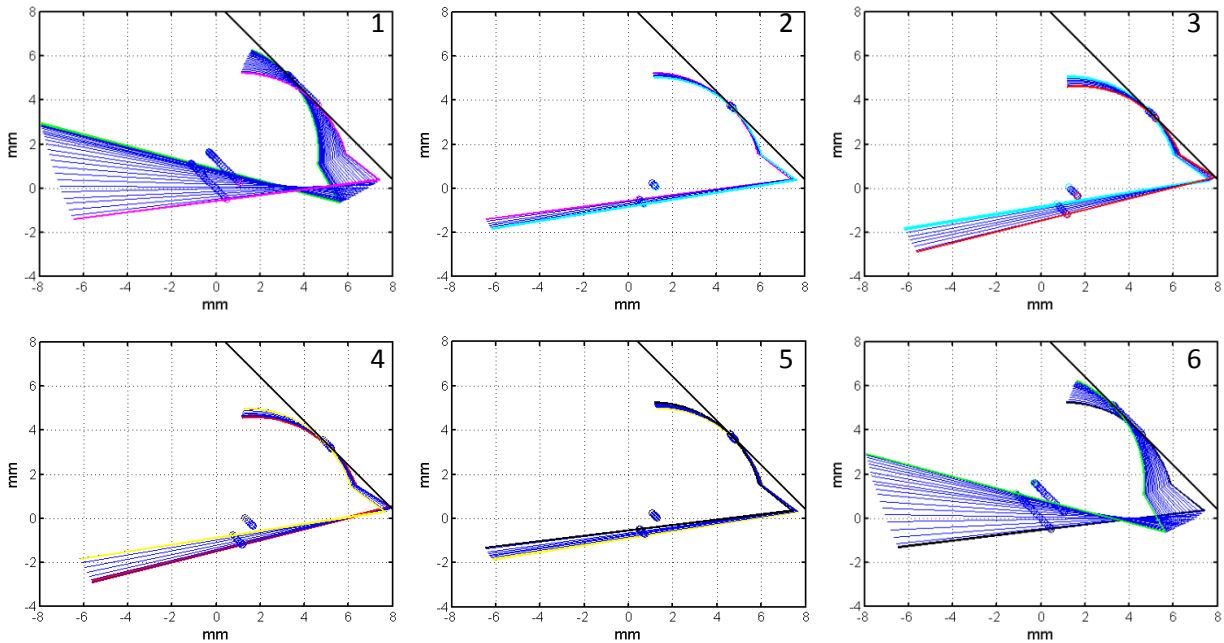


Fig.4.22

From Fig.4.22, it is convenient to understand what happens to the damper motion at each stage. For 1 and 6, the damper experiences large rotation; for 3 and 4, local rolling happens; for 2 and 5, the damper surfaces are in opposite stick state.

Example 2:

motion type	nominal amplitude	excitation frequency	dead weight
in-phase	$60\mu m$	5Hz	4.65kg

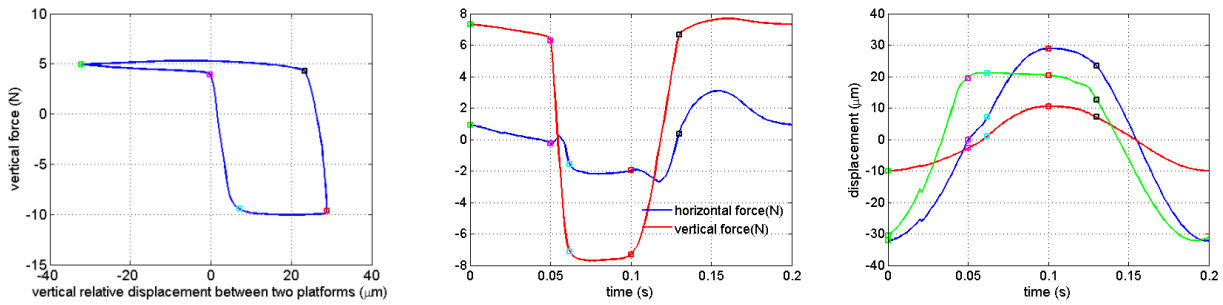


Fig.4.23 Hysteresis shape and motion measurement from example 2

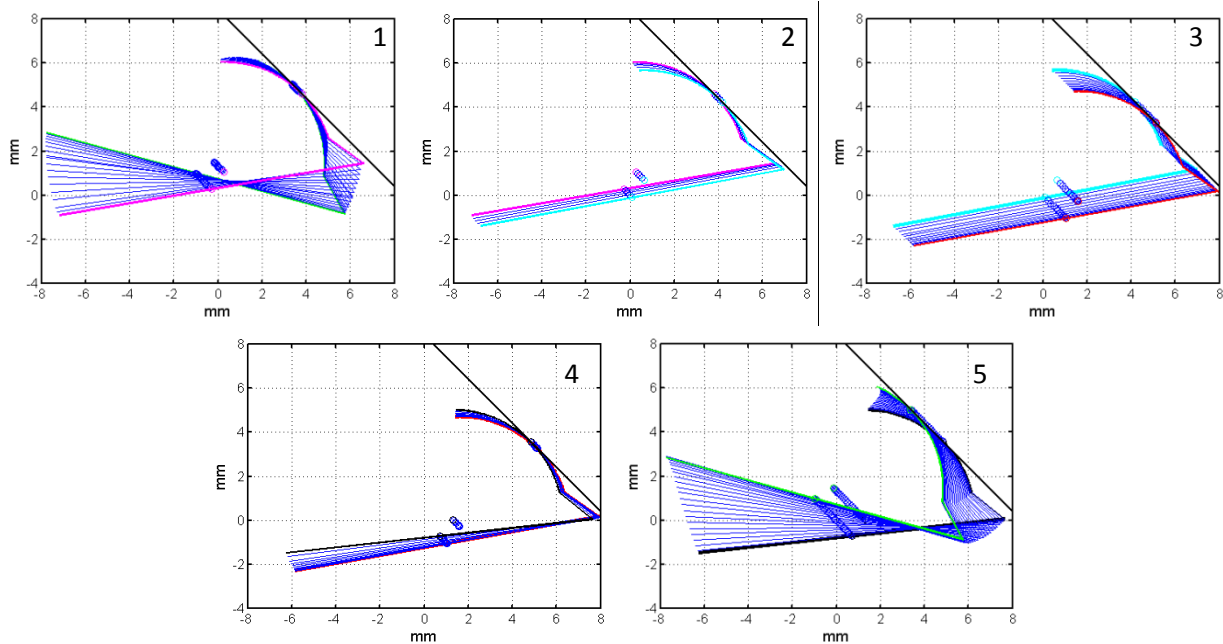


Fig.4.24

Example 3:

motion type	nominal amplitude	excitation frequency	dead weight
in-phase	$60\mu m$	5Hz	4.65kg

The nominal operation condition of this example is the same as example 2, but they have different hysteresis shape. The motion under this condition is similar with example 1, under different excitation frequency. Most rotations happen in the 1st and 6th stage.

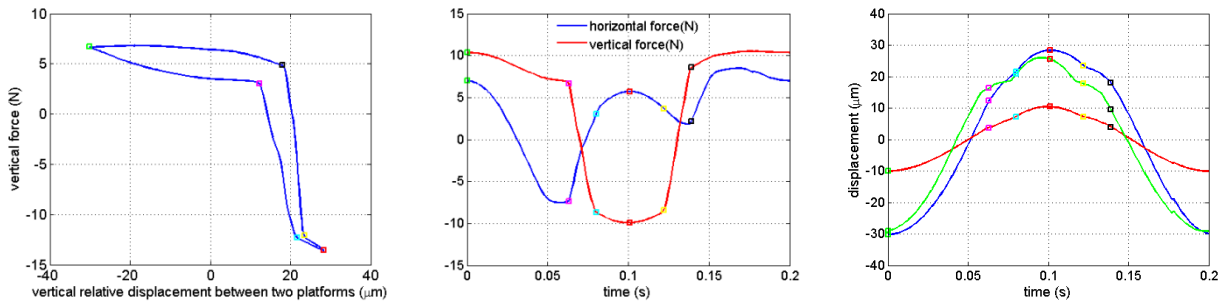


Fig.4.25 Hysteresis shape and motion measurement from example 3

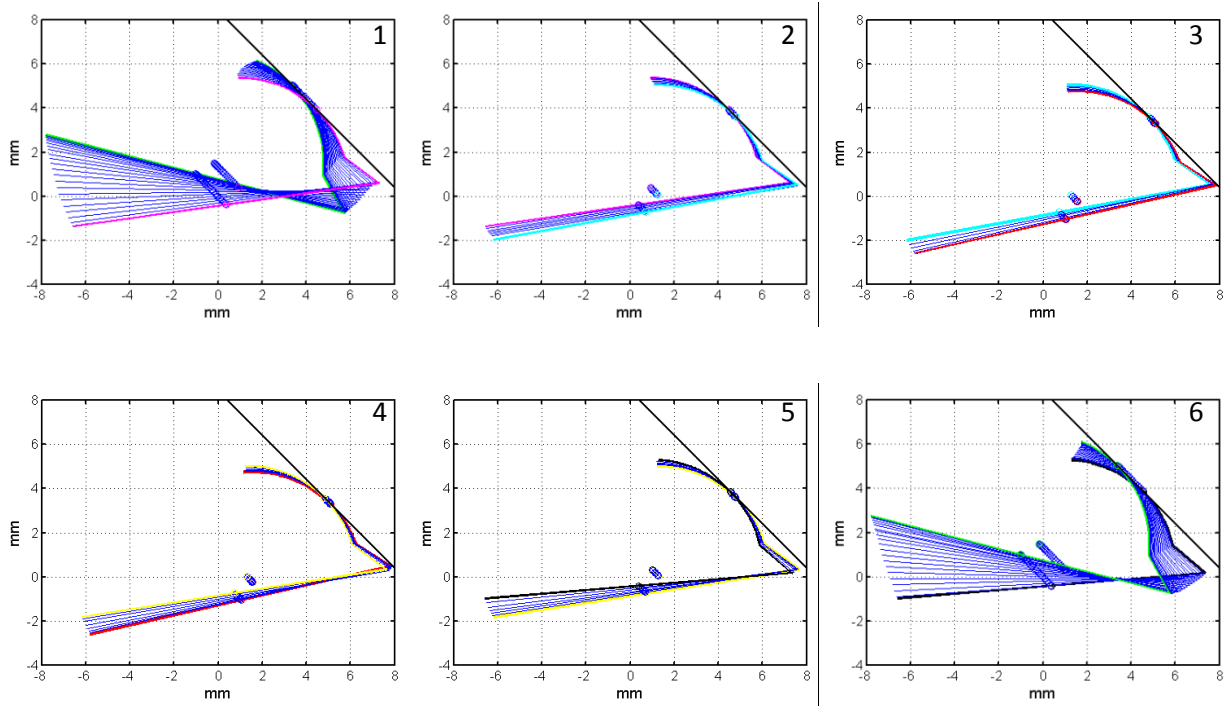


Fig.4.26

Example 4:

motion type	nominal amplitude	excitation frequency	dead weight
in-phase	20 μm	5Hz	4.65kg

For small nominal excitation amplitude, initially the hysteresis can have a traditional Coulomb like shape and damper rotation is small.

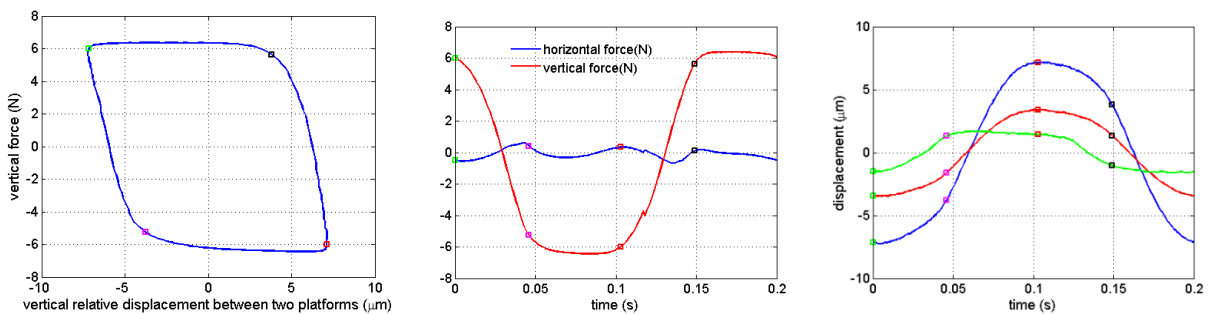


Fig.4.27 Hysteresis shape and motion measurement from example 4

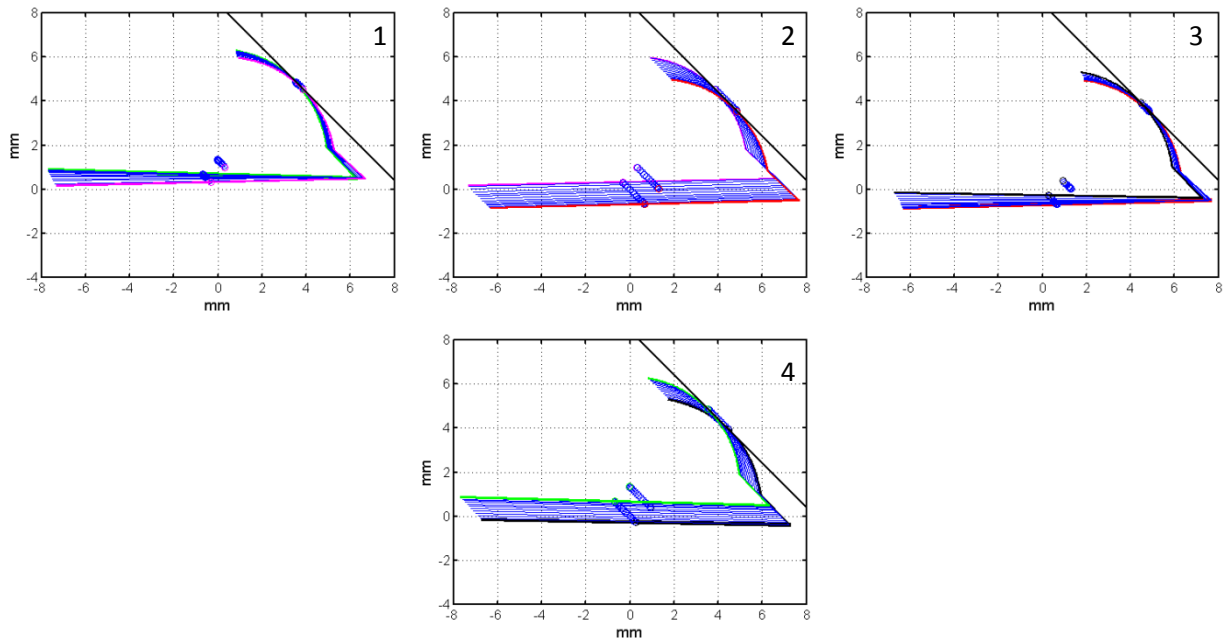


Fig.4.28

At this stage the damper motion is clear and intuitive. Furthermore, because the right curved surface of the damper is always in contact with the right platform, the relative movement between the contact points pair can be deduced according to the way discussed in chapter 3. The results are shown in Fig.4.29 for example 1-4. Here the errors are not shown, the estimations can be referred to the value in section 3.2.2. The word ‘sliding’ is not accurate actually, it means the displacement between the contact surfaces caused by damper translation, either spring loading in stick condition or sliding in slip condition.

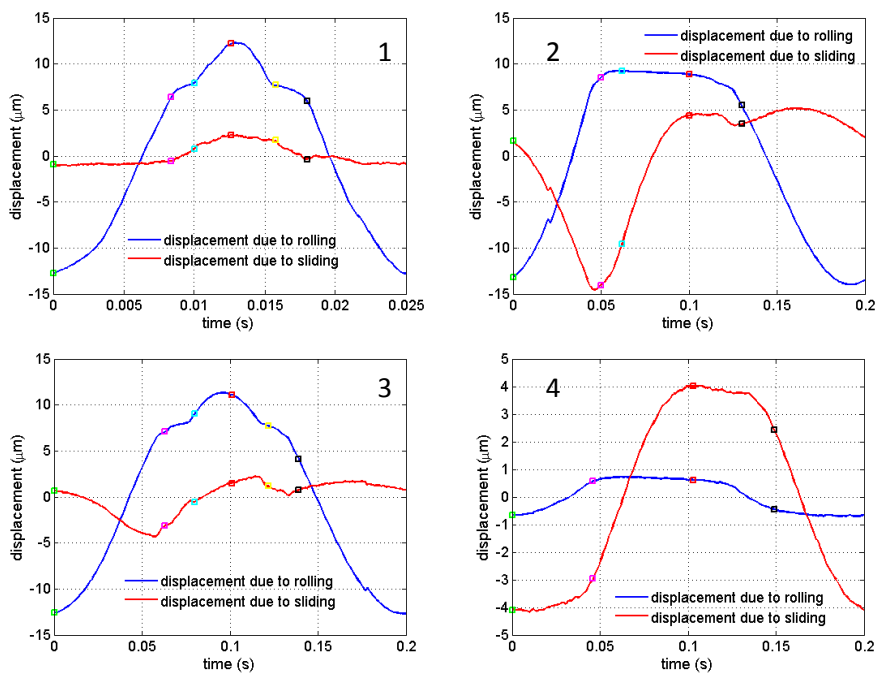


Fig.4.29

In example 1, the displacement due to sliding on the right contact point is very small, the contact point is used like a hinge during operation. Example 3 is similar to 1. In example2, there are two

stages in which one has mostly sliding and the other mostly rolling. In example 4, small rotations happen together with tangential spring loading. The complex situations again show the difficulty to predict damper behavior.

4.3.3 Contact force distribution

In this section the force distribution diagrams (corresponding to example 1-4 from last section) are shown to provide more information investigating the damper performance. In each figure, subplot a is the hysteresis, b is the proportion between tangential and normal contact force on each surface, c is the force distribution demonstration.

Fig.4.30 shows a case similar to example 1. It is clear that in the stage between green and pink point, between black and green point, the resultant force on the left surface passes through the lower contact point, implying the upper contact point loses the contact. When hysteresis moves to the red point, the lower contact point loses the contact and resultant force moves to the upper contact point. From subplot b, it can be deduced that the right surface is always in stick state or small micro-slip while the left surface can experience some macro-slip. This information will be used in the numerical simulation by assigning certain value to the nominal parameter: friction coefficient at the interface.

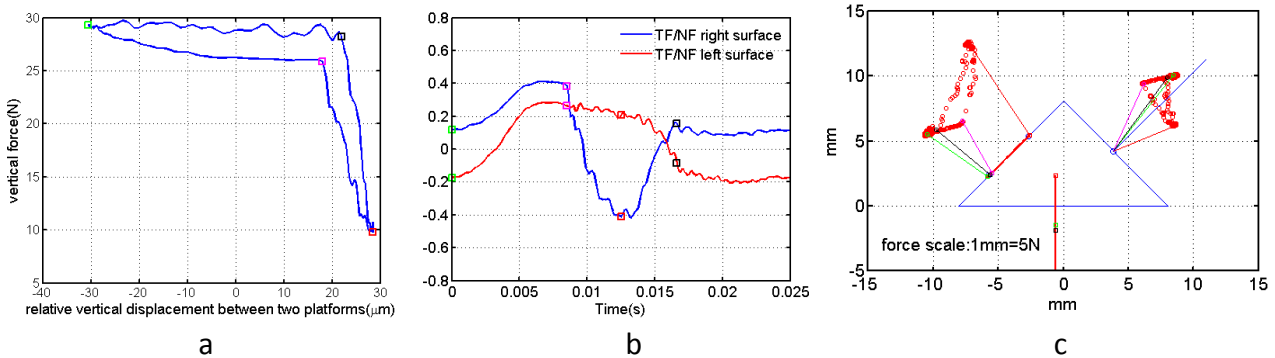


Fig.4.30

Fig.4.31 shows a case similar to example 2. The resultant force on left surface does not reach upper contact point, which means the lower contact point is always in contact with left platform. There is a stage between blue and red point that both surfaces are in slip state. Between green and pink point, between black and green point, it is still difficult to predict what happens without further demonstration, which means a numerical model is needed.

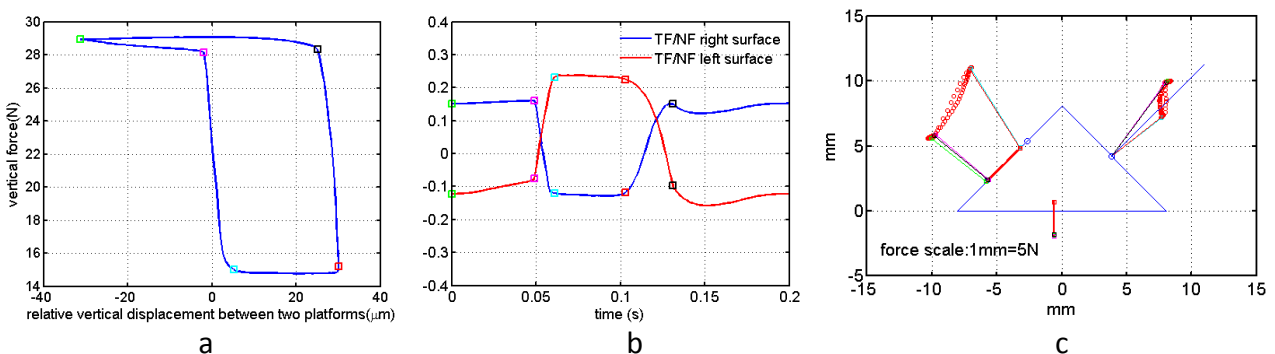


Fig.4.31

Fig.4.32 shows a case similar to example 3. Like the description of Fig.3.30, here the right surface is always in stick or micro-slip state while the states of two contact points on left surface are not predicted. There should be one point experiencing slip during operation because the hysteresis shows certain amount of energy dissipation.

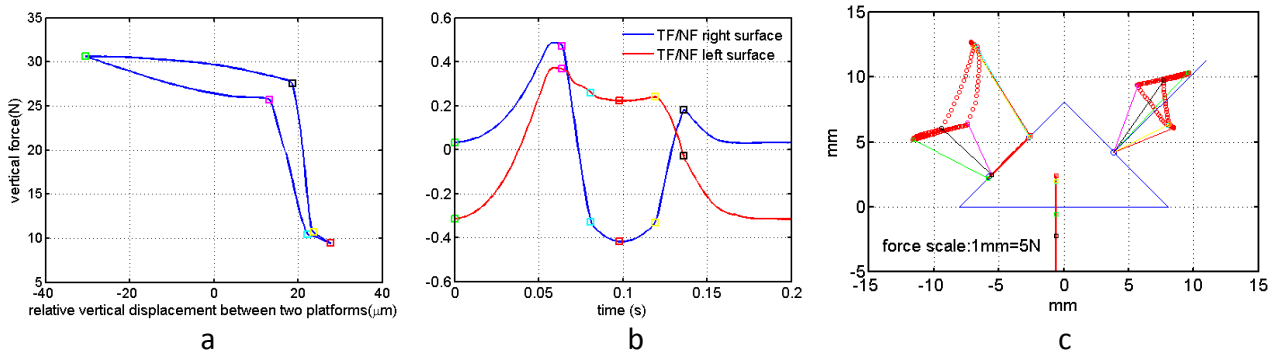


Fig.4.32

Fig.4.33 shows a case similar to example 4. In this case the resultant force does not reach the limit position of any contact point, which means both contact points are always in contact with respective platforms during the cycle. There is a regular mutual transition between stick and slip state for both surfaces. Micro-slip phenomena exist.

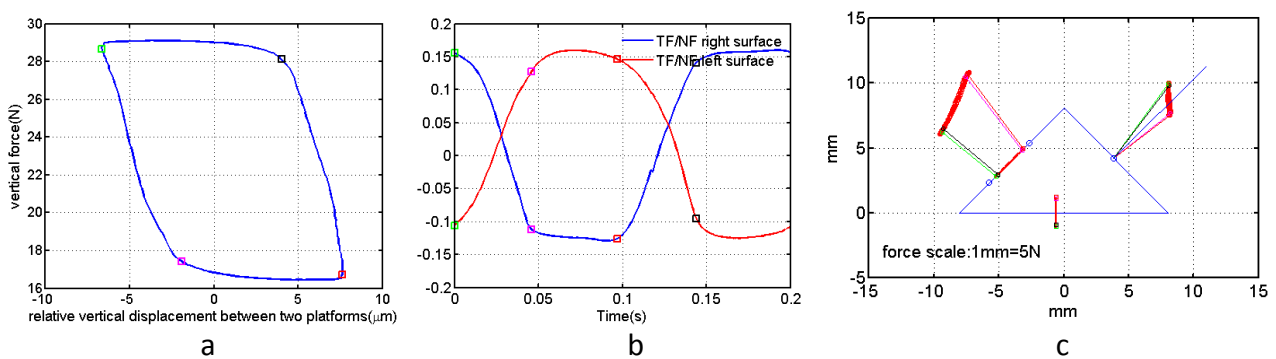


Fig.4.33

4.4 In-phase results of crossed curve-flat damper

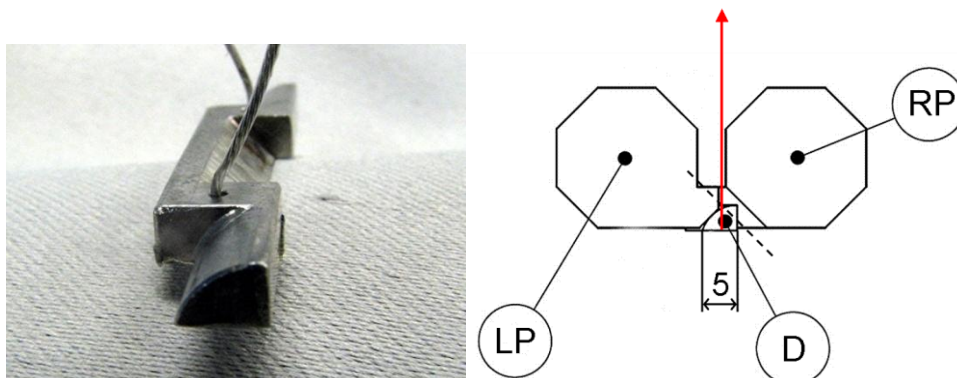


Fig.4.34 Configuration of the crossed curve-flat damper

The tests made on the wedge shaped three point damper show that the damper is efficient under out-of-phase condition if the contact force amplitude can be controlled to prevent a final stuck state especially for high frequency excitation. Under in-phase condition this damper is not efficient due to large potent of rotation even at very low frequency. Based on the consideration to reduce damper rotation, a laboratory crossed curve-flat damper is designed as shown in Fig.3.34. The purpose of crossed shape is to make the contct point positions on two surfaces overlap and make the line between this overlapping position near to the mass center(here equivalently to centrifugal force application position) to avoid damper rotation.

4.4.1 Typical hysteresis

Hysteresis measurement is shown under different operating condtions listed below. The difference between the hysteresis of this damper and three-point damper is significant. Fig.4.35- Fig.4.38 show 4 groups of measured hysteresis.

Group1:

motion type	nominal amplitude	excitation frequency	dead weight
in-phase	60 μ m	5Hz	2.65kg

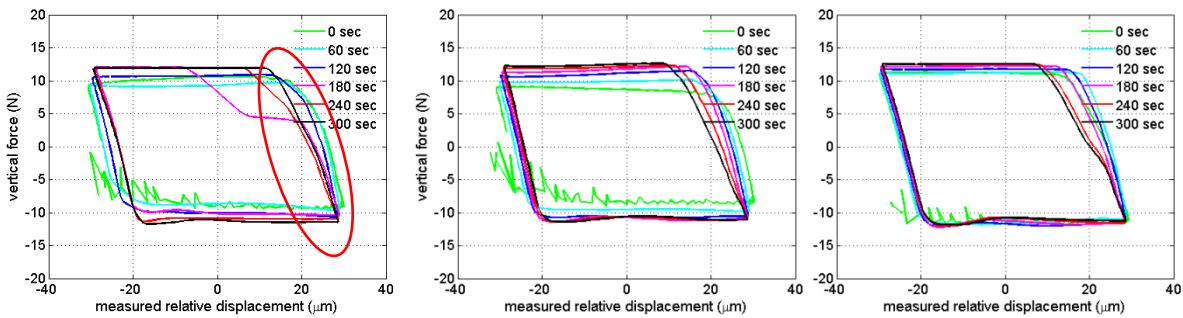


Fig.4.35 Hysteresis sample of group 1

Group2:

motion type	nominal amplitude	excitation frequency	dead weight
in-phase	60 μ m	5Hz	4.65kg

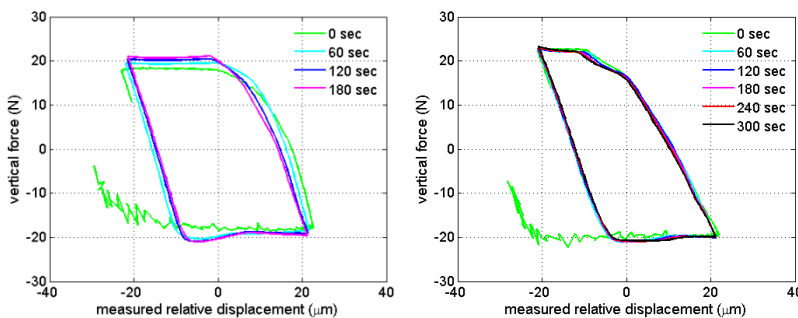


Fig.4.36 Hysteresis sample of group 2

Group3:

motion type	nominal amplitude	excitation frequency	dead weight
in-phase	60 μm	40Hz	2.65kg(Fig.3.37.a,b)
			4.65kg(Fig.3.37.c)

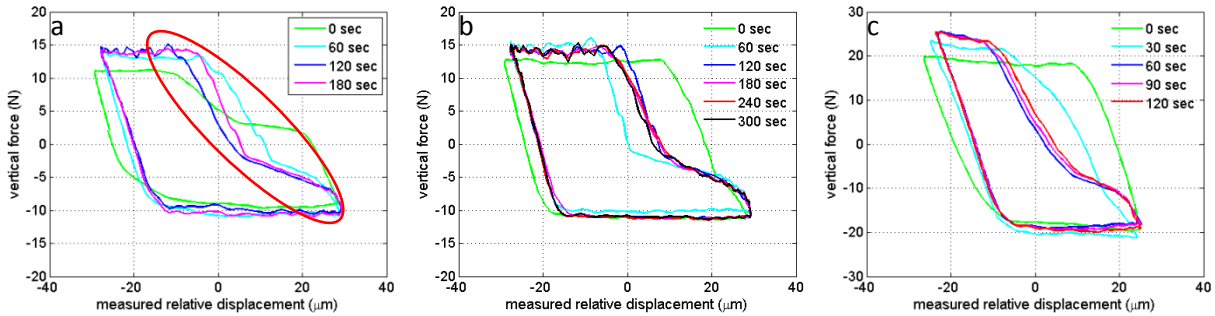


Fig.4.37 Hysteresis sample of group 3

Group4:

motion type	nominal amplitude	excitation frequency	dead weight
in-phase	20 μm	5Hz	2.65kg(Fig.3.38.a)
			4.65kg(Fig.3.38.b)

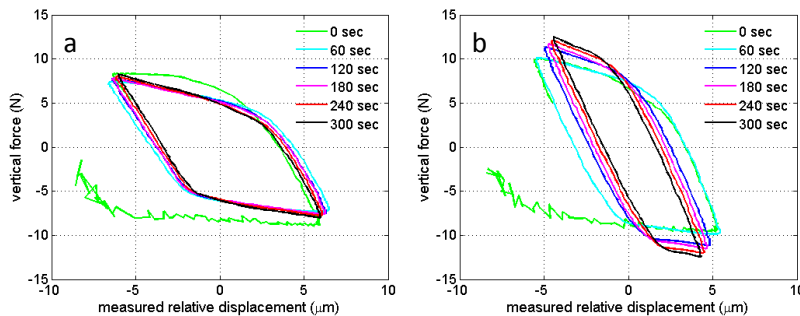


Fig.4.38 Hysteresis sample of group 4

Here the features of crossed curve-flat damper in-phase hysteresis are summarized:

Generally this damper gives good friction damping behavior for both low and high preload. The hysteresis has a Coulomb shape except for the part labeled by a red ellipse in Fig.4.35 and Fig.4.37. From the previous experience, the unsymmetric part arises from possible rotation, which can be found from the wear trace in Fig.4.39. The wear process contributes a lot to the variability of measurement results by changing contact position and parameters.



Fig.4.39 Wear trace on the flat surface of crossed curve-flat damper

4.4.2 Contact force distribution

By neglecting the damper inertial force and contact position variability, the contact force distribution is constructed.

motion type	nominal amplitude	excitation frequency	dead weight
in-phase	60 μm	5Hz	2.65kg

Two examples according the above condition are shown in Fig.4.40 and Fig.4.41.

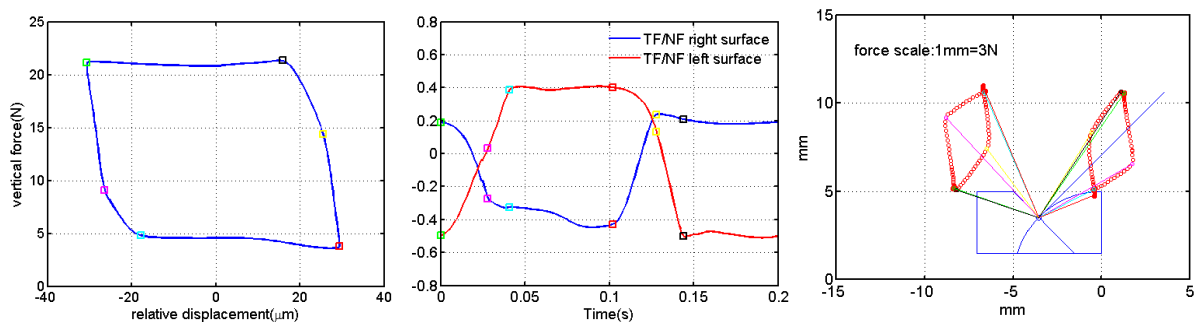


Fig.4.40 Contact force distribution of example 1

Combining above 3 subplots, the stages in one cycle are as follows(starting from green point):

- 1 Both sides stuck(left surface unloaded upward, right surface unloaded downward).
- 2 Left surface stuck, right surface slipping down, forces change.
- 3 Both sides slipping(left surface up, right surface down), forces sustain.
- 4 Both sides stuck(left surface unloaded downward, right surface unloaded upward).
- 5 Left surface stuck, right surface slipping up, forces change.
- 6 Both sides slipping(left surface down, right surface up), forces sustain.

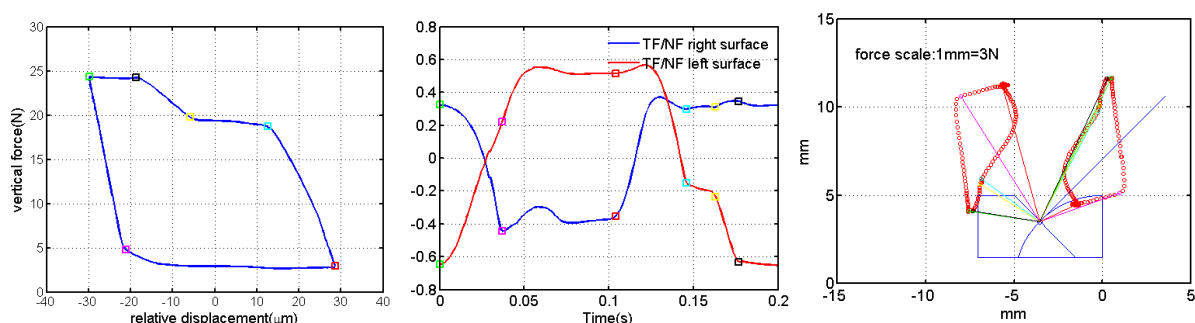


Fig.4.41 Contact force distribution of example 2

In the case of Fig.4.41, the stages in one cycle are as follows(starting from green point):

- 1 Both sides stuck(left surface unloaded upward, right surface unloaded downward), forces change.
- 2 Left surface stuck(unloaded upward), right surface slipping down, forces change.
- 3 Both sides slipping(left surface up, right surface down)
- 4 Left surface slipping up, right surface stuck(unloaded upward).
- 5 Left surface stuck(unloaded downward), right surface slipping up, forces change.

6 Left surface stuck(unloaded downward), right surface slipping up, forces sustain(possible lost of contact points).

7 Stage 6 continues.

8 Both sides slipping (left surface down, right surface up), forces sustain.

It is clear that when the surface condition in contact has great variability during operation, the damper equilibrium and motion will be complex.

4.5 Out-of-phase results of crossed curve-flat damper

Hysteresis obtained under the following conditions are shown in Fig.4.42.

motion type	nominal amplitude	excitation frequency	dead weight
out-of-phase	20 μm (Fig.4.42.1-3)	5Hz(Fig.4.42.1, Fig.4.42.4)	2.65kg(Fig.4.42.1-3)
	60 μm (Fig.4.42.4-6)	40Hz(Fig.4.42.2, Fig.4.42.5)	4.65kg(Fig.4.42.4-6)
		80Hz(Fig.4.42.3, Fig.4.42.6)	

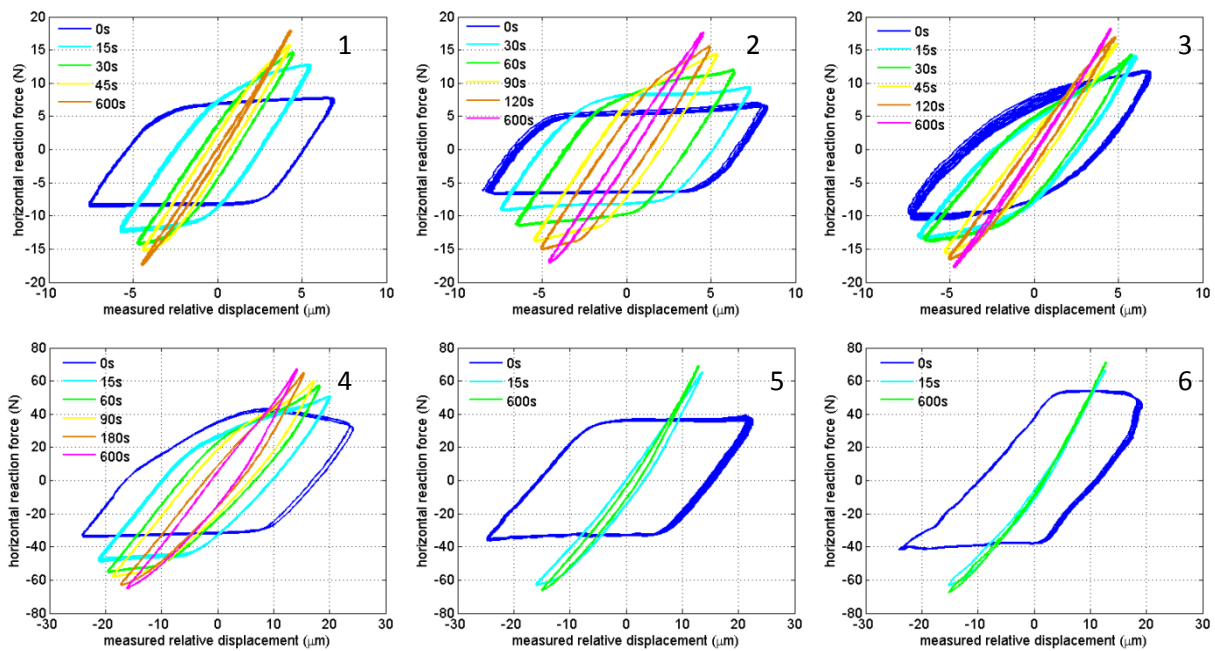


Fig.4.42 Hysteresis examples for crossed curve-flat damper

The examples shown in Fig.4.42 are regular measured hysteresis, but in some tests irregular hysteresis is found like in Fig.4.43.

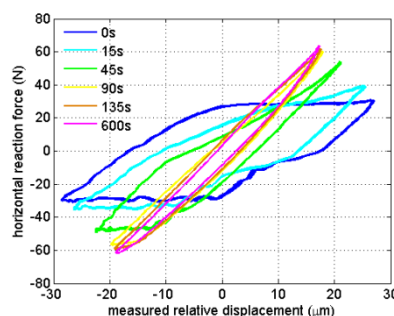


Fig.4.43 Irregular hysteresis example(60 μ m,40Hz,2.65kg)

The irregularity is caused by the contact condition change, which is difficult to control. Fig.4.44 show the energy dissipation under different operation conditions from a group of tests.

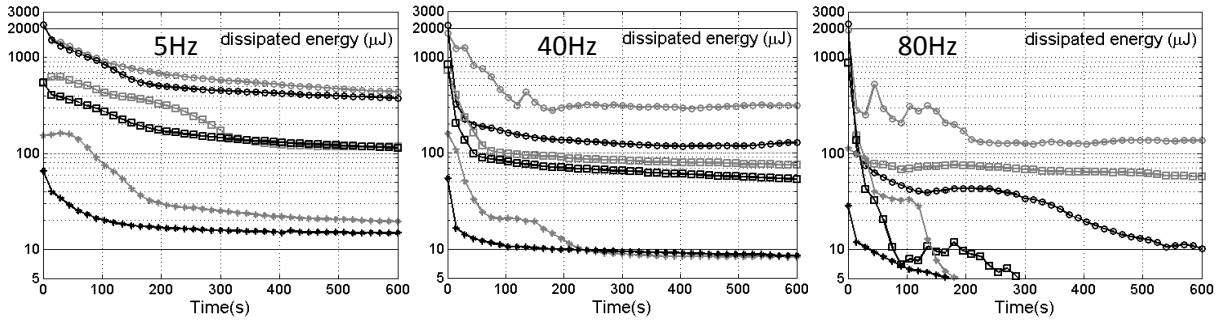


Fig.4.44 Energy dissipation(black color:4.65kg grey color:2.65kg)
O - 60 μ m nominal □ - 40 μ m nominal * - 20 μ m nominal

The results clearly show the hysteresis evolves to micro-slip stage which dissipates small energy during the cycle.

4.6 In-phase results of non-crossed curve-flat damper

Initially this damper is expected to tend to rotate a lot during in-phase motion because the long distance between the two contact position on each surface. Fig.4.45 shows the features of hysteresis and corresponding distribution.

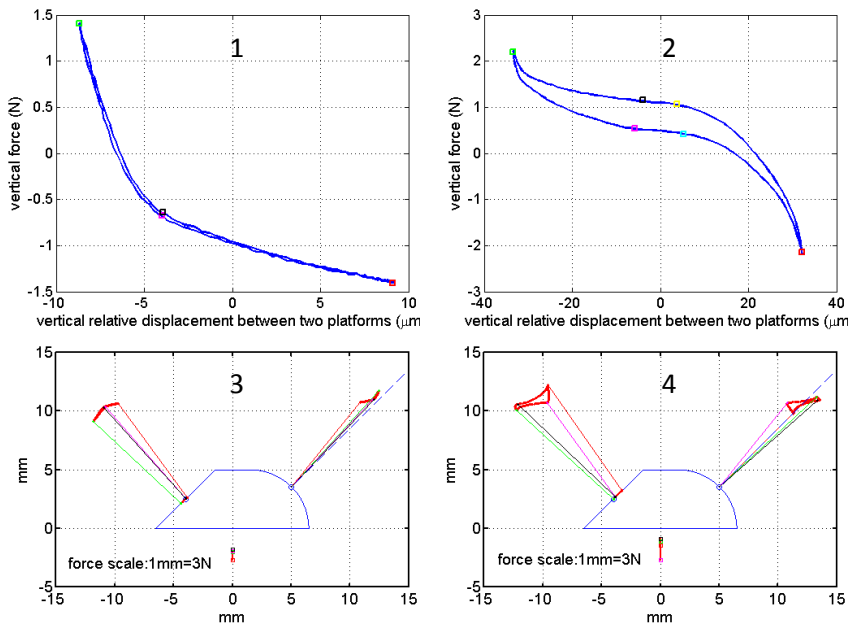


Fig.4.45 Typical in-phase hysteresis and force distribution for non-crossed curve-flat damper
Left: 5 Hz, 20 μ m, 4.65kg Right: 5 Hz, 60 μ m, 4.65kg

The experiment verifies that this configuration of curve-flat damper is not efficient under in-phase condition. After many cycles of in-phase motion(both low and high frequency), there is no wear trace on the contact surfaces.

4.7 Conclusions

Three dampers with different geometries are tested.

The three-point damper is investigated in detail to understand more about normal wedge-shaped under-platform damper behavior in the sense of kinematics and equilibrium.

The meaning of visual stiffness given by the measured hysteresis slope when both sides are in stick state is demonstrated.

In the operational frequency range, the three-point damper works in a mutual stick-slip influence between the two interfaces, which is predicted in literature and now experimentally verified. The scheme of this mutual influence leads to different shapes of hysteresis cycle and damper equilibrium and in consequence the damper kinematics show different features. Friction coefficient is an important parameter which may influence the complexity of this scheme. When the friction coefficient is changed, the contact points on left surface may experience absence of contact for both out-of-phase and in-phase conditions.

Under out-of-phase condition, the final hysteresis shows a micro-slip state with high friction coefficient and contact force. Under in-phase condition, the final hysteresis keeps a state with large rotation and relatively low friction coefficient and contact force.

The increase of simulated centrifugal force can accelerate the evolution of contact condition.

From the current experimental device and methods, damper motion is reconstructed with marked accuracy.

The crossed curve-flat damper is designed intentionally to reduce the rotation effect from the common wedge-shaped damper. The experiments verify this advantage. But due to the contact surface wear, there can happen possible rotations shown in the hysteresis. Due to the experimental limitation, the damper motion is not reconstructed. Under out-of-phase condition especially when higher preload is applied, the hysteresis evolves to micro-slip stage fast.

The non-crossed curve-flat damper is intentionally to be compared with the previous two dampers under in-phase motion. The results show it slips very little and mostly rolls. The imperfection of the left flat surface (might have a large curvature) can promote the rotation effect. So in practice, this shape should not be used.

The test rig shows limitations when high frequency excitations are imposed due to the flexibility of the structure.

Chapter 5 Numerical simulation of damper motion with direct time integration

Apart from remarkable repeatability and reasonable intuitive demonstrations, the experimental results also show great complexity and uncertainty of damper behavior, which leads to the need of system modeling to understand better what happens in detail and predict new types of damper behavior reliably.

5.1 Overview of Den Hartog's solution

In 1931 J.R.Den Hartog published his paper on steady state of forced vibration of a SDOF mechanical system with Coulomb friction or combined Coulomb friction and viscous damping.

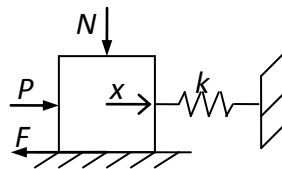


Fig.5.1 SDOF system considered by Den Hartog

Considering only dry friction, the differential equation of motion of the mass in Fig.5.1 is:

$$m\ddot{x} + kx \pm F = P \cos(\omega t + \varphi) \quad (1)$$

Where the + sign holds when the mass moves in the +x direction and vice versa. The phase angle φ is included for the purpose of subsequently writing the boundary condition in a convenient form. Den Hartog proposed two possible steady state motion patterns, one without stop during motion(case (a)) and one with one stop during half a cycle(case (b)), which are shown in Fig.5.2.

In case (a) during the half-cycle of the motion $0 < t < \pi / \omega$ the velocity is always negative so that (1) holds with - sign before F . Using the abbreviations: $P/k = a$, $F/k = x_f$, $k/m = \omega_n^2$, the differential equation in that interval is rewritten as:

$$\ddot{x} + \omega_n^2(x - x_f) = a\omega_n^2 \cos(\omega t + \varphi) \quad (2)$$

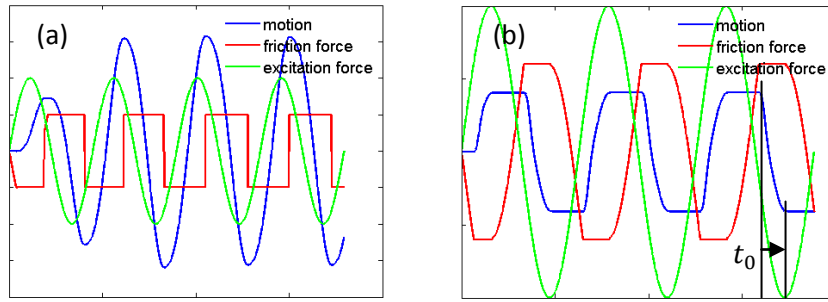


Fig.5.2 Two possible patterns of a SDOF motion with friction

Denote the response amplitude as x_0 . A steady-state solution corresponding to case (a) has to fulfill the following boundary conditions(consider half a cycle due to the symmetry):

$$\begin{cases} t=0 & x=x_0 & \dot{x}=0 \\ t=\pi/\omega & x=-x_0 & \dot{x}=0 \end{cases} \quad (3)$$

In case (b) there is motion during the interval $0 < t < t_0$ and standstill during $t_0 < t < \pi/\omega$. During the interval of motion the equation (2) holds, while the boundary conditions are:

$$\begin{cases} t=0 & x=x_0 & \dot{x}=0 \\ t=t_0 & x=-x_0 & \dot{x}=0 \end{cases} \quad (4)$$

Then the equations can be solved with respective boundary conditions. Fig.5.3 shows the boundary line between no stop and one stop motion in the frequency response diagram.

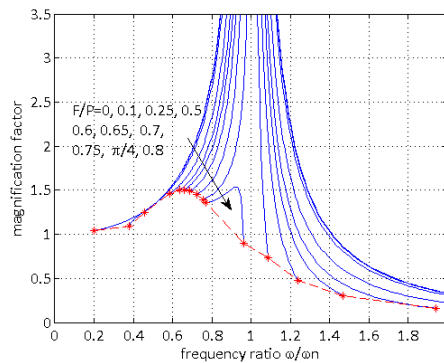


Fig.5.3 Boundary line of no stop motion and one stop motion from Den Hartog

The motion pattern proposition is not intuitive because naturally people do not consider that the movement of a body under a periodic excitation have one or more stops in half a cycle. His analysis tells us some interesting properties due to friction in vibration. For example, in a vibration only with dry friction damping, when the friction ratio F/P is smaller than $\pi/4$, the amplitude of vibration at resonance still extend to infinity. But if the value has a tiny increase(larger than $\pi/4$), the amplitude will immediately be decreased to a finite. Meanwhile there is the associated feature that the phase-frequency diagram is discontinuous when passing the resonance frequency. This phenomenon is different from viscous damping which suppresses the amplitude to finite value even at resonance. In some means the system dynamical behavior is not stable at resonance frequency when the friction coefficient is around $\pi/4$. His solution of motion equation with one stop or more than one stop in half a cycle was found in his experiments.

Den Hartog did not consider the stiffness between the two contact surfaces, which is satisfactory for most macro motions where the contact stiffness is rather high. Den Hartog's analytical solution is a base for comparing numerical calculation.

5.2 Direct time integration for motion equations with dry friction

In complex mechanical systems it is difficult to obtain analytical solution (or closed form) of motion with dry friction due to the nonlinear behavior of friction force, which is from the mutual dependence of friction force and relative movement, especially when there are more than one contact interfaces. HBM(Harmonic Balance Method) is usually used in approximate analytical solution of such systems and in most cases the result is satisfactory. But HBM is not sufficient to predict the whole features because one harmonics or even more are not enough to represent the dynamics when friction dominantly influences the system.

In this thesis, the main purpose is to understand better the damper kinematics and dynamics with certain geometry under certain excitation type. Except the centrifugal force as an external force, the left forces applied on the damper are from contact surfaces, which show great nonlinearity due to friction and geometry coupling. So it is necessary to find a reliable direct integration scheme to get the main features of a dynamic system with dry friction. Based on this idea, Newmark- β method is studied to perform this numerical integration.

Newmark- β method was developed based on acceleration interpolation in structural dynamics in the 1960s. It has some favorable properties such as unconditionally stable when the parameters are chosen properly and having enough precision. A short description of Newmark- β method is as following.

For an time interval Δt , apply Taylor series and linear combination of accelerations at time t and $t+\Delta t$ and choose two different control constants γ and β , the following relations are derived.

$$\{\dot{x}\}^{t+\Delta t} = \{\dot{x}\}^t + \{\tilde{\ddot{x}}\} \cdot \Delta t \quad (5)$$

$$\{\tilde{\ddot{x}}\} = \{\ddot{x}\}^t + \gamma(\{\ddot{x}\}^{t+\Delta t} - \{\ddot{x}\}^t) \quad (6)$$

$$\{\dot{x}\}^{t+\Delta t} = \{\dot{x}\}^t + (1-\gamma)\Delta t \cdot \{\ddot{x}\}^t + \gamma\Delta t \{\ddot{x}\}^{t+\Delta t} \quad (7)$$

$$\{x\}^{t+\Delta t} = \{x\}^t + \{\dot{x}\}^t \cdot \Delta t + \frac{1}{2}\{\bar{\ddot{x}}\} \Delta t^2 \quad (8)$$

$$\{\bar{\ddot{x}}\} = \{\ddot{x}\}^t + 2\beta(\{\ddot{x}\}^{t+\Delta t} - \{\ddot{x}\}^t) \quad (9)$$

$$\{x\}^{t+\Delta t} = \{x\}^t + \Delta t \cdot \{\dot{x}\}^t + \frac{1}{2}(1-2\beta) \cdot \Delta t^2 \{\ddot{x}\}^t + \beta \cdot \Delta t^2 \{\ddot{x}\}^{t+\Delta t} \quad (10)$$

Referring to (10), we have

$$\{\ddot{x}\}^{t+\Delta t} = \frac{1}{\beta \Delta t^2} (\{x\}^{t+\Delta t} - \{x\}^t) - \frac{1}{\beta \Delta t} \{\dot{x}\}^t - \left(\frac{1}{2\beta} - 1\right) \{\ddot{x}\}^t \quad (11)$$

Then the variables at time $t+\Delta t$ should satisfy the equilibrium equation.

To solve the nonlinear motion equations with dry friction, because the state variables are inter-dependent on friction force, it is necessary to bring in iteration scheme (like Newton-Raphson Method) to find the nonlinear equilibrium point.

According to the way that starts the iteration, there are force-based and displacement-based schemes.

$$[\mathbf{M}]_{n \times n} \{\ddot{x}\}_{n \times 1} + [\mathbf{C}]_{n \times n} \{\dot{x}\}_{n \times 1} + [\mathbf{K}]_{n \times n} \{x\}_{n \times 1} = \{\mathbf{F}_c\}_{n \times 1} + \{\mathbf{F}_e\}_{n \times 1} \quad (12)$$

The force-based scheme follows classical Newmark procedure and performs as follows.

$$a_0 = \frac{1}{\beta \Delta t^2}, \quad a_1 = \frac{\gamma}{\beta \Delta t}, \quad a_2 = \frac{1}{\beta \Delta t}, \quad a_3 = \frac{1}{2\beta} - 1, \quad a_4 = \frac{\gamma}{\beta} - 1, \quad a_5 = \frac{\Delta t}{2} \left(\frac{\gamma}{\beta} - 2 \right)$$

$$a_6 = \Delta t (1 - \gamma), \quad a_7 = \gamma \Delta t$$

$$\mathbf{K}_{eff} = [\mathbf{K}] + a_0 [\mathbf{M}] + a_1 [\mathbf{C}]$$

1 For integration step $i + 1$:

Assume contact forces $\{\mathbf{F}_c\}^{i+1,k} = \{\mathbf{F}_c\}^i$.

2 For iteration k :

2.1 Impose contact forces $\{\mathbf{F}_c\}^{i+1,k}$ and excitation forces $\{\mathbf{F}_e\}^{i+1}$ and get total forces

$$\{\mathbf{F}_{total}\}^{i+1,k} = \{\mathbf{F}_c\}^{i+1,k} + \{\mathbf{F}_e\}^{i+1}$$

and form the effective load

$$\{\mathbf{F}_{eff}\}^{i+1,k} = \{\mathbf{F}_{total}\}^{i+1,k} + [\mathbf{M}] (a_6 \{x\}^i + a_2 \{\dot{x}\}^i + a_3 \{\ddot{x}\}^i) + [\mathbf{C}] (a_1 \{x\}^i + a_4 \{\dot{x}\}^i + a_5 \{\ddot{x}\}^i)$$

2.2 Calculate the displacement

$$\{x\}^{i+1,k} = \mathbf{K}_{eff}^{-1} \{\mathbf{F}_{eff}\}^{i+1,k}$$

and find the acceleration and velocity

$$\{\ddot{x}\}^{i+1,k} = a_0 (\{x\}^{i+1,k} - \{x\}^i) - a_2 \{\dot{x}\}^i - a_3 \{\ddot{x}\}^i$$

$$\{\dot{x}\}^{i+1,k} = a_0 \{\dot{x}\}^i + a_6 \{\ddot{x}\}^i + a_7 \{\ddot{x}\}^{i+1,k}$$

2.3 Calculate the new contact forces $\{F_c\}^{i+1,k+1}$ with the displacements above according to contact state.

2.4 Check if $\{\Delta F_c\}^{i+1,k}$ satisfies the tolerance requirement: $\text{norm}(\{\Delta F_c\}^{i+1,k}) < \text{tol}$,

If yes, stop iterations and set the calculated state variable values as the values for current step and go to next step from 1, $i = i + 1$.

If no, go to 2.1, $k = k + 1$.

The force based iteration scheme is simple to be implemented but the update of contact force has less physical interpretation as displacement based scheme.

The displacement-based Newmark method starts the iteration from assumption of state variables and the scheme is as follows.

1 For integration step $i + 1$:

option 1 : Assume $\{x\}^{i+1,k} = \{x\}^i$, then from Newmark relation we have

$$\{\dot{x}\}^{i+1,k} = -\left(\frac{\gamma}{\beta} - 1\right)\{\dot{x}\}^i - \Delta t\left(\frac{\gamma}{2\beta} - 1\right)\{\ddot{x}\}^i \quad \text{and} \quad \{\ddot{x}\}^{i+1,k} = -\frac{1}{\Delta t \cdot \beta}\{\dot{x}\}^i - \left(\frac{1}{2\beta} - 1\right)\{\ddot{x}\}^i$$

Option 2: Assume $\{\ddot{x}\}^{i+1,k} = \{\ddot{x}\}^i$, then we have

$$\{\dot{x}\}^{i+1,k} = \{\dot{x}\}^i + \Delta t \cdot \{\ddot{x}\}^i \quad \text{and} \quad \{x\}^{i+1,k} = \{x\}^i + \Delta t \cdot \{\dot{x}\}^i + \frac{\Delta t^2}{2} \cdot \{\ddot{x}\}^i$$

2 For iteration k :

2.1 Impose displacements $\{x\}^{i+1,k}$ and calculate the contact forces $\{F_c\}^{i+1,k}$ according to contact state.

2.2 According to the equilibrium equation

$$[M]\{\ddot{x} + \Delta\ddot{x}\}^{i+1,k} + [C]\{\dot{x} + \Delta\dot{x}\}^{i+1,k} + [K]\{x + \Delta x\}^{i+1,k} = \{F_c\}^{i+1,k} + \{F_e\}^{i+1,k}$$

we can calculate the unbalanced force:

$$R_{eff}^{i+1,k} = \{F_e\}^{i+1,k} + \{F_c\}^{i+1,k} - [K]\{x\}^{i+1,k} - [C]\{\dot{x}\}^{i+1,k} - [M]\{\ddot{x}\}^{i+1,k}$$

And according to Newmark relation the effective stiffness matrix is obtained as:

$$K_{eff}^{i+1,k} = [K] + \frac{1}{\beta \cdot \Delta t^2} [M] + \frac{\gamma}{\beta \cdot \Delta t} [C]$$

2.3 Calculate the incremental displacement:

$$\{\Delta x\}^{i+1,k} = K_{eff}^{i+1,k} \setminus R_{eff}^{i+1,k}$$

2.4 Check if $\{\Delta x\}^{i+1,k}$ satisfies the tolerance requirement: $\text{norm}(\{\Delta x\}^{i+1,k}) < \text{tol}$:

If yes, stop iterations and set the calculated state variable values as the values for current step and go to next step from 1, $i = i + 1$.

If no, update the displacement, velocity and acceleration as follows

$$\{x\}^{i+1,k+1} = \{x\}^{i+1,k} + p \cdot \{\Delta x\}^{i+1,k}$$

$$\{\dot{x}\}^{i+1,k+1} = \{\dot{x}\}^{i+1,k} + p \cdot \frac{\gamma}{\beta \cdot \Delta t} \{\Delta x\}^{i+1,k}$$

$$\{\ddot{x}\}^{i+1,k+1} = \{\ddot{x}\}^{i+1,k} + p \cdot \frac{1}{\beta \cdot \Delta t^2} \{\Delta x\}^{i+1,k}$$

and go to 2.1, $k = k + 1$. In the formulations p is a penalty number to control computation stability and accelerates the convergence, which is normally set 1 without specifications.

To better demonstrate the process of operating the displacement based iteration scheme, a flow chart is shown in Fig.5.4.

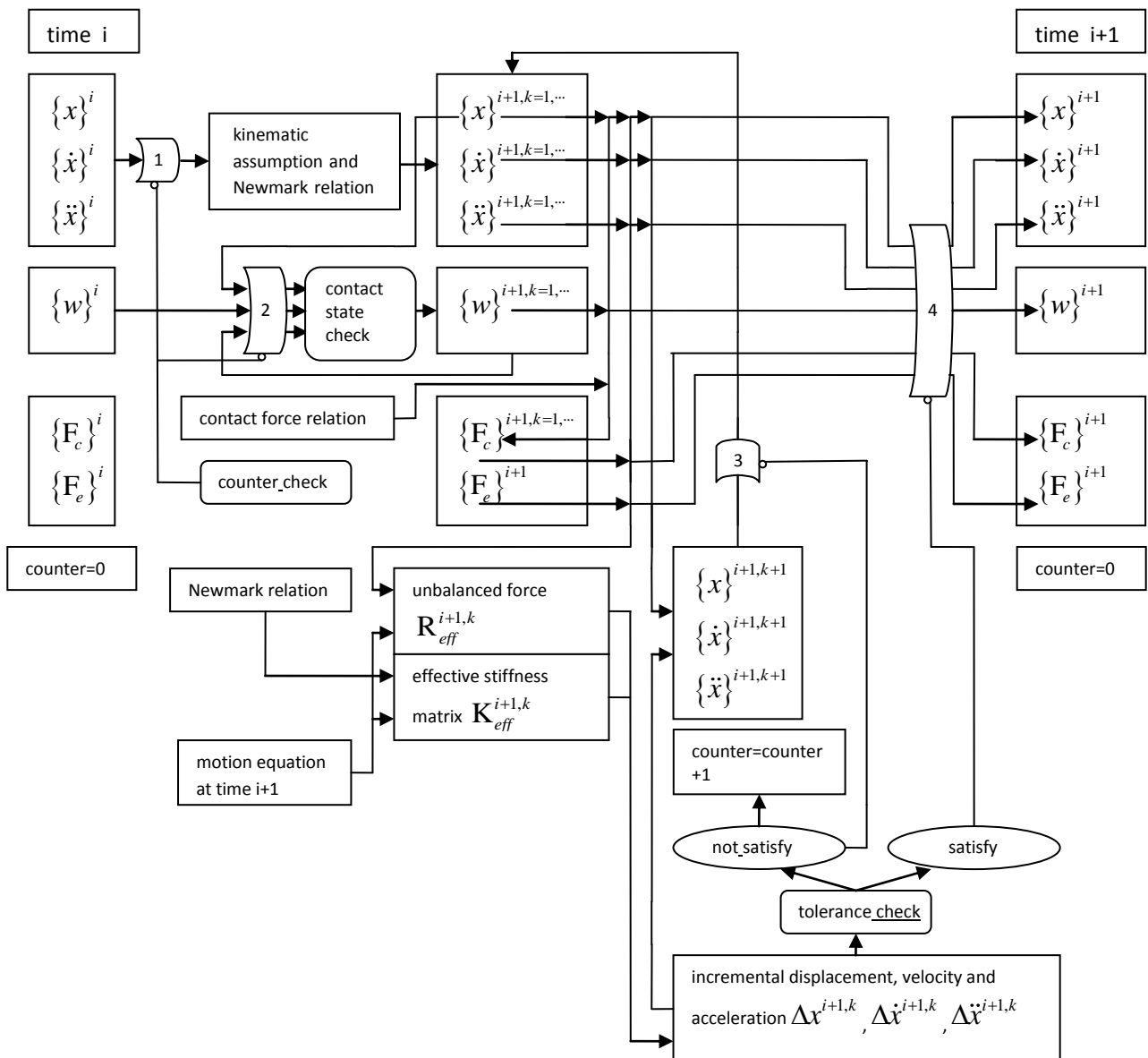


Fig.5.4 Procedure of displacement based iteration with Newmark method

5.3 Contact model description

As discussed in section 5.2, when the numerical procedure is implemented, the contact forces need to be calculated and contact states need to be checked according to the contact model. In this section the contact model which accomplishes the above said task in the simulation is described.

Consider a general 2-D macro contact model with normal and tangential stiffness demonstrated by Fig.5.5. m_1, m_2 represent two bodies in contact; t_1, n_1 are tangential and normal displacement at the contact point on body m_1 ; t_2, n_2 are tangential and normal displacement at the contact point on body m_2 ; T, N are tangential and normal contact forces applied on body m_2 ; k_t, k_n are tangential and normal contact stiffness; s is the slider displacement between the contact pair. The sign definition is shown in the figure.

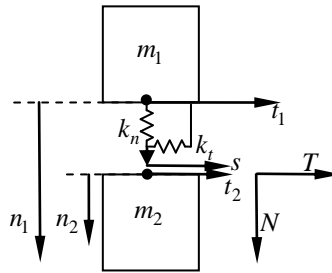


Fig.5.5 General 2-D macro contact model

The relation between the state at current time step and corresponding parameters are listed below(the right superscript 0 means at previous time step, 1 means at current step):

Table 5.1 Contact state and related parameters

parameters state	slider displacement: s	tangential force on m_2 : T	normal force on m_2 : N
stick	$s^{(1)} = s^{(0)} + (t_2^{(1)} - t_2^{(0)})$	$T^{(1)} = k_t \cdot (t_1^{(1)} - s^{(1)})$ $= k_t \cdot (t_1^{(1)} - t_2^{(1)} - (s^{(0)} - t_2^{(0)}))$	$N^{(1)} = k_n \cdot (n_2^{(1)} - n_1^{(1)})$
positive slip	$s^{(1)} = t_1^{(1)} - \frac{\mu N^{(1)}}{k_t}$	$T^{(1)} = \mu \cdot N^{(1)}$	$N^{(1)} = k_n \cdot (n_2^{(1)} - n_1^{(1)})$
negative slip	$s^{(1)} = t_1^{(1)} + \frac{\mu N^{(1)}}{k_t}$	$T^{(1)} = -\mu \cdot N^{(1)}$	$N^{(1)} = k_n \cdot (n_2^{(1)} - n_1^{(1)})$
separation	$s^{(1)} = t_1^{(1)}$	0	0

The procedure to determine contact state and contact forces at current time step follows a Predictor-Corrector method:

1. Assume the current state as stick state.
 Get normal force $N^{(1)} = \max(k_n(n_1^{(1)} - n_2^{(1)}), 0)$.
 Get tangential force $T^{(1)} = k_t(t_1^{(1)} - t_2^{(1)} - s^{*(0)})$.
 Update $s^{*(1)} = s^{*(0)}$.
 If $N^{(1)} > 0$ and $T^{(1)} \geq \mu \cdot N_1$, go to 2.1.
 If $N^{(1)} > 0$ and $T^{(1)} \leq -\mu \cdot N_1$, go to 2.2.
 If $N^{(1)} \leq 0$, go to 2.3.
2. Update according to transition to different states.
 - 2.1 Set $T^{(1)} = \mu \cdot N_1$, update $s^{*(1)} = t_1^{(1)} - t_2^{(1)} - \frac{\mu \cdot N^{(1)}}{k_t}$. (positive slip)
 - 2.2 Set $T^{(1)} = -\mu \cdot N_1$, update $s^{*(1)} = t_1^{(1)} - t_2^{(1)} + \frac{\mu \cdot N^{(1)}}{k_t}$. (negative slip)
 - 2.3 Set $T^{(1)} = 0$, update $s^{*(1)} = t_1^{(1)} - t_2^{(1)}$. (separation)

After these preparations are done, take Den Hartog's analytical solution as benchmark of the numerical simulation. Consider the SDOF in Fig.5.6, which is similar to Den Hartog's system except the addition of tangential contact stiffness and also is a special case of the general contact model described above.

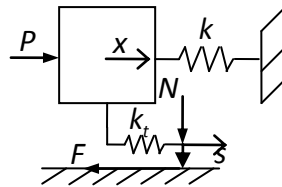


Fig.5.6 SDOF with tangential stiffness

From section 5.1, Fig.5.7 is plotted to demonstrate a response obtained by Den Hartog.

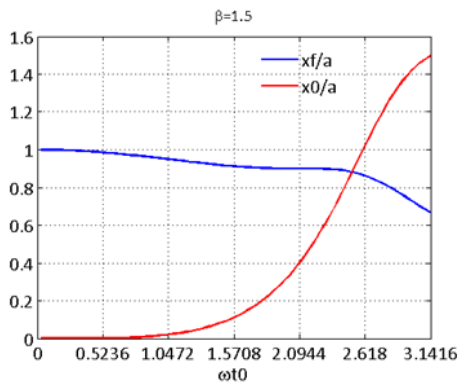


Fig.5.7 Response amplitude variation with t_0

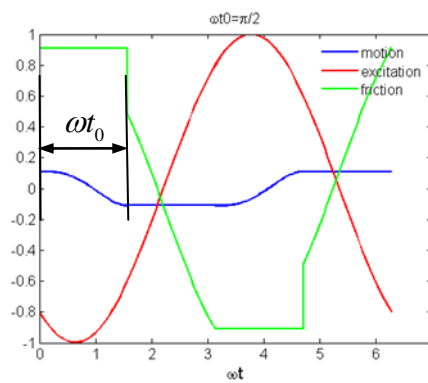


Fig.5.8 Response when $\omega t_0 = \frac{\pi}{2}$

To be compared with Den Hartog's solution, a test case is chosen from Fig.5.7 as following:

$$\beta = \frac{\omega_n}{\omega} = 1.5, \omega t_0 = \frac{\pi}{2}, \text{ and respectively } \frac{x_f}{a} = 0.9119, \frac{x_0}{a} = 0.1109, \varphi = 2.4997$$

The friction force, motion and excitation force are plotted in Fig.5.8. And correspondingly perform the time integration using:

$$P = 1, F = 0.9119, m = 1, k = 1, k_t = 1e5, \omega = (2/3)\omega_n, \Delta t = 1e-4(2\pi/\omega)$$

Fig.5.9 shows the results when steady state cycles are reached.

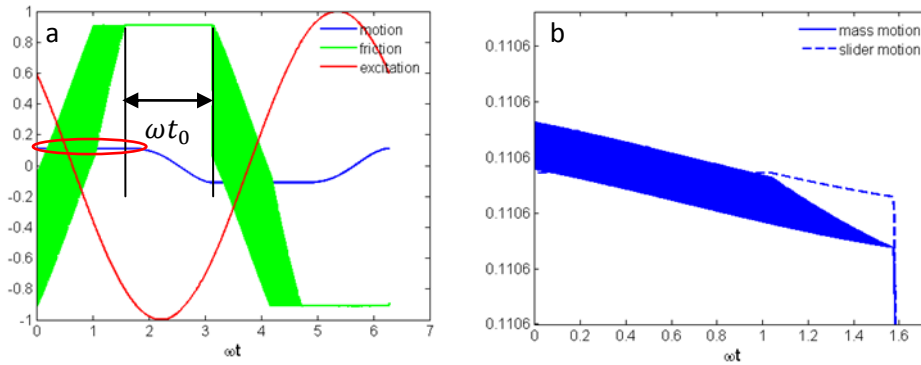


Fig.5.9 Response by DTI (b is a detail from a)

The numerical response amplitude is 0.03% less than the analytical value. The significant difference between this numerical and analytical result is that the mass motion has high frequency interfacial oscillations when the slider stops moving, which is not present when tangential contact stiffness is not considered. This oscillation may be not physical due to local damping factor, [42] discussed the method to eliminate this problem stabilizing the contact force calculation.

It is observed what happens to the response when tangential stiffness is changed. The response in the results table below is convergent to the value analytically obtained by Den Hartog as the stiffness increases. The constants used in the numerical calculation are:

tol=1e-12	$\Delta p=1e-6$	$\Delta t=1e-4 \cdot (2\pi/\omega)$
-----------	-----------------	-------------------------------------

Results:

tangential stiffness (N/m)	1e2	1e3	1e4	1e5	1e6	1e7
response factor (x_0/a)	0.0898	0.1088	0.1106	0.1106	0.1106	0.1106
number of cycles for steady state	20	22	16	16	16	17

In this case, when tangential stiffness reaches $1e4 N/m$, the response is already convergent. This is not true for any case. The convergent speed according to increase of tangential stiffness depends on excitation frequency and friction level. For example, under the condition $\omega/\omega_n = 0.9$ and $F/P = 0.9$, the convergence speed is shown in Fig.5.10, which is much slower than the previous case.

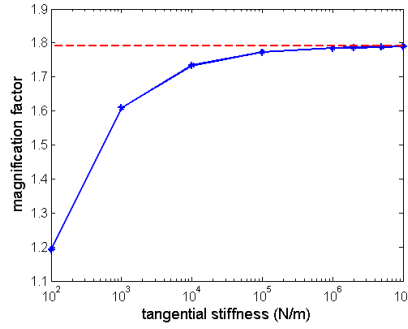


Fig.5.10 Response convergence with tangential stiffness(low speed case)

In reality the contact stiffness between two elastic contact bodies is quite large, like what is obtained from the experiment in Chapter 4, to the level of $10^7 N/m$.

It is also noticed that for this nonlinear motion equation, Newmark method is not unconditionally stable. Take the example shown in Fig.5.8, when the time step increased 10 times longer, which is still much smaller than the excitation period, the calculation diverges immediately within certain tolerance and iteration number limitation. This feature also brings in a problem of contact high frequency oscillation which may not be physically existent. The reason for this problem is not clear at this stage. [44] also reports that unconditional stability of Newmark scheme may be lost in the nonlinear regime.

5.4 Formulation of damper motion in the test rig

The Newmark procedure and contact model are now integrated to simulate the test system demonstrated in Fig.5.11.

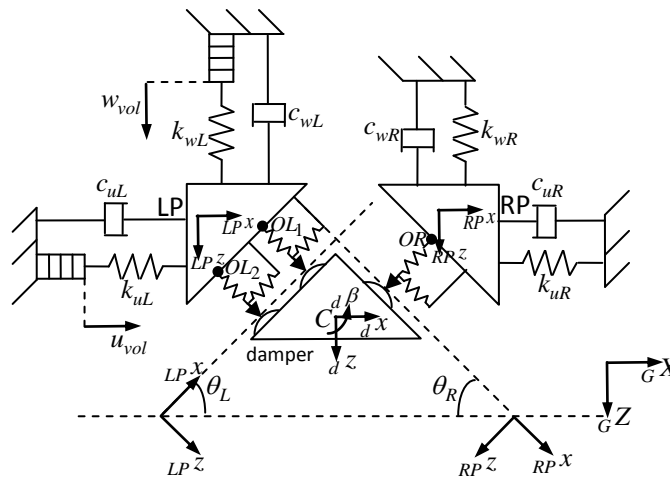


Fig.5.11 Damper-platform system in the test rig

Excitations are given by the piezoelectric actuator displacement u_{vol} and w_{vol} to the left platform. By neglecting the platform rotation, both platforms have 2 degrees of freedom, representing two translational motions. The damper has 3 degrees of freedom including rotation. Take the three-

$$\begin{bmatrix}
\cos \theta_R & -\sin \theta_R & \cos \theta_L & \sin \theta_L & \cos \theta_L & \sin \theta_L \\
\sin \theta_R & \cos \theta_R & -\sin \theta_L & \cos \theta_L & -\sin \theta_L & \cos \theta_L \\
\begin{pmatrix} OR z_d \cdot \cos \theta_R \\ -OR x_d \cdot \sin \theta_R \end{pmatrix} & \begin{pmatrix} -OR z_d \cdot \sin \theta_R \\ -OR x_d \cdot \cos \theta_R \end{pmatrix} & \begin{pmatrix} OL_1 z_d \cdot \cos \theta_L \\ +OL_1 x_d \cdot \sin \theta_L \end{pmatrix} & \begin{pmatrix} OL_1 z_d \cdot \sin \theta_L \\ -OL_1 x_d \cdot \cos \theta_L \end{pmatrix} & \begin{pmatrix} OL_2 z_d \cdot \cos \theta_L \\ +OL_2 x_d \cdot \sin \theta_L \end{pmatrix} & \begin{pmatrix} OL_2 z_d \cdot \sin \theta_L \\ -OL_2 x_d \cdot \cos \theta_L \end{pmatrix}
\end{bmatrix} \begin{Bmatrix} OR^T \\ OR^N \\ OL_1^T \\ OL_1^N \\ OL_2^T \\ OL_2^N \end{Bmatrix} = \begin{bmatrix} m_d & 0 & 0 \\ 0 & m_d & 0 \\ 0 & 0 & I_d \end{bmatrix} \begin{Bmatrix} \ddot{u}_d \\ \ddot{w}_d \\ \ddot{\beta}_d \end{Bmatrix} + \begin{bmatrix} c_{ud} & 0 & 0 \\ 0 & c_{wd} & 0 \\ 0 & 0 & c_{rd} \end{bmatrix} \begin{Bmatrix} \dot{u}_d \\ \dot{w}_d \\ \dot{\beta}_d \end{Bmatrix} + \begin{bmatrix} k_{ud} & 0 & 0 \\ 0 & k_{wd} & 0 \\ 0 & 0 & k_{rd} \end{bmatrix} \begin{Bmatrix} u_d \\ w_d \\ \beta_d \end{Bmatrix} - \begin{Bmatrix} 0 \\ c F_Z \\ -\delta x \cdot c F_Z \end{Bmatrix} \quad (13)$$

Express the left platform equilibrium in matrix form:

$$m_{LP} \ddot{u}_{LP} = \sum F_X = OL_1^* F_X + OL_2^* F_X + k_{uL}(u_{vol} - u_{LP}) - c_{uL} \dot{u}_{LP}$$

$$m_{LP} \ddot{w}_{LP} = \sum F_Z = OL_1^* F_Z + OL_2^* F_Z + k_{wL}(w_{vol} - w_{LP}) - c_{wL} \dot{w}_{LP}$$

$$OL_1^* F_X = -OL_1 F_X, \quad OL_1^* F_Z = -OL_1 F_Z, \quad OL_2^* F_X = -OL_2 F_X, \quad OL_2^* F_Z = -OL_2 F_Z$$

$$\begin{bmatrix} -GLP A & -GLP A \end{bmatrix} \begin{Bmatrix} OL_1^T \\ OL_1^N \\ OL_2^T \\ OL_2^N \end{Bmatrix} + \begin{Bmatrix} k_{uL} \cdot u_{vol} \\ k_{wL} \cdot w_{vol} \end{Bmatrix} = \begin{bmatrix} m_{uL} & 0 \\ 0 & m_{wL} \end{bmatrix} \begin{Bmatrix} \ddot{u}_{LP} \\ \ddot{w}_{LP} \end{Bmatrix} + \begin{bmatrix} k_{uL} & 0 \\ 0 & k_{wL} \end{bmatrix} \begin{Bmatrix} u_{LP} \\ w_{LP} \end{Bmatrix} + \begin{bmatrix} c_{uL} & 0 \\ 0 & c_{wL} \end{bmatrix} \begin{Bmatrix} \dot{u}_{LP} \\ \dot{w}_{LP} \end{Bmatrix} \quad (14)$$

Express the right platform equilibrium in matrix form:

$$m_{RP} \ddot{u}_{RP} = \sum F_X = OR^* F_X - k_{uR} u_{RP} - c_{uR} \dot{u}_{RP}$$

$$m_{RP} \ddot{w}_{RP} = \sum F_Z = OR^* F_Z - k_{wR} w_{RP} - c_{wR} \dot{w}_{RP}$$

$$OR^* F_X = -OR F_X, \quad OR^* F_Z = -OR F_Z$$

$$-GRP A \begin{Bmatrix} OR^T \\ OR^N \end{Bmatrix} = \begin{bmatrix} m_{uR} & 0 \\ 0 & m_{wR} \end{bmatrix} \begin{Bmatrix} \ddot{u}_{RP} \\ \ddot{w}_{RP} \end{Bmatrix} + \begin{bmatrix} k_{uR} & 0 \\ 0 & k_{wR} \end{bmatrix} \begin{Bmatrix} u_{RP} \\ w_{RP} \end{Bmatrix} + \begin{bmatrix} c_{uR} & 0 \\ 0 & c_{wR} \end{bmatrix} \begin{Bmatrix} \dot{u}_{RP} \\ \dot{w}_{RP} \end{Bmatrix} \quad (15)$$

Total equilibrium is obtained:

$$B \times F_{contact} + F_{external} = M \times \ddot{U} + K \times U + C \times \dot{U} \quad (16)$$

$$B = \begin{bmatrix}
RPG A & LPG A & LPG A \\
\begin{bmatrix} OR z_d & -OR x_d \end{bmatrix}^{GRP A} & \begin{bmatrix} OL_1 z_d & -OL_1 x_d \end{bmatrix}^{GLP A} & \begin{bmatrix} OL_2 z_d & -OL_2 x_d \end{bmatrix}^{GLP A} \\
\begin{bmatrix} 0 \end{bmatrix}_{2 \times 2} & -LPG A & -LPG A \\
-RPG A & \begin{bmatrix} 0 \end{bmatrix}_{2 \times 2} & \begin{bmatrix} 0 \end{bmatrix}_{2 \times 2}
\end{bmatrix}_{7 \times 6}$$

$$= \begin{bmatrix} \cos \theta_R & -\sin \theta_R & \cos \theta_L & \sin \theta_L & \cos \theta_L & \sin \theta_L \\ \sin \theta_R & \sin \theta_R & -\sin \theta_L & \cos \theta_L & -\sin \theta_L & \cos \theta_L \\ \begin{pmatrix} OR z_d \cdot \cos \theta_R \\ -OR x_d \cdot \sin \theta_R \end{pmatrix} & \begin{pmatrix} -OR z_d \cdot \sin \theta_R \\ -OR x_d \cdot \cos \theta_R \end{pmatrix} & \begin{pmatrix} OL_1 z_d \cdot \cos \theta_L \\ +OL_1 x_d \cdot \sin \theta_L \end{pmatrix} & \begin{pmatrix} OL_1 z_d \cdot \sin \theta_L \\ -OL_1 x_d \cdot \cos \theta_L \end{pmatrix} & \begin{pmatrix} OL_2 z_d \cdot \cos \theta_L \\ +OL_2 x_d \cdot \sin \theta_L \end{pmatrix} & \begin{pmatrix} OL_2 z_d \cdot \sin \theta_L \\ -OL_2 x_d \cdot \cos \theta_L \end{pmatrix} \\ 0 & 0 & -\cos \theta_L & -\sin \theta_L & -\cos \theta_L & -\sin \theta_L \\ 0 & 0 & \sin \theta_L & -\cos \theta_L & \sin \theta_L & -\cos \theta_L \\ -\cos \theta_R & \sin \theta_R & 0 & 0 & 0 & 0 \\ -\sin \theta_R & \cos \theta_R & 0 & 0 & 0 & 0 \end{bmatrix}$$

$$U = \begin{Bmatrix} u_d \\ w_d \\ \beta_d \\ u_{PL} \\ w_{PL} \\ u_{PR} \\ w_{PR} \end{Bmatrix}, F_{contact} = \begin{Bmatrix} OR^T \\ OR^N \\ OL_1^T \\ OL_1^N \\ OL_2^T \\ OL_2^N \end{Bmatrix}, F_{external} = \begin{Bmatrix} 0 \\ {}_C F_Z \\ -\delta x \cdot {}_C F_Z \\ k_{uL} \cdot u_{vol} \\ k_{wL} \cdot w_{vol} \\ 0 \\ 0 \end{Bmatrix}, M = \begin{bmatrix} m_d & 0 & 0 & 0 & 0 & 0 & 0 \\ 0 & m_d & 0 & 0 & 0 & 0 & 0 \\ 0 & 0 & I_d & 0 & 0 & 0 & 0 \\ 0 & 0 & 0 & m_{LP} & 0 & 0 & 0 \\ 0 & 0 & 0 & 0 & m_{LP} & 0 & 0 \\ 0 & 0 & 0 & 0 & 0 & m_{RP} & 0 \\ 0 & 0 & 0 & 0 & 0 & 0 & m_{RP} \end{bmatrix}$$

$$C = \begin{bmatrix} c_{ud} & 0 & 0 & 0 & 0 & 0 & 0 \\ 0 & c_{wd} & 0 & 0 & 0 & 0 & 0 \\ 0 & 0 & c_{rd} & 0 & 0 & 0 & 0 \\ 0 & 0 & 0 & c_{uL} & 0 & 0 & 0 \\ 0 & 0 & 0 & 0 & c_{wL} & 0 & 0 \\ 0 & 0 & 0 & 0 & 0 & c_{uR} & 0 \\ 0 & 0 & 0 & 0 & 0 & 0 & c_{wR} \end{bmatrix}, K = \begin{bmatrix} k_{ud} & 0 & 0 & 0 & 0 & 0 & 0 \\ 0 & k_{wd} & 0 & 0 & 0 & 0 & 0 \\ 0 & 0 & k_{rd} & 0 & 0 & 0 & 0 \\ 0 & 0 & 0 & k_{uL} & 0 & 0 & 0 \\ 0 & 0 & 0 & 0 & k_{wL} & 0 & 0 \\ 0 & 0 & 0 & 0 & 0 & k_{uR} & 0 \\ 0 & 0 & 0 & 0 & 0 & 0 & k_{wR} \end{bmatrix}$$

Here k_{ud} , k_{wd} , k_{rd} is respectively the stiffness of horizontal, vertical and rotational spring connected between damper and ground, which are not shown in Fig.5.11. They are put in the equations with potential function of making integrations convergent. In reality k_{ud} , k_{wd} and k_{rd} do not exist because the damper is free. c_{ud} , c_{wd} , c_{rd} is equivalent viscous damping factor of the viscous element connected to the damper. Not only for numerical convergence, but also from physical point of view, c_{ud} , c_{wd} , c_{rd} are necessary parameters in the simulation.

Since there is manufacturing uncertainties, δx is the distance between dead weight application line and damper real mass center.

Kinematic relations are built up as following.

For instant velocities, we have:

$${}^{ORC}D = \begin{bmatrix} 1 & 0 & {}^{OR}z_d \\ 0 & 1 & -{}^{OR}x_d \end{bmatrix}, \quad {}^{OL_1C}D = \begin{bmatrix} 1 & 0 & {}^{OL_1}z_d \\ 0 & 1 & -{}^{OL_1}x_d \end{bmatrix}, \quad {}^{OL_2C}D = \begin{bmatrix} 1 & 0 & {}^{OL_2}z_d \\ 0 & 1 & -{}^{OL_2}x_d \end{bmatrix}, \quad {}^G\dot{u} = \begin{Bmatrix} {}^G\dot{u} \\ {}^G\dot{w} \\ {}^{OL_1}\dot{u} \\ {}^{OL_1}\dot{w} \\ {}^{OL_2}\dot{u} \\ {}^{OL_2}\dot{w} \end{Bmatrix} = \begin{bmatrix} {}^{ORC}D \\ {}^{OL_1C}D \\ {}^{OL_2C}D \end{bmatrix} \begin{Bmatrix} \dot{u}_d \\ \dot{w}_d \\ \dot{\beta}_d \end{Bmatrix}$$

$${}^P\dot{u} = \begin{Bmatrix} {}^{RP}\dot{t} \\ {}^{OR}\dot{t} \\ {}^{RP}\dot{n} \\ {}^{LP}\dot{t} \\ {}^{OL_1}\dot{t} \\ {}^{LP}\dot{n} \\ {}^{OL_1}\dot{n} \\ {}^{LP}\dot{t} \\ {}^{OL_2}\dot{t} \\ {}^{LP}\dot{n} \\ {}^{OL_2}\dot{n} \end{Bmatrix} = \begin{bmatrix} {}^{RPG}A & [0]_{2 \times 2} & [0]_{2 \times 2} \\ [0]_{2 \times 2} & {}^{LPG}A & [0]_{2 \times 2} \\ [0]_{2 \times 2} & [0]_{2 \times 2} & {}^{LPG}A \end{bmatrix} {}^G\dot{u} = \begin{bmatrix} {}^{RPG}A & [0]_{2 \times 2} & [0]_{2 \times 2} \\ [0]_{2 \times 2} & {}^{LPG}A & [0]_{2 \times 2} \\ [0]_{2 \times 2} & [0]_{2 \times 2} & {}^{LPG}A \end{bmatrix} \begin{bmatrix} {}^{ORC}D \\ {}^{OL_1C}D \\ {}^{OL_2C}D \end{bmatrix} \begin{Bmatrix} \dot{u}_d \\ \dot{w}_d \\ \dot{\beta}_d \end{Bmatrix} = \begin{bmatrix} {}^{RPG}A & {}^{ORC}D \\ {}^{LPG}A & {}^{OL_1C}D \\ {}^{LPG}A & {}^{OL_2C}D \end{bmatrix} \begin{Bmatrix} \dot{u}_d \\ \dot{w}_d \\ \dot{\beta}_d \end{Bmatrix}$$

$${}^P\dot{u} = E_1 \begin{Bmatrix} \dot{u}_d \\ \dot{w}_d \\ \dot{\beta}_d \end{Bmatrix}, \quad E_1 = \begin{bmatrix} \cos \theta_R & \sin \theta_R & \begin{pmatrix} {}^{OR}z_d \cdot \cos \theta_R \\ -{}^{OR}x_d \cdot \sin \theta_R \end{pmatrix} \\ -\sin \theta_R & \cos \theta_R & \begin{pmatrix} -{}^{OR}z_d \cdot \sin \theta_R \\ -{}^{OR}x_d \cdot \cos \theta_R \end{pmatrix} \\ \cos \theta_L & -\sin \theta_L & \begin{pmatrix} {}^{OL_1}z_d \cdot \cos \theta_L \\ +{}^{OL_1}x_d \cdot \sin \theta_L \end{pmatrix} \\ \sin \theta_L & \cos \theta_L & \begin{pmatrix} {}^{OL_1}z_d \cdot \sin \theta_L \\ -{}^{OL_1}x_d \cdot \cos \theta_L \end{pmatrix} \\ \cos \theta_L & -\sin \theta_L & \begin{pmatrix} {}^{OL_1}z_d \cdot \cos \theta_L \\ +{}^{OL_1}x_d \cdot \sin \theta_L \end{pmatrix} \\ \sin \theta_L & \cos \theta_L & \begin{pmatrix} {}^{OL_1}z_d \cdot \sin \theta_L \\ -{}^{OL_1}x_d \cdot \cos \theta_L \end{pmatrix} \end{bmatrix}$$

If the variations of positions of contact points in the local damper coordinate system are small quantities relative to the distance between contact point and mass center, the position can be regarded as constant during the motion.

By integrating with time, we can have the relation of displacements as:

$${}^P u = E_1 \begin{Bmatrix} u_d \\ w_d \\ \beta_d \end{Bmatrix} \quad (17)$$

Similarly, for left platform mass center and contact points, and for right platform mass center and contact points we have:

$${}^{LP}u^* = \begin{Bmatrix} {}^{LP} \\ {}^{OL_1^*}t \\ {}^{LP} \\ {}^{OL_1^*}n \\ {}^{LP} \\ {}^{OL_2^*}t \\ {}^{LP} \\ {}^{OL_2^*}n \end{Bmatrix} = E_2 \begin{Bmatrix} u_{LP} \\ w_{LP} \end{Bmatrix}, \quad E_2 = \begin{bmatrix} {}^{LPG}A \\ {}^{LPG}A \end{bmatrix} \quad (18)$$

$${}^{RP}u^* = \begin{Bmatrix} {}^{RP} \\ {}^{OR^*}t \\ {}^{RP} \\ {}^{OR^*}t \end{Bmatrix} = E_3 \begin{Bmatrix} u_{RP} \\ w_{RP} \end{Bmatrix}, \quad E_3 = {}^{RPG}A \quad (19)$$

After the system equilibrium and kinematic relations are built up, a numerical program is worked out to combine the integration method, contact model and system parameters to simulate the experimental outcome.

It should be noted that to start the numerical calculation, the initial conditions of the system should be determined. Equation (16) can be changed to static equilibrium expression by eliminating the inertial and damping forces, that is:

$$B \times F_{contact} + F_{external} = K \times U \quad (20)$$

When $F_{contact}$ is expressed by the function of contact stiffness, there exist different solutions due to the nonlinearity of friction force, which means the initial conditions can be not unique.

5.5 Simulation results of out-of-phase motion for three-point damper

The detailed mass, stiffness and damping distribution are not known from the test rig. But the values of these parameters do not influence the damper response when the excitation frequency is low. For all the following simulations, the common values assigned are:

$$m_{LP} = m_{RP} = 0.2\text{kg}, \quad c_{uL} = c_{uR} = c_{wL} = c_{wR} = 80\text{kg/s}$$

$$m_d = 0.02\text{kg}, \quad I_d = 2.18 \times 10^{-7}\text{kg} \cdot \text{m}^2$$

5.5.1 Steady state response and comparison with experimental results

First the contact tangential stiffness used in the simulation can be obtained from equation (10) in Chapter 4 and Fig.4.4.1, about $13 \times 56 / 45 \approx 16\text{N}/\mu\text{m}$.

Consider the experimental example shown in Fig.4.12 when a 'shoe' shape hysteresis happens. Assign $\mu_R = 0.39$, $\mu_{L1} = \mu_{L2} = 0.22$, which are rough friction coefficient values from Fig.4.12.2. Other parameters are the same with experiment. When the initial conditions are set as ${}^{OR}T = 0$, ${}^{OL1}T = 0$, ${}^{OL2}T = 0$, the numerical steady state response is as follows in Fig.5.12.

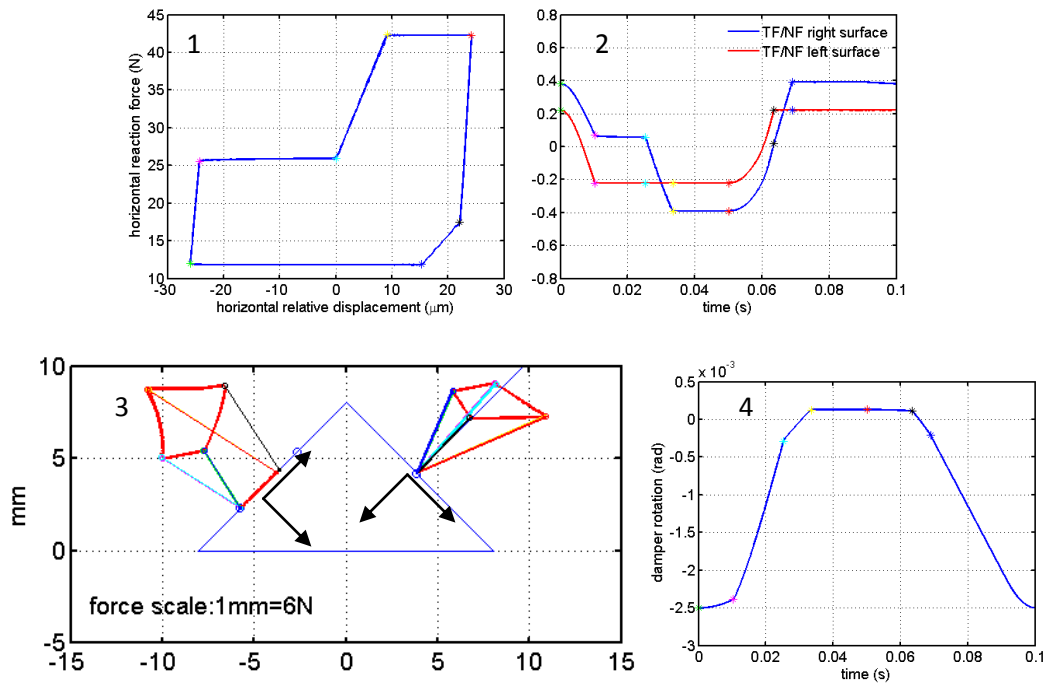


Fig.5.12 Case of simulation of hysteresis, force distribution and rotation

In general, this simulation result is consistent with the experimental outcome except local micro stick slip phenomenon. The details on each contact pair is plotted in Fig.5.13.

From subplot 1, 2, 3 of Fig.5.13, the energy dissipated at each contact pair is known. Subplot 4, 5, 6 demonstrate the relative motion between platform contact point and damper contact point. When the relative displacement between platform slider and damper contact point (denoted as δs) is equal to the relative displacement between platform contact point and damper contact point (denoted as δc), the contact pair loses contact. When δs keeps constant, the contact pair is in stick condition. When δs is changing, the contact pair is in slip condition.

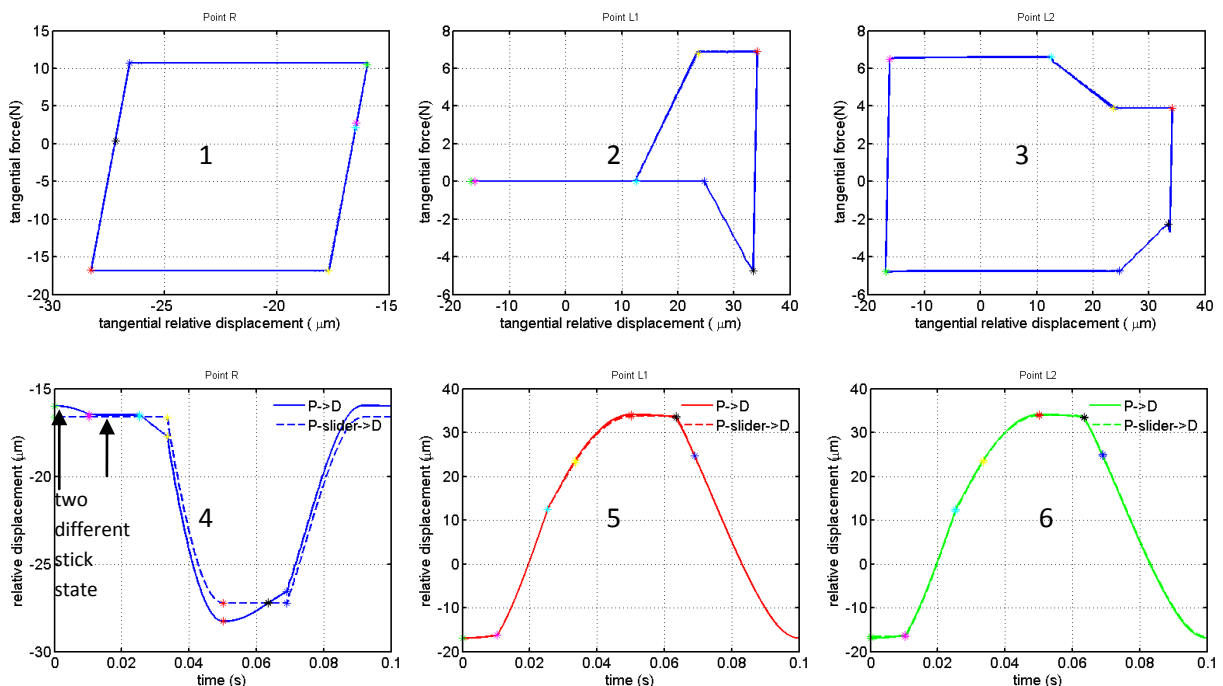


Fig.5.13 Hysteresis and relative movement at each contact pair

Consider the definition of friction coefficient, when the proportion between tangential force(TF) and normal force(NF) reaches one limit, the contact surface will slip. Fig.5.14 gives the details of proportion TF/NF for left two contact points.

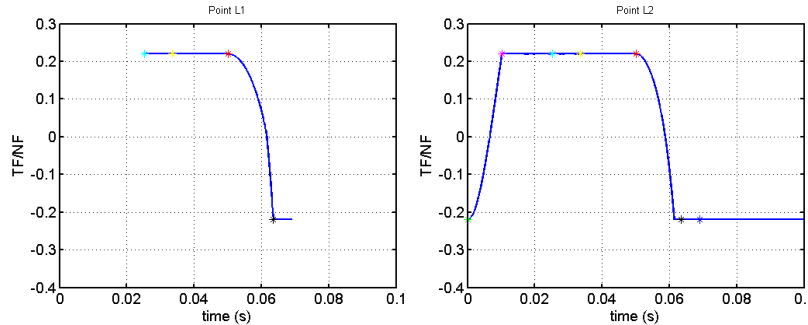


Fig.5.14 Proportion between tangential and normal contact force of left surface contacts

With the help of Fig.5.13 and Fig.5.14, each stage in one cycle is demonstrated:

- (1) From labeled green to pink point, contact point OR^* moves up relative to OR in stick state; contact point OL_1^* loses contact with OL_1 ; contact point OL_2^* moves up relative to OL_2 in stick state. Damper rotation is small.
- (2) From pink to cyan point, OR^* keeps a constant position relative to OR^* in stick state; OL_1^* loses contact with OL_1 ; OL_2^* slips up relative to OL_2 . Damper rotation is large. Point OR^* in this stage is like a pivot axis.
- (3) From cyan to yellow point, OR^* moves up relative to OR in stick state; OL_1^* begins having contact with OL_1 and slips up relative to OL_1 ; OL_2^* slips up relative to OL_2 . Damper rotation is small.
- (4) From yellow to red point, OR^* slips up relative to OR ; OL_1^* slips up relative to OL_1 ; OL_2^* slips up relative to OL_2 . There is no damper rotation.
- (5) From red to black point, OR^* moves down relative to OR in stick state; OL_1^* moves down relative to OL_1 in stick state; OL_2^* moves down relative to OL_2 in stick state. There is no damper rotation.
- (6) From black to blue point, OR^* moves down relative to OR in stick state; OL_1^* slips down relative to OL_1 and begin losing contact with OL_1 ; OL_2^* slips down relative to OL_2 . Damper rotation is small.
- (7) From blue to green point, OR^* slips down relative to OR ; OL_1^* loses contact with OL_1 ; OL_2^* slips down relative to OL_2 . Damper rotation is large.

If we check the slope of the hysteresis line which represents a dual-stick state, the value when fitted is 12.80 from this example shown in Fig.5.15, which is in accordance with the theory developed in chapter 4, based on the values assigned to normal and tangential stiffness in the simulation.

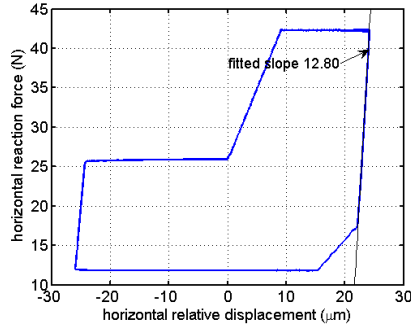


Fig.5.15

5.5.2 Solution from different initial conditions

In the previous section, the initial conditions are set as $OR^T = 0$, $OL1^T = 0$, $OL2^T = 0$. When the initial conditions are changed, it is necessary to check whether the steady state response is influenced.

Set static friction coefficient as $\mu_{RS} = 0.5$, $\mu_{L1s} = 0.5$, $\mu_{L2s} = 0.5$.

Four possible initial conditions are calculated:

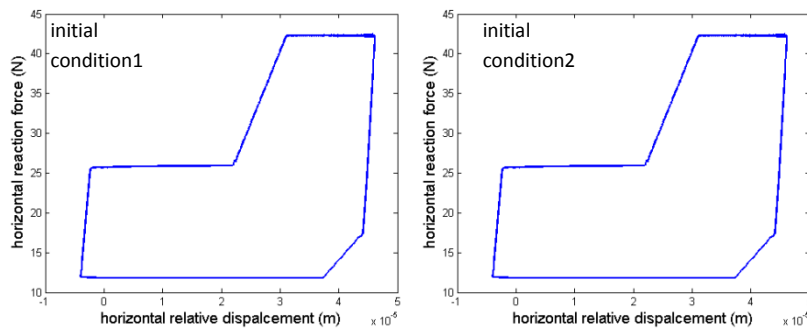
Initial conditions 1 $OR^T = 0$, $OL1^T = 0$, $OL2^T = 0$

Initial conditions 2 $OR^T = \mu_{RS}ORN$, $OL1^T = -\mu_{L1s}OL1N$, $OL2^T = -\mu_{L2s}OL2N$

Initial conditions 3 $OR^T = -\mu_{RS}ORN$, $OL1^T = \mu_{L1s}OL1N$, $OL2^T = \mu_{L2s}OL2N$

Initial conditions 4 $OR^T = \mu_{RS}ORN$, $OL1^T = 0$, $OL2^T = -\mu_{L2s}OL2N$

The steady state response(the 20th cycle from each simulation) shown in Fig.5.16 implies that the solution for these initial conditions is unique.



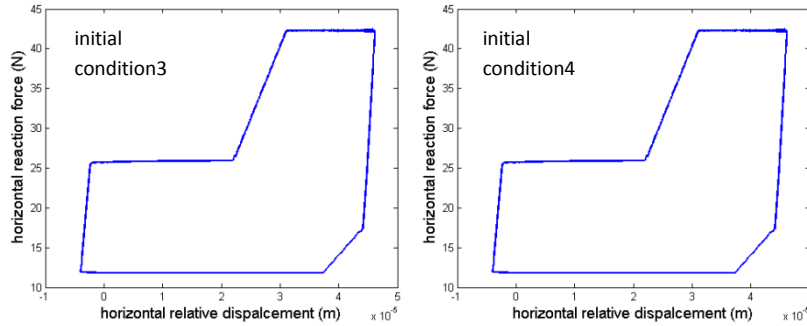


Fig.5.16 Steady state response from 4 different initial conditions

At this stage it is not clear whether the steady state response is always unique for different initial conditions.

5.5.3 Influence of excitation frequency and test rig stiffness

In practice, the under-platform damper works in high frequency range, which beyond the ability of current test rig due to its flexibility. It is useful to implement high frequency excitation in the simulation to check how the damper behavior is changed with frequency.

Under the same other conditions of example in 5.4.1, three frequencies are used: 10Hz, 40Hz and 100Hz.

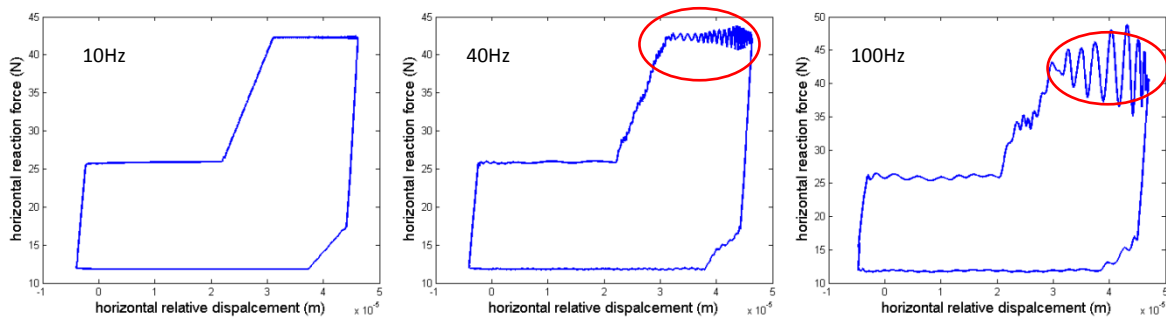


Fig.5.17 Steady state response under excitation of different frequencies

The basic hysteresis features are similar for the three frequencies, but the part labeled by red ellipse has quite large high frequency interfacial oscillations due to contact stiffness, which is critical for the simulation. Improvements shall be found to solve this problem.

Ideally, when the parts that impose motion and measure force are infinitely stiff, the damper behavior under certain excitation is only determined by its own parameters such as mass, geometry and the contact parameters. Due to the flexibility of the test rig, there is some external influence to damper dynamics. In simulation the mass of platforms can be reduced and the stiffness related to platforms can be increased to reduce the external influence. In Fig.5.18, one case with 100 times higher test rig stiffness is simulated with the conditions adopted in the example in section 5.4.1.

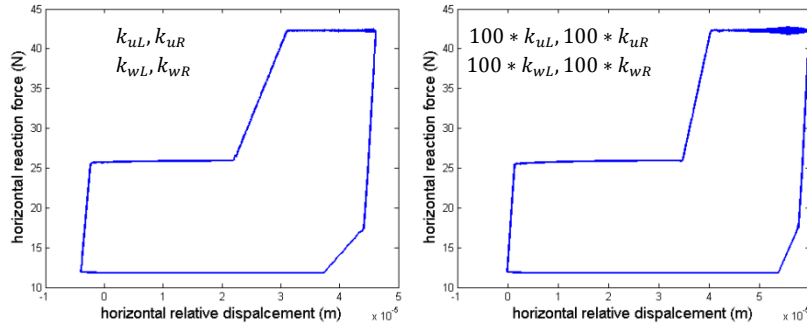


Fig.5.18 Steady state response with different test rig stiffness

The result shows the compliance of current test rig is not critical to disturb the measurement of damper behavior(still in the simulation interfacial high frequency oscillations exist).

5.5.4 Response sensitivity to friction coefficient

From the hysteresis measurement, typically as demonstrated in Fig.4.6, the hysteresis evolution is significant. From the measurement of transmitted force, the parameter which changes according to the evolution is the proportion limit between tangential and normal contact surface, namely friction coefficient. The response sensitivity is checked under the same other conditions with different groups of friction coefficients. Fig.5.19.a-b are the hysteresis given by the damper.

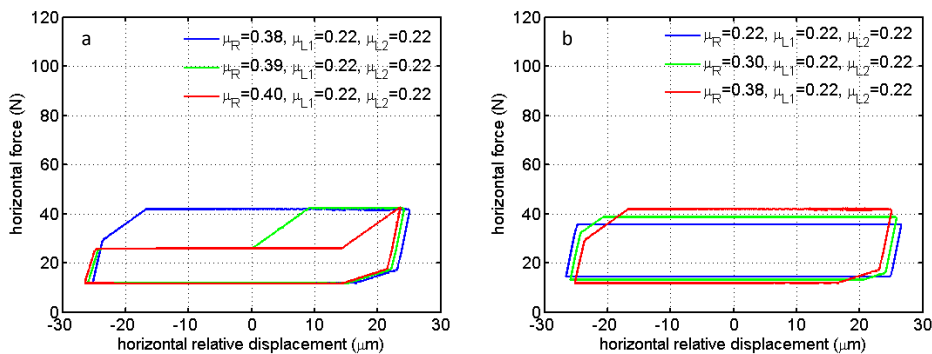


Fig.5.19 Steady state response sensitivity to friction coefficient variation

As shown in Fig.5.19, different ‘shoe’ shapes in the experiment can be obtained in the simulation by changing the values of friction coefficient. Fig.5.19-a is the synthetic demonstration of a solution region which is very sensitive to the change of respective friction coefficients and Fig.5.19-b is the synthetic demonstration of a solution region which is not so sensitive to the friction coefficient variations. This phenomenon may explain the complex uncertain behavior of under-platform damper from one aspect.

5.6 Simulation results of in-phase motion for three-point damper

5.6.1 Steady state response and comparison with experimental results

Two examples under the following conditions are shown in Fig.5.20 and Fig.5.21 comparing hysteresis, force distribution and damper rotation.

motion type	nominal amplitude	excitation frequency	dead weight
in-phase	60 μm	5Hz	4.65kg

The friction coefficients used in the simulation are set according to Fig.4.31b and Fig.4.32b respectively as:

$$\mu_R = 0.15, \mu_{L1} = 0.15, \mu_{L2} = 0.15 \text{ (example 1)}$$

$$\mu_R = 0.42, \mu_{L1} = 0.22, \mu_{L2} = 0.32 \text{ (example 2)}$$

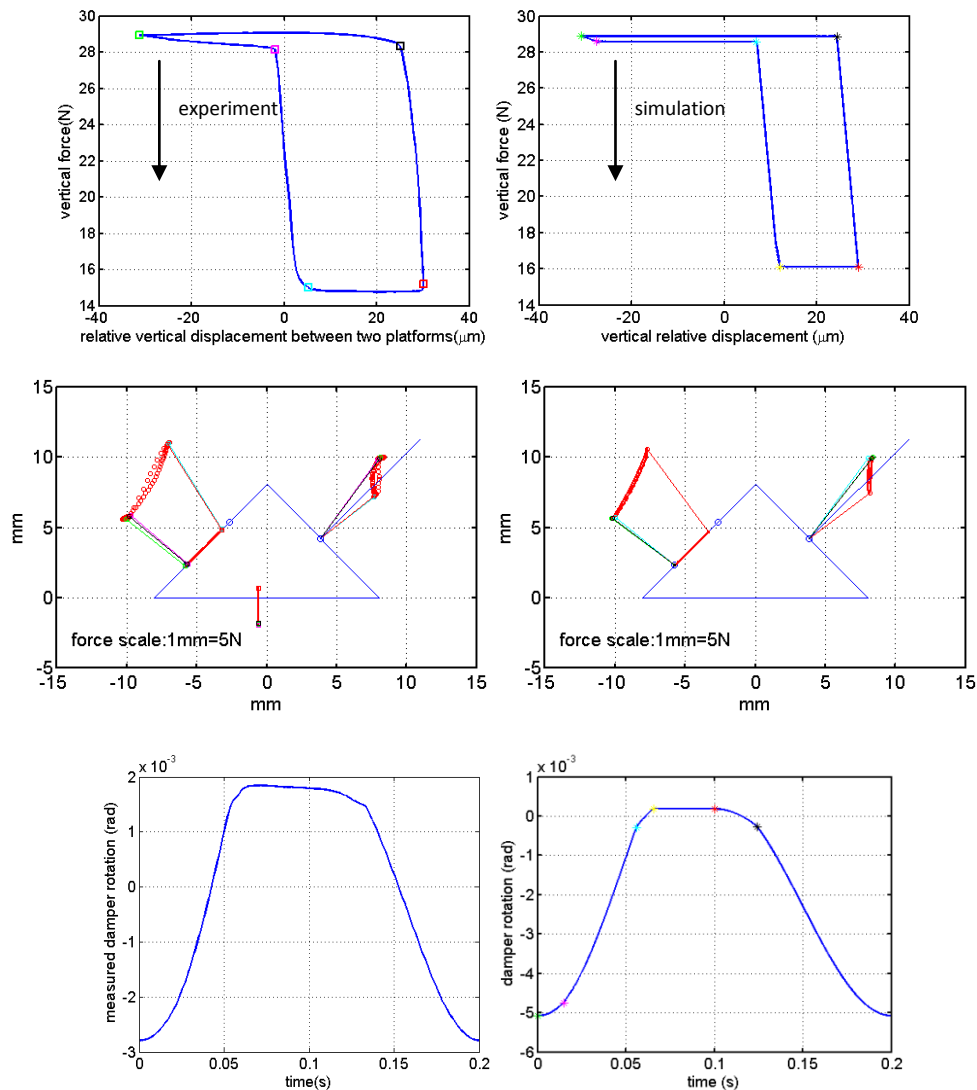


Fig.5.20 Comparison demonstration example 1

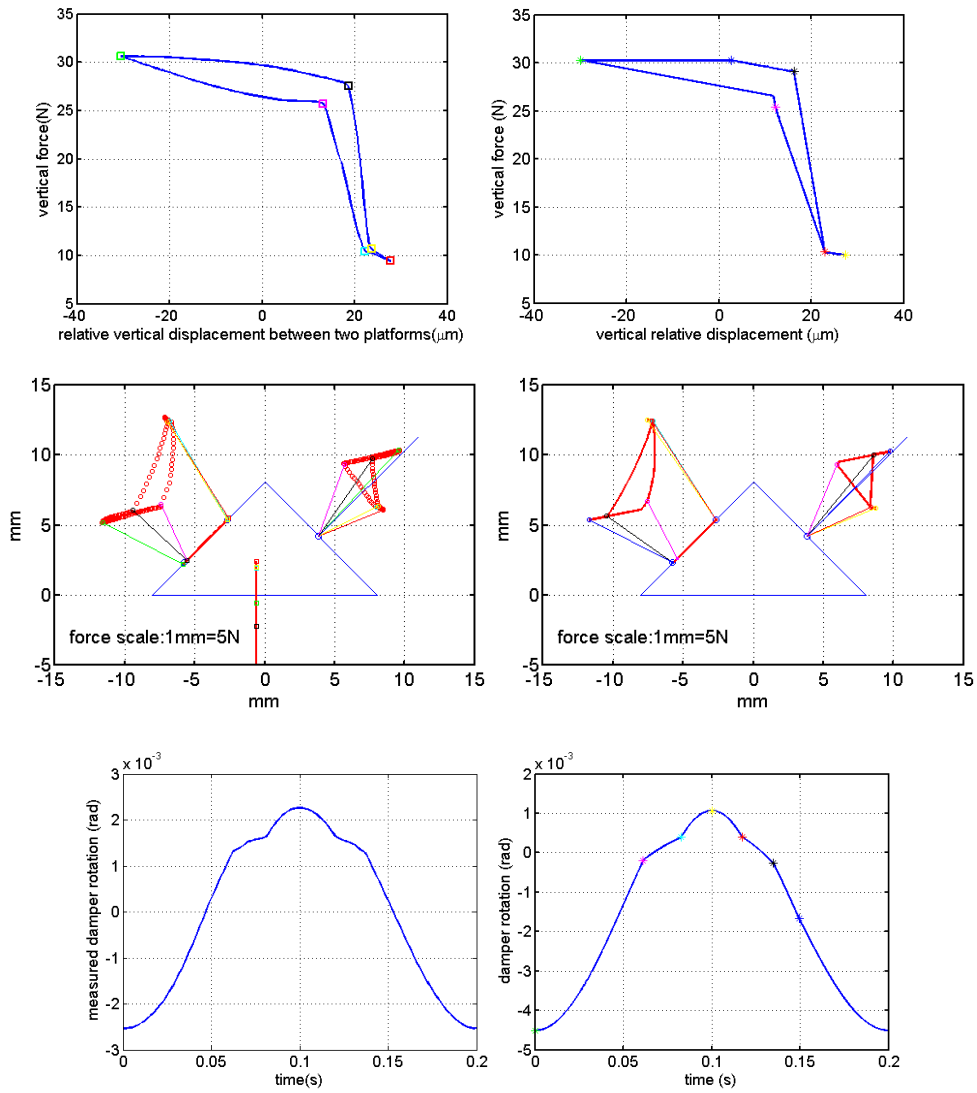


Fig.5.21 Comparison demonstration example 2

There is good consistency between experiment and simulation. For example 2, the local hysteresis are shown in Fig.5.22.

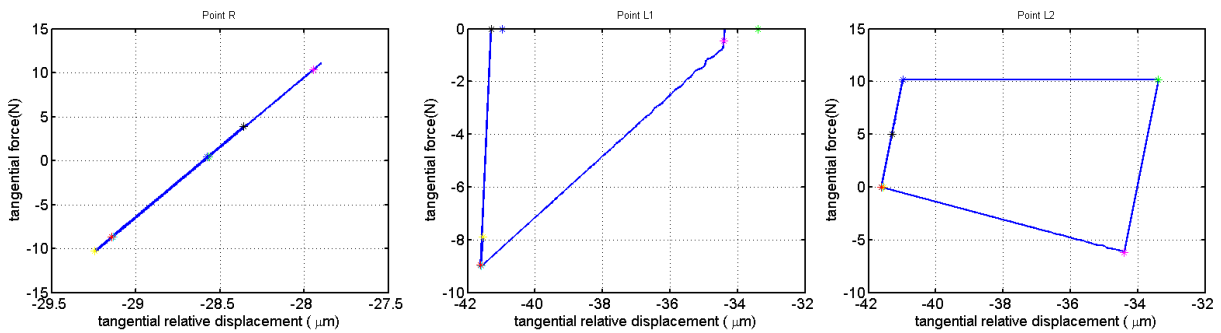


Fig.5.22 Comparison demonstration example 2

Denote the total hysteresis area as A_{total} , the area of local hysteresis is A_R , A_{L1} , A_{L2} respectively, it is found:

$$A_{total}(135.67) \approx A_R(0.09) + A_{L1}(33.43) + A_{L2}(100.36)$$

The details on each contact pair of the simulation of example 2 are demonstrated in Fig.5.23.

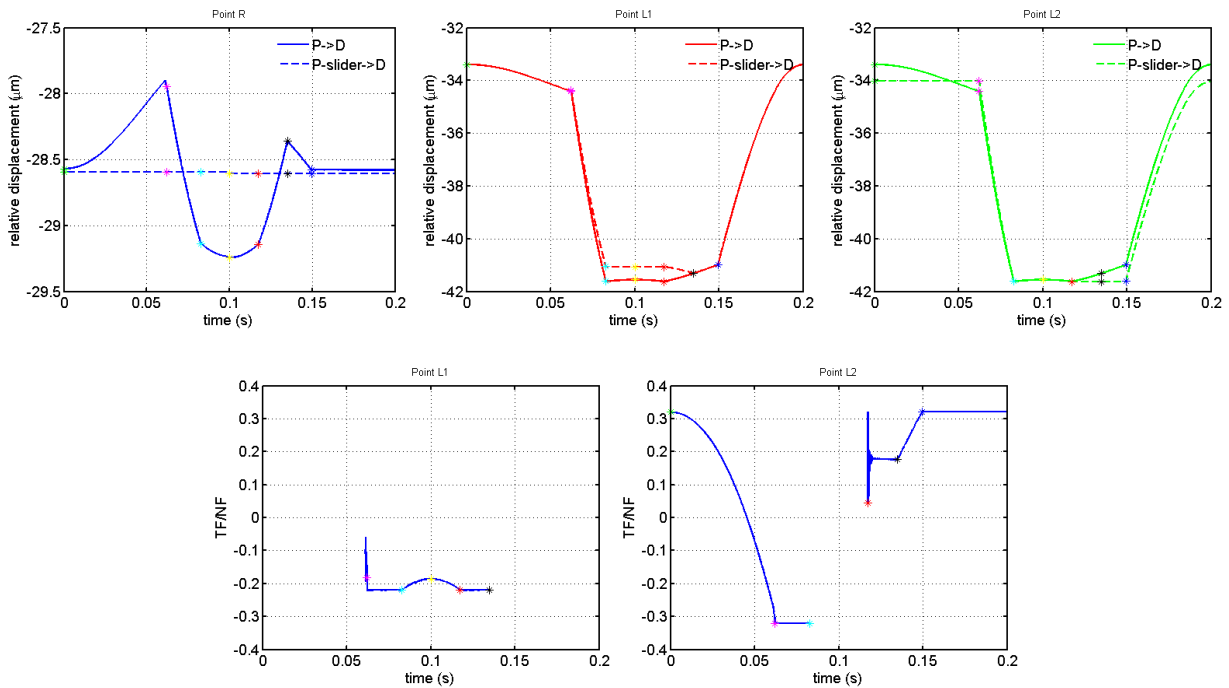
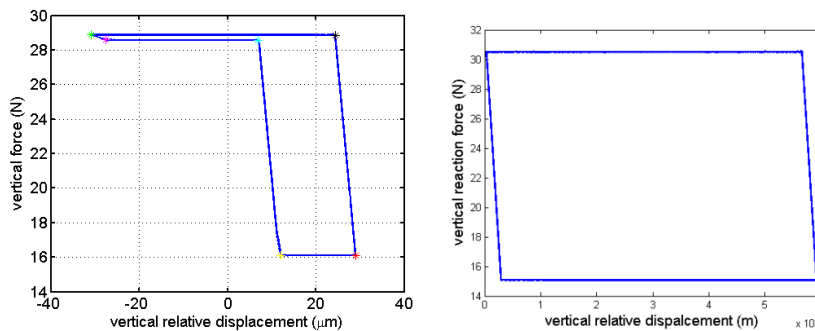


Fig.5.23 Details on contact pair in simulation of example 2

It is clear from Fig.5.23 that both of left contact pair lose contact in one cycle. The upper contact pair is in separation state more than half period of one cycle. The hysteresis for each contact pair is not symmetric.

5.6.2 Influence of damper angle

In literature (Yang and Meng,1998) pointed out that the damper rotation can be prevented by properly design the damper angle. Here a damper configuration with $\theta_L = \theta_R = 60^\circ$ and left two contact points are more separated than the tested one. The simulation is performed under the same conditions as in section 5.5.1. The comparisons for example 1 and 2 are put in Fig.5.24 and Fig.5.25 respectively.



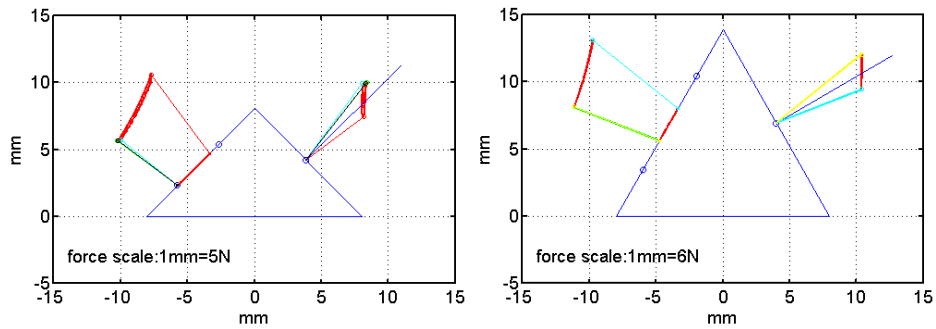


Fig.5.24 Comparison 1- demonstrating damper angle influence

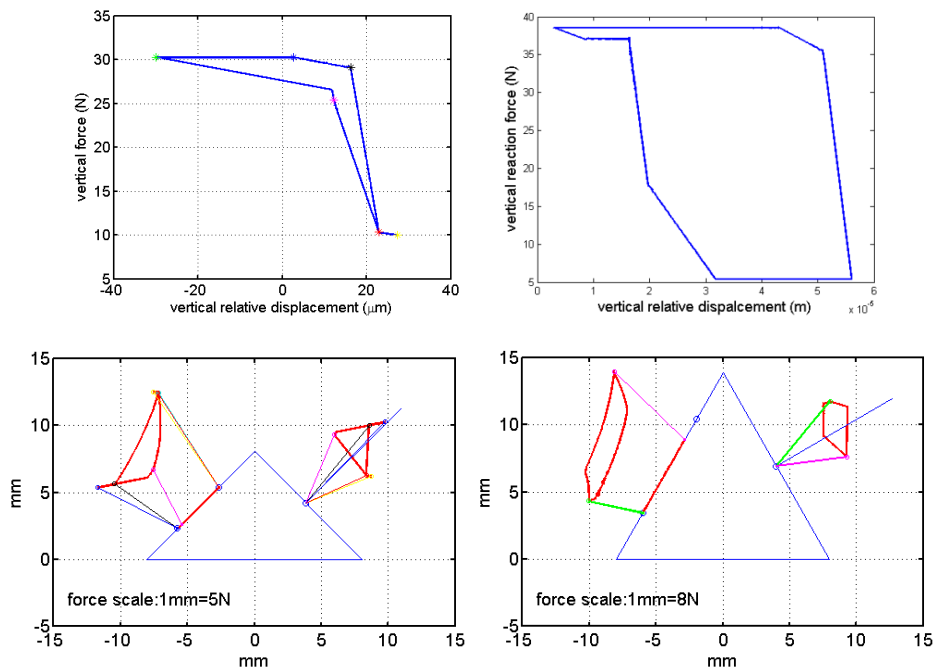


Fig.5.25 Comparison 2- demonstrating damper angle influence

In the first case, the resultant force on the left surface of the 60° damper never reaches the position of two contact points, which means two contact pairs are always in contact. In the second case, the resultant force sometimes reaches the lower contact point position but the force distribution is still much better than the 45° damper. It is predicted that large base angle configuration of three-point damper is much more effective in in-phase motion than the ones with small base angle.

5.7 Exception case of unique steady state solution

Some literature proposed that the steady state response of an under-platform damper may be not unique when initial conditions are different. In the simulation, if there exists one contact interface always in stick condition, the steady state solutions can be non-unique. An example is demonstrated in Fig.5.26 and Fig.5.27.

The common parameters for the two groups are:

motion type	nominal amplitude	excitation frequency	dead weight
out-of-phase	$20\mu m$	5Hz	4.65kg

For first group the initial condition and friction parameters are:

$${}^0_{OR}T = -\mu_R {}^0_{OR}N, \quad {}^0_{OL1}T = \mu_{L1} {}^0_{OL1}N, \quad {}^0_{OL2}T = \mu_{L2} {}^0_{OL2}N$$

$$\mu_R = 0.8, \mu_{L1} = 0.2, \mu_{L2} = 0.2$$

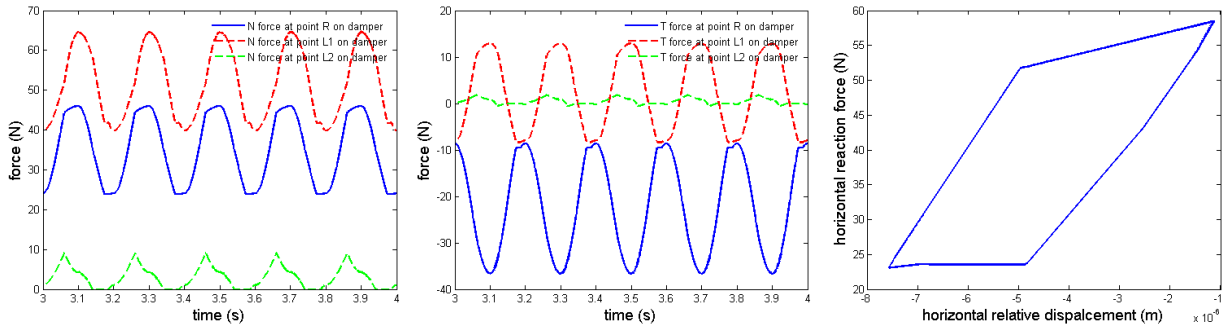


Fig.5.26 Solution 1 of damper response

For second group the initial condition and friction parameters are:

$${}^0_{OR}T = 0, \quad {}^0_{OL1}T = 0, \quad {}^0_{OL2}T = 0$$

$$\mu_R = 0.8, \mu_{L1} = 0.2, \mu_{L2} = 0.2$$

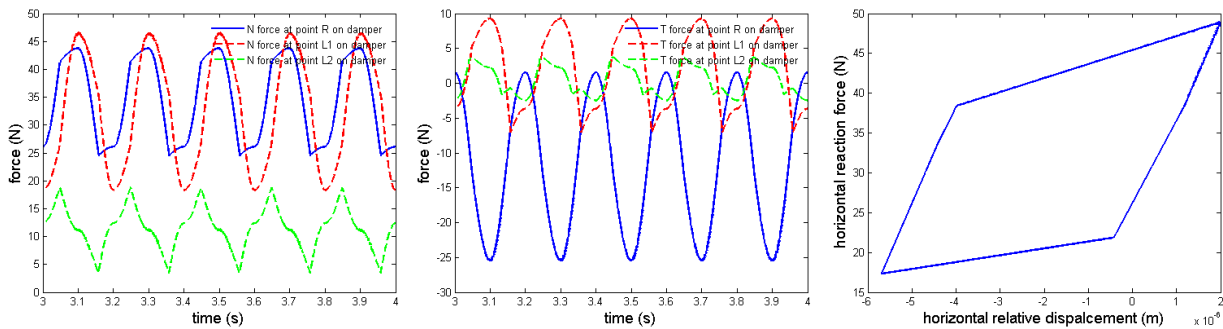


Fig.5.27 Solution 2 of damper response

At this stage, a theoretical understanding of the non-unique solutions is not included in this thesis.

5.8 Conclusions

A time integration procedure is used to simulate damper response in the test rig.

The time integration procedure is based on Newmark method and numerical results from a SDOF system are compared with Den Hartog's solution to verify the reliability of integration method. There are two features of the current time integration method, first it is not unconditionally stable like the traditional Newmark method in linear structural dynamics, second the interfacial high frequency oscillations due to contact stiffness may be not physical.

The time integration procedure is then combined with 2D macro contact model to simulate the three-point damper response. The formulation can be extended to other types of damper conveniently by changing the contact element position and number of contact elements.

The simulation results show good consistency with the experimental results. The force distribution and damper rotation(shape and amplitude) are well predicted. It is verified that when local friction coefficient changes, the damper response can change sensitively. The interfacial high frequency oscillations become critical when the system operation frequency increases. The compliance of the current test rig is not critical to influence the damper response. The steady state solution is checked under different initial conditions and in most test cases it is unique. Potentially if one contact surface is always in stick condition, the solution can be not unique.

The simulation tool is also used to predict the behavior of a three-point damper with different angles. Results show a great influence of this geometry factor to the damper behavior. It is expected in the future this tool can be used to optimize the damper angle and guide the experiments to test this important factor.

Closure

This thesis discusses the experimental and numerical investigations of laboratory under-platform dampers to have better understanding of the damper kinematics and dynamics.

Although the designed test rig has performance limitations after the manufacturing, some experimental results with good repetitions are observed. The experimental hysteresis provides information about contact stiffness and stick-slip state coupled by the two interfaces. The visual stiffness shown in the hysteresis is a coupled quantity from the contact stiffness of both interface. Micro-slip phenomenon is clear in some stages of the hysteresis but in this thesis it is not studied.

Under out-of-phase condition the damper tends to reach a stuck state with pure micro-slip under high friction coefficient. This happens much more quickly when high frequency excitation is applied. This phenomenon is not understood clearly by the author yet. But what can be observed is when rotation dominates like in the in-phase motion, the friction coefficient can be kept relatively low.

A clear motion picture of the damper is reconstructed by measuring translation and rotation of the damper. This does not provide a theoretical modeling of the damper performance but gives people intuitive idea about the damper efficiency.

The numerical procedure built in this thesis gives consistent simulations compared with the experimental results for three-point damper. The simulation tool is helpful to understand what is going on in detail of the damper and contact points. When new types of damper are to be tested, the simulation can provide an prediction giving guidelines. But before applying this numerical tool to a general damper geometry, the local interfacial oscillations should be solved, which is critical especially for high frequency excitation. Micro-slip model can be introduced to the procedure conveniently.

Improvements can be done to the test rig from several aspects:

- 1 Make the structure stiffer without increasing mass along the operation chain.
- 2 Modify the right platform to locate the contact force application point near to the axial center of the perpendicular guiding rods.
- 3 Find a way to test different damper angles at low cost.
- 4 Change the force sensor to a type which is capable of measuring static force component.

5 Put close-loop control to the piezoelectric actuator.

6 Design new laser support for fine tuning the projection position.

Cited literature

- [1] Den Hartog, J. P., "Forced Vibrations with Combined Coulomb and Viscous Friction", *Trans. of ASME*, APM-53-9, pp. 107-115, 1931.
- [2] E.S. Levitan, Forced oscillation of a spring-mass system having combined Coulomb and viscous damping, *Transactions of the ASME* 32 (1960) 1265–1269.
- [3] M.S. Hundal, Response of a base excited system with Coulomb and viscous friction, *Journal of Sound and Vibration* 64 (1979) 371–378.
- [4] T.K. Pratt, R. Williams, Nonlinear analysis of stick/slip motion, *Journal of Sound and Vibration* 74 (1981) 531–542.
- [5] Dariusz Grech, Zygmunt Mazur, The problem of friction in two-dimensional relative motion, May 2000 IFT UWr 934/2000
- [6] B.A. Wernitz, N.P.Hoffmann, Recurrence analysis and phase space reconstruction of irregular vibration in friction brakes: Signatures of chaos in steady sliding, *Journal of Sound and Vibration* 331 (2012) 3887–3896
- [7] P. Duffor, J. Woodhouse, Instability of systems with a frictional point contact. Part 1: basic modeling, *Journal of Sound and Vibration*, 271 (2004) 365–390
- [8] C.F. Beards, J.L. Williams, The damping of structural vibration by rotational slip in joints, *Journal of Sound and Vibration* 53 (1977) 333–340.
- [9] C.F. Beards, A. Woowat, The control of frame vibration by friction damping in joints, *ASME Vibration, Acoustic Stress and Reliability in Design* 107 (1985) 27–32.
- [10] R.A. Ibrahim, Friction-induced vibration, chatter, squeal, and chaos Part II: Dynamics and modeling, *Applied Mechanics Review* 47 (7) (1994) 227–253.
- [11] I. López, J.M. Busturia, H. Nijmeijer, Energy dissipation of a friction damper, *Journal of Sound and Vibration*, 278 (2004) 539–561
- [12] Griffin, J.H., "Friction Damping of Resonant Stresses in Gas Turbine Engine Airfoils", *Journal of Engineering for Power*, v. 102, Apr, 1980.

- [13] Sinha, A., Griffin, J. H., Effects of Static Friction on the Forced Response of Frictionally Damped Turbine Blades, *Journal of Engineering for Gas Turbine and Power*, v. 106, pp. 65-69, Jan. 1984
- [14] Christian, M. Firrone, Dynamics of the underplatform damper for aeronautical turbo engines, PhD thesis at Politecnico di Torino, April, 2006
- [15] Sanliturk, K. Y., Imregun, M., Ewins, D. J.: Harmonic Balance Vibration Analysis of Turbine Blades With Friction Dampers, *Journal of Engineering for Gas Turbine and Power*, v. 119, pp. 958-963, oct. 1997.
- [16] W.D.Iwan.:On a class of models for the yielding behavior of continuous and composite system, *ASME Journal of Applied Mechanics*, N. 89, pp. 612-617, 1967
- [17] Menq, C.H., Bielak, J., and Griffin, J.H., The influence of micro-slip on vibratory response, Part 1: A new micro-slip model, *Journal of Sound and Vibration*, 1985. 107(2): p. 279-293.
- [18] Segalman,D.J., Starr, M.J., Inversion of Masing models via continuous Iwan systems. *International Journal of Non-Linear Mechanics*, 2008. 43: p. 74-80.
- [19] Menq, C.H., Bielak, J., Griffin, J.H., The influence of micro-slip on vibratory response, Part I: a new micro-slip model, *Journal of Sound and Vibration*, N. 107(2), pp. 279-293, 1986
- [20] Casaba G., Forced response analysis in time and frequency domain of a tuned bladed disk with friction dampers, *Journal of Sound and Vibration*, 214(3) (1998) 395–412
- [21] Yang, B.D., Menq, C.H., Modeling of Friction Contact and Its Application to the Design of Shroud Contact, *Journal of Engineering for Gas Turbine and Power*, v. 119, pp. 958- 963, oct. 1997.
- [22] Yang, B.D., Chu, M.L., Menq, C.H., Stick-slip-separation analysis and non-linear stiffness and damping characterization of friction contacts having variable normal load, *Journal of Sound and Vibration*, N. 210(4), pp. 461-481, 1998
- [23] Yang, B.D., Menq, C.H., Characterization of 3D contact kinematics and prediction of resonant response of structures having 3D frictional constraint, *Journal of Sound and Vibration*, N. 217(5), pp. 909-925, 1998
- [24] Yang, B.D., Menq, C.H., Characterization of Contact Kinematics and Application to the Design of Wedge Dampers in Turbomachinery Blading: Part 1 – Stick-Slip Contact Kinematics, *Journal of Engineering for Gas Turbine and Power*, v. 120, pp. 410- 417, apr. 1998.
- [25] Yang, B.D., Menq, C.H., Characterization of Contact Kinematics and Application to the Design of Wedge Dampers in Turbomachinery Blading: Part 2 – Prediction of Forced Response and Experimental Verification, *Journal of Engineering for Gas Turbine and Power*, v. 120, pp. 418- 423, apr. 1998.
- [26] Panning, L., Sextro, W., Popp, K., Optimization of Interblade Friction Damper Design, *ASME Gas Turbine & Aeroengine Congress and Exhibition Munich*, 2000-GT-541, may 2000.

- [27] Csaba, G., Modelling of a Microslip Friction Damper Subjected to Translation and Rotation, ASME Gas Turbine & Aeroengine Congress and Exhibition Indianapolis, 99-GT-149, Jun, 1999.
- [28] Panning, L., Popp, K., Sextro, W., Götting, F., Kayser, A., Wolter, I., Asymmetrical underplatform dampers in gas turbine bladings: theory and application, Proceedings of ASME Turbo Expo 2004, Power for Land, Sea, and Air, Vienna, Austria, June 14-17, 2004
- [29] F. Pfeiffer and M. Hajek, 'Stick-Slip Motion of Turbine Blade Dampers', Phil. Trans. R. Soc. Lond. A 1992 338, 503-517
- [30] K.Y. Sanliturk, D.J. Ewins, A.B. Stanbridge, Underplatform Dampers for Turbine Blades: Theoretical Modeling, Analysis, and Comparison With Experimental Data, Journal of Engineering for Gas Turbines and Power, Vol. 123, 919-929, October, 2001
- [31] D. Botto, S. Zucca, S. Pavone, M.M. Gola, Parametric study of the kinematic behaviour of the underplatform damper and correlation with experimental data, Proceedings of ISMA 2008, 1039-1053
- [32] Christian M. Firrone, Measurement of the kinematics of two underplatform dampers with different geometry and comparison with numerical simulation, Journal of Sound and Vibration, 323 (1-2) (2009) 313-333
- [33] Mindlin, R. D., Deresiewicz, H., Elastic spheres in contact under varying oblique forces, J. Applied Mechanics Trans. ASME, 20, pp. 327-344
- [34] Izhak Etsion, Revisiting the Cattaneo-Mindlin concept of interfacial slip in tangentially loaded compliant bodies, Proceedings of PACAM, Jan 04-08, 2010, Foz do Iguaçu, PR, Brazil
- [35] Mindlin, R. D., Mason, W. P., Osmer, I. F., Deresiewicz, H., Effects of an oscillating tangential force on the contact surfaces of elastic spheres, Proceedings of the First U.S. National Congress of Applied Mechanics, pp. 203-208
- [36] Johnson, K. L., Surface interaction between elastically loaded bodies under tangential forces, Proc. R. Soc. London, Ser. A, A230, pp. 531-549
- [37] Goodman, L. E., and Brown, C. B., Energy dissipation in contact friction: constant normal and cyclic tangential loading, ASME J. Appl. Mech., 29, pp. 17-22
- [38] Berruti, T., Filippi, S., Goglio, L., Gola, M. M., A test rig for frictionally damped bladed segments, ASME Gas Turbine and Aeroengine Congress and Exhibition, 2000, No. 2000-GT-538
- [39] Sanliturk, K.Y., Stanbridge, A. B., Ewins, D.J., Friction Dampers: Measurement, Modeling and Application to Blade Vibration Control", Proc. Des. Eng. Conf., Vol. 3, Part B, DE-Vol. 84-2, ASME, New York, pp. 1377-1382
- [40] Sergio Filippi, Adnan Akay, Muzio M. Gola, Measurement of tangential contact hysteresis during microslip, Trans. ASME, 2004, Vol. 126, pp. 482-489

[41] Lyan-Ywan Lu, Lap-Loi Chung, Lai-Yun Wu, Ging-Long Lin, Dynamic analysis of structures with friction devices using discrete-time state-space formulation, *Computers & Structures*, 84 (2006) 1049-1071

[42] Rolf Krause, Mirjam Walloth, A time discretization scheme based on Rothe's method for dynamical contact problems with friction

[43] Johnson, K. L. *Contact Mechanics*, Cambridge University Press, 1985

[44] M.M.I. Baig, K.J. Bathe, On direct time integration in large deformation dynamic analysis, Third MIT Conference on Computational Fluid and Solid Mechanics

[45] PI-Ceramic, PZ 138E User Manual - PICA™-Stack / PICA™-Power / PICA™-Thru - Piezoceramic Actuators, in Product Description and Operating Notes, P.C. GmbH, Editor. 2004, PI Ceramic GmbH: Lederhose, Germany. p. 16.